

2006

Spin Polarized Transport in Nanoscale Devices

Sandipan Pramanik
Virginia Commonwealth University

Follow this and additional works at: <http://scholarscompass.vcu.edu/etd>

 Part of the [Electrical and Computer Engineering Commons](#)

© The Author

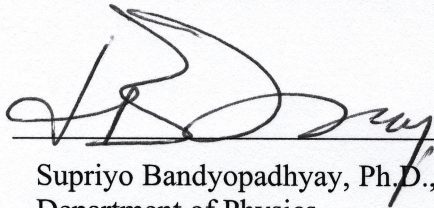
Downloaded from

<http://scholarscompass.vcu.edu/etd/1092>

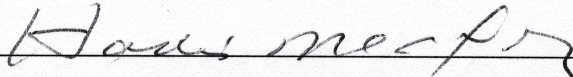
This Dissertation is brought to you for free and open access by the Graduate School at VCU Scholars Compass. It has been accepted for inclusion in Theses and Dissertations by an authorized administrator of VCU Scholars Compass. For more information, please contact libcompass@vcu.edu.

School of Engineering
Virginia Commonwealth University

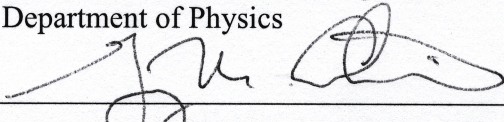
This is to certify that the dissertation prepared by Sandipan Pramanik entitled SPIN POLARIZED TRANSPORT IN NANOSCALE DEVICES has been approved by his committee as satisfactory completion of the dissertation requirement for the degree of Doctor of Philosophy



Supriyo Bandyopadhyay, Ph.D., Department of Electrical and Computer Engineering and Department of Physics



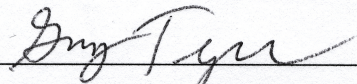
Hadis Morkoc, Ph.D., Department of Electrical and Computer Engineering and Department of Physics



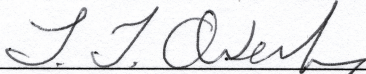
Gary Atkinson, Ph.D., Department of Electrical and Computer Engineering



Puru Jena, Ph.D., Department of Physics



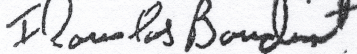
Gary Tepper, Ph.D., Department of Mechanical Engineering



L. Thomas Overby, Ph.D., Assistant Dean of Graduate Affairs, School of Engineering



Russell D. Jamison, Ph.D., Dean, School of Engineering



F. Douglas Boudinot, Ph.D., Dean, School of Graduate Studies

September 20, 2006

© Sandipan Pramanik, 2006

All Rights Reserved

SPIN POLARIZED TRANSPORT IN NANOSCALE DEVICES

A dissertation submitted in partial fulfillment of the requirements for the degree of
Doctor of Philosophy at Virginia Commonwealth University

by

SANDIPAN PRAMANIK

M.S., Virginia Commonwealth University, 2003

B.E., Bengal Engineering and Science University (West Bengal, India), 2001

Director: SUPRIYO BANDYOPADHYAY

PROFESSOR, DEPARTMENT OF ELECTRICAL AND COMPUTER ENGINEERING
AND DEPARTMENT OF PHYSICS

Virginia Commonwealth University
Richmond, Virginia
September, 2006

Acknowledgement

Many people have in various ways helped me bring this dissertation to its current state. In grateful recognition of their contribution, I would like to thank

- Prof. Supriyo Bandyopadhyay for his invaluable help, guidance and unwavering support throughout my graduate studies. Everything I learnt about research in last four years has come from him.
- United States Air Force Office of Scientific Research (AFOSR) and the National Science Foundation (NSF-USA) for providing financial support of this work.
- Prof. Marc Cahay and Mr. Kalyan Garre at the University of Cincinnati, for numerous valuable discussions on various projects that are part of this dissertation.
- Members of the dissertation committee (Prof.s Hadis Morkoc, Puru Jena, Gary Atkinson and Gary Tepper at Virginia Commonwealth University) for critically reviewing this work and for a number of insightful comments.
- My colleagues and friends at VCU, who made my stay in Richmond very enjoyable and with whom I share many unforgettable experiences of graduate student life.
- My undergraduate advisor Dr. Mainak Sengupta at Bengal Engineering and Science University, whose inspiration and guidance provided my key of entry into the exciting world of scientific research.

- And last but not the least, my mother Smt. Bani Pramanik, my sister Malabika and her husband Karthik for standing by me during all my difficult times. None of this would have been possible without your constant support and encouragement. This work is dedicated to you all.
-

Table of Contents

	Page
Acknowledgement	ii
List of Tables	vii
List of Figures	viii
Chapter	
1 Introduction.....	1
1.1 Spin-orbit coupling: basic concepts	3
1.2 Spin-orbit coupling in solids and symmetry considerations	6
1.3 Spin polarized transport in semiconductors in presence of spin-orbit coupling	11
1.4 Hyperfine interaction in semiconductor quantum dots	17
1.5 This dissertation	25
2 Spin Relaxation in Time versus Space: The Difference between Charge and Spin Diffusion Constants	28
2.1 Introduction	29
2.2 Analytical proof that $D_c \neq D_s$	31
2.3 Spin diffusion constant and charge diffusion constant.....	41
2.4 Necessary conditions for D'yakonov-Perel' spin relaxation in space...42	
2.5 Conclusion.....	46

3	D'yakonov-Perel' Spin Relaxation in a Quantum Wire: Multichanneled Transport	48
	3.1 Introduction	49
	3.2 Theoretical model.....	50
	3.3 Results and discussion.....	53
4	D'yakonov-Perel' Spin Relaxation of "Upstream" Electrons in a Quantum Wire: Failure of the Traditional Drift-Diffusion Model.....	58
	4.1 Drift-diffusion model of spin transport	59
	4.2 Semiclassical model of spin relaxation	62
	4.3 Model of upstream spin transport.....	65
	4.4 Results and discussion.....	70
	4.5 Population inversion of upstream electrons	74
	4.6 Conclusion.....	79
5	Spin Fluctuations and "Spin Noise"	84
	5.1 Introduction	84
	5.2 Theoretical model.....	85
	5.3 Results and discussion.....	86
	5.4 Conclusion.....	87
6	Spin Transport Experiment in Self-Assembled All-Metal Nanowire Spin Valves: A Study of the Pure Elliott-Yafet Mechanism	92
	6.1 Introduction	93

6.2	Experimental results	95
6.3	Results and discussion	100
6.4	Conclusion	110
7	Spin Relaxation in a Nanowire Organic Spin Valve: Observation of Extremely Long Spin Relaxation Times	111
7.1	Introduction	112
7.2	Experimental procedure	114
7.3	Results and discussion	116
8	Transverse Spin Relaxation Times in an Ensemble of Electrochemically Self-Assembled CdS Quantum Dots	143
8.1	Introduction	144
8.2	Sample fabrication procedure	147
8.3	Experimental results	148
8.4	Discussion	151
8.5	Conclusion	152
	Bibliography	154
	Short vita	170

List of Tables

Page

Table 6.1: Spin relaxation lengths and spin relaxation times at various temperatures. ...107

List of Figures

	Page
Figure 1.1: Hyperfine interaction in a quantum dot.....	21
Figure 2.1: Geometry of the quantum wire.....	32
Figure 2.2: Temporal decay of ensemble averaged spin components as calculated using Monte Carlo simulator	37
Figure 2.3: Spatial spin relaxation in a GaAs quantum wire as described in Figure 2.1 ...	39
Figure 3.1 Spatial decay of the normalized spin polarized current in a GaAs quantum wire channel of rectangular cross-section $30 \text{ nm} \times 4 \text{ nm}$	54
Figure 3.2: Spatial decay of the normalized spin polarized current and the injected spin vector in the GaAs quantum wire channel.....	55
Figure 3.3: Dependence of spin relaxation length on transport-driving electric field.....	56
Figure 4.1: A quantum wire structure of length $L = 1.005 \text{ }\mu\text{m}$ with rectangular cross-section $30 \text{ nm} \times 4 \text{ nm}$	66
Figure 4.2: Subband energy dispersion in the quantum wire.....	67
Figure 4.3: Spatial variation of ensemble averaged spin components for driving electric field 0.5 kV/cm at steady state.....	72
Figure 4.4: Spatial variation of ensemble averaged spin components for driving electric field 1 kV/cm at steady state.....	73

Figure 4.5: Spatial variation of ensemble averaged spin components for driving electric field 1.5 kV/cm at steady state.....	74
Figure 4.6: Spatial variation of ensemble averaged spin components for driving electric field 2 kV/cm at steady state.....	75
Figure 4.7: Spatial variation of ensemble averaged spin components at steady state. Driving electric field is 1 kV/cm, lattice temperature = 30 K and injection energy is 441 meV. Injected electrons are <i>y</i> polarized.....	76
Figure 4.8: Spatial variation of ensemble averaged spin components at steady state. Driving electric field is 1 kV/cm, lattice temperature = 30 K and injection energy is 426 meV. Injected electrons are <i>z</i> polarized.....	77
Figure 4.9: Spatial variation of electron population over different subbands at steady state. Driving electric field is 0.5 kV/cm, lattice temperature = 30 K and injection energy is 426 meV. Injected electrons are <i>y</i> polarized.	78
Figure 4.10: Spatial variation of electron population over different subbands at steady state. Driving electric field is 1 kV/cm, lattice temperature = 30 K and injection energy is 426 meV. Injected electrons are <i>y</i> polarized.....	79
Figure 4.11: Spatial variation of electron population over different subbands at steady state. Driving electric field is 1.5 kV/cm, lattice temperature = 30 K and injection energy is 426 meV. Injected electrons are <i>y</i> polarized.	81

Figure 4.12: Spatial variation of electron population over different subbands at steady state. Driving electric field is 2 kV/cm, lattice temperature = 30 K and injection energy is 426 meV. Injected electrons are y polarized.	82
Figure 4.13: Spatial variation of electron population over different subbands at steady state. Driving electric field is 1 kV/cm, lattice temperature = 30 K and injection energy is 441 meV. Injected electrons are y polarized.	83
Figure 5.1: Temporal dephasing of the x , y and z components of ensemble averaged spin in the GaAs quantum wire at 30 K. The driving electric field is 2 kV/cm, and the spins are injected with their polarizations initially aligned along the wire axis (x - axis)	89
Figure 5.2: Autocorrelation function of the spin fluctuations in the GaAs quantum wire at a driving electric field of 2 kV/cm and at a lattice temperature of 30 K	90
Figure 5.3: The spectral density of “spin noise” in the quantum wire for driving electric field = 2 kV/cm and lattice temperature = 30 K.	91
Figure 6.1: Schematic description of a nanowire spin valve structure consisting of Co, Cu and Ni.....	94
Figure 6.2: SEM micrograph of the top surface of the alumina template formed by anodization using 3% oxalic acid at 40 V dc.....	95
Figure 6.3: SEM micrograph of the bottom surface of the alumina template after removing the bulk aluminum. This shows that the reverse polarity etching has successfully removed the barrier layer	96

Figure 6.4: Transmission electron micrograph of released tri-layered nanowires showing that the Cu layer is ~ 40 nm thick	98
Figure 6.5: A schematic representation of the all-metal nanowire spin valve device. Note that not all nanowires are connected from both sides. Here only two wires are shown connected (electrically) from both ends.....	99
Figure 6.6: The linear I - V characteristics of the device shown in Figure 6.5.....	101
Figure 6.7 (a): Magnetoresistance characteristics at 100 K and bias current of 10 microamperes. The spin valve peaks are indicated by the vertical arrows.....	102
Figure 6.7 (b): Magnetoresistance characteristics at 50 K and bias current of 10 microamperes. The spin valve peaks are indicated by the vertical arrows.....	103
Figure 6.7 (c): Magnetoresistance characteristics at 1.9 K and bias current of 10 microamperes. The spin valve peaks are indicated by the vertical arrows.....	104
Figure 6.8: Magnetoresistance characteristics at 1.9 K and bias current of 100 microamperes. The spin valve peaks are indicated by the vertical arrows.....	109
Figure 7.1: Schematic description of the sample fabrication process. The red, yellow and green layers indicate cobalt, Alq ₃ and nickel respectively	116
Figure 7.2: Magnetoresistance trace of the control sample, consisting of ~ 500 Ni-Co bilayered nanowires (no Alq ₃)	118
Figure 7.3: Distribution of the spin valve signal.....	120
Figure 7.4 (a): Magnetoresistance trace of Alq ₃ nanowire at 1.9 K. The magnetic field is parallel to the wire axis. Solid and broken arrows indicate reverse and forward scans of	

the magnetic field. The spin valve peaks occur between + (-) 800 Oe and + (-) 1800 Oe	123
Figure 7.4 (b): Magnetoresistance trace of Alq ₃ nanowire at 10 K. The magnetic field is parallel to the wire axis. Solid and broken arrows indicate reverse and forward scans of the magnetic field. The spin valve peaks occur between + (-) 800 Oe and + (-) 1800 Oe	126
Figure 7.4 (c): Magnetoresistance trace of Alq ₃ nanowire at 50 K. The magnetic field is parallel to the wire axis. Solid and broken arrows indicate reverse and forward scans of the magnetic field. The spin valve peaks occur between + (-) 800 Oe and + (-) 1800 Oe	127
Figure 7.4 (d): Magnetoresistance trace of Alq ₃ nanowire at 100 K. The magnetic field is parallel to the wire axis. Solid and broken arrows indicate reverse and forward scans of the magnetic field. The spin valve peaks occur between + (-) 800 Oe and + (-) 1800 Oe	128
Figure 7.5: Inverse spin valve effect and background negative magnetoresistance in Ni-Alq ₃ -Co nanowires at four different temperatures and fixed bias of 10μA rms.....	129
Figure 7.6: Inverse spin valve effect and background negative magnetoresistance in Ni-Alq ₃ -Co nanowires at four different bias values and fixed temperature of 1.9 K	130
Figure 7.7: Transmission electron micrograph of a typical nanowire spin valve structure. In this set of samples, thickness of the Alq ₃ layer is ~ 33 nm	131

Figure 7.8: Current versus voltage characteristics of the trilayered spin valve nanowires at three different temperatures	132
Figure 7.9: Transmission electron micrograph of a typical nanowire spin valve structure (2 nd set of samples). In this set, thickness of the Alq ₃ layer is ~ 26 nm.....	133
Figure 7.10: This figure plots spin relaxation length in Alq ₃ nanowires as a function of temperature	134
Figure 7.11: This figure plots spin relaxation time in Alq ₃ nanowires as a function of temperature	136
Figure 7.12: This figure plots spin relaxation length in Alq ₃ nanowires as a function of applied bias at a fixed temperature of 1.9 K.....	140
Figure 7.13: This figure plots spin relaxation time in Alq ₃ nanowires as a function of applied bias at a fixed temperature of 1.9 K.....	141
Figure 7.14: Explanation of background negative and positive magnetoresistance.....	142
Figure 8.1: Schematic description of the sample fabrication process.....	149
Figure 8.2: A SEM micrograph of nanoporous template with nominal pore diameter of 10 nm. The areal density of the pores is approximately 10 ¹¹ /cm ²	150
Figure 8.3: First derivative of the ESR linewidth as a function of magnetic flux density at four different temperatures. Note that the distance between the two peaks decreases slowly as we increase temperature. The vertical axis is in arbitrary units and the four spectra are shifted vertically for easy comparison.....	150
Figure 8.4: The measured T ₂ [*] time as a function of temperature	153

Abstract

SPIN POLARIZED TRANSPORT IN NANOSCALE DEVICES

By Sandipan Pramanik, Ph.D.

A dissertation submitted in partial fulfillment of the requirements for the degree of
Doctor of Philosophy at Virginia Commonwealth University

Virginia Commonwealth University, 2006

Major Director: Supriyo Bandyopadhyay
Professor, Department of Electrical and Computer Engineering and Department of Physics

The ultimate goal in the rapidly burgeoning field of spintronics is to realize semiconductor-based devices that utilize the spin degree of freedom of a single charge carrier (electron or hole) or an ensemble of such carriers to achieve novel and/or enhanced device functionalities such as spin based light emitting devices, spin transistors and femto-Tesla magnetic field sensors. These devices share a common feature: they all rely on *controlled* transport of spins in semiconductors. A prototypical spintronic device has a transistor-like configuration in which a semiconducting channel is sandwiched between two contacts (source and drain) with a gate electrode sitting on top of the channel.

Unlike conventional charge-based transistors, the “source” electrode of a spin transistor is a ferromagnetic (or half-metallic) material which injects *spin polarized* electrons in the channel. During transit, the spin polarizations of the electrons are controllably rotated by a gate electric field mediated spin-orbit coupling effect. The drain contact is ferromagnetic (or half-metallic) as well and the transmission probability of an electron through this drain electrode depends on the relative orientation of electron spin polarization and the (fixed) magnetization of the drain. When the spins of the electrons are parallel to the drain magnetization, they are transmitted by the drain resulting in a large device current (ON state of spinFET). However, these electrons will be completely blocked if their spins are antiparallel to the drain magnetization, and ideally, in this situation device current will be zero (OFF state of spinFET). Thus, if we vary the gate voltage, we can modulate the channel current by controlling the spin orientations of the electrons with respect to the drain magnetization. This is how transistor action is realized (Datta-Das model).

However, during transport, electrons’ velocities change randomly with time due to scattering and hence different electrons experience different spin-orbit magnetic fields. As a result, even though all electrons start their journey with identical spin orientations, soon after injection spins of different electrons point along different directions in space. This randomization of initial spin polarization is referred to as *spin relaxation* and this is detrimental to the spintronic devices. In particular, for Datta-Das transistor, this will lead to inefficient gate control and large leakage current in the OFF state of the spinFET. The aim of this work is to understand various spin relaxation processes that are operative in semiconductor nanostructures and to indicate possible ways of minimizing them.

The theoretical aspect of this dissertation (Chapters 2 – 5) focuses on the D'yakonov-Perel' process of spin relaxation in a semiconductor quantum wire. This process of spin relaxation occurs because during transport electron spin precesses like a spinning top about the spin-orbit magnetic field. We show that the conventional drift-diffusion model of spin transport, which has been used extensively in literature, completely breaks down in case of a quantum confined system (e.g. a quantum wire). Our approach employs a semi-classical model which couples the spin density matrix evolution with the Boltzmann transport equation. Using this model we have thoroughly studied spin relaxation in a semiconductor quantum wire and identified several inconsistencies of the drift-diffusion formalism.

The experimental side of this work (Chapters 6 – 8) deals with two different issues:

- (a) performing spin transport experiments in order to extract spin relaxation length and time in various materials (e.g. Cu, Alq₃) under one-dimensional confinement, and
- (b) measurement of the ensemble spin dephasing time in self-assembled cadmium sulfide quantum dots using electron spin resonance technique.

The spin transport experiment, as described in Chapter 7 of this dissertation, shows that the spin relaxation time in organic semiconductor (Alq₃) is extremely long, approaching a few seconds at low temperatures. Alq₃ is the chemical formula of tris-8-hydroxy-quinoline aluminum, which is a small molecular weight organic semiconductor. This material is extensively used in organic display industry as the electron transport and emission layer in green organic light emitting diodes. The long spin relaxation time in Alq₃ makes it an ideal platform for spintronics. This also indicates that it may be possible to realize spin based organic light emitting diodes which will have much higher internal quantum efficiency

than their conventional non-spin counterparts. From the spin transport experiment mentioned above we have also identified Elliott-Yafet mode as the dominant spin relaxation mechanism operative in organic semiconductors.

Electron spin resonance experiment performed on self-assembled quantum dots (Chapter 8) allows us to determine the ensemble spin dephasing time (or transverse spin relaxation time) of electrons confined in these systems. In quantum dots electrons are strongly localized in space. Surprisingly, the ensemble spin dephasing time shows an increasing trend as we increase temperature. The most likely explanation for this phenomenon is that spin dephasing in quantum dots (unlike quantum wells and wires) is dominated by nuclear hyperfine interaction, which weakens progressively with temperature.

We hope that our work, which elaborates on all of the above mentioned topics in great detail, will be a significant contribution towards the current state of knowledge of subtle spin-based issues operative in nanoscale device structures, and will ultimately lead to realization of novel nano-spintronic devices.

CHAPTER 1. Introduction

Spintronics (acronym for “spin-based electronics”) is defined as the science and technology of manipulating the spin degree of freedom of a single charge carrier (electron or hole) or an ensemble of such carriers to encode, store, process and deliver information [1-3]. In conventional electronic devices (e.g. diodes or transistors) carrier spins point along random directions in space and play no role in the performance of these devices. Spintronic devices, on the other hand, rely on the *controlled* transport of “spin-polarized” carriers. Such a spintronic device is the read-head sensor [4] which accompanies every state-of-the-art computer hard drive. The main advantage of this sensor (over its previous generation counterpart) is its higher sensitivity to magnetic fields originating from the recorded bits on a magnetic hard disc drive (HDD). This increased sensitivity allows efficient signal detection (read operation) from smaller recorded bits and thus leads to enormous storage capacity exceeding 10 Gigabytes/in² [5].

The operating principle of the read head sensor is the *giant magnetoresistance effect* (GMR) observed in heterogeneous metallic systems in which magnetic (e.g. Fe, Co) and non-magnetic layers (e.g. Cu, Ag) are alternately stacked to form a multilayer configuration. The resistance of this multilayered structure depends on the relative magnetization orientations of the ferromagnetic layers. In particular, when the magnetizations of the ferromagnets are parallel (antiparallel) device resistance is low

(high). The change in resistance is approximately 100% at low temperature and hence this effect is dubbed as “giant” magnetoresistance” (GMR) effect [6, 7] as opposed to the anomalous magnetoresistance effect where change in resistance is meager 1-2%. The origin of the GMR effect lies in spin polarized electron injection from ferromagnetic layers into the paramagnet and spin dependent scattering at the ferromagnet/paramagnet interface. A nice review on this topic is available in reference [8].

Motivated by this initial commercial success of spintronics in metallic systems, significant effort has been invested in search of similar killer application in semiconductor based systems. Early efforts in this area were focused on developing spin based analogues of classical signal processing devices (e.g. field-effect [9, 10] or bipolar junction [11-14] transistors). The motivation behind this was a tacit belief that spintronic transistors would consume less power and operate faster than their electronic brethren. A closer re-examination of these concepts reveals that as far as the signal processing functions are concerned, the spintronic transistors may not offer significant advantage over their charge based counterparts [15]. However, these spintronic devices can play a role in memory applications which do not require high gain or high frequency performance. Other unconventional areas where semiconductor spintronics may find niche applications include (a) single spin logic [16], (b) spin neurons [17] and (c) quantum computing using spin in a quantum dot to encode qubits [18, 19].

An important consideration for spintronic devices (irrespective of their applications) is the longevity of spin. After injection in a semiconductor channel, the spin of the carrier couples with the environmental magnetic field accruing from various sources including spin-orbit interaction, nuclear hyperfine interaction and interaction with other charge

carriers. As a result the initial spin polarization gets randomized with time and the spin-coded information is lost. This phenomenon which is commonly referred to as spin dephasing, or spin relaxation, is detrimental to spintronic device applications. Thus it is crucial to understand various spin relaxing mechanisms that are operative in semiconductor nanostructures and devise suitable means to suppress them. This is exactly what this dissertation investigates.

In this work, we address various issues regarding spin relaxation in quasi-one-dimensional (quantum wires) and zero-dimensional (quantum dots) structures. As mentioned above, spin relaxation mainly takes place due to spin-orbit coupling and hyperfine interaction present in the system under consideration. In this introductory chapter we will focus on the basic physics of electron spin relaxation in nanostructures due to these two effects.

This chapter is organized as follows: in the next section we will review the basic concepts of spin-orbit coupling, followed by a discussion on how this effect manifests in solid-state systems. Next we will discuss various modes of electron spin relaxation in solids and how contemporary theories address the problem of spin polarized electron transport. We will conclude with a discussion on hyperfine interaction in quantum dots and present an overview of this dissertation.

1.1 Spin-orbit coupling: basic concepts

Spin is an intrinsic magnetic moment associated with an electron. In order to control spin-orientation, we need a magnetic field. This field can either be externally applied or it

can originate from the spin-orbit coupling effect of the system in which the electron belongs. In this section we review the basic concepts of spin-orbit coupling.

Let us consider an electron moving with a velocity \vec{v}_e under the influence of an external electric field \vec{E} . In case of a single hydrogen atom, this electric field arises due to the positively charged proton situated at the center of the atom. In the rest frame of the electron, the proton orbits the electron with a velocity same as the velocity of the electron around the proton (just as the Sun orbits the Earth in the Earth's rest frame). This "orbiting" positively charged proton produces a magnetic field at the location of the electron according to the laws of electrodynamics. We can also arrive at this same physical picture starting from the special theory of relativity. The proton, in its rest frame, experiences only the coulomb electric field between itself and the orbiting electron. However, to the electron, in its own rest frame, this electric field appears as a Lorentz-transformed magnetic field [20]. This magnetic field, denoted by B' , is given by the well known equation [21]:

$$\vec{B}' = \frac{(\vec{E} \times \vec{v}_e)/c^2}{\sqrt{1 - (v_e/c)^2}} \rightarrow \frac{\vec{E} \times \vec{v}_e}{c^2}, \text{ on the limit } v_e \ll c \quad (1.1)$$

where c is the velocity of light and \vec{v}_e is the linear velocity of the orbiting electron. This magnetic field (originating from "orbital" or spatial motion of the electron), in the rest frame of the electron, affects the spin polarization of the electron. This is the so-called "spin-orbit coupling" effect where spin polarization of an electron is influenced by its spatial motion in an electric field. The energy of an electron due to this spin-orbit magnetic field is given by

$$\varepsilon = -\vec{\mu} \cdot \vec{B}' \equiv -\frac{e\hbar}{2m_e} \vec{\sigma} \cdot \vec{B}' \quad (1.2)$$

where $\vec{\mu}$ is the electron spin magnetic moment, m_e is the electronic mass and $\vec{\sigma}$ is the Pauli spin matrix.

Thus, combining equations (1.1) and (1.2) we can write the quantum-mechanical Hamiltonian describing spin-orbit coupling as

$$H_{SO} = -\frac{e\hbar}{2m_e c^2} \vec{\sigma} \cdot (\vec{\nabla} V \times \vec{v}_e^{OP}) \quad (1.3)$$

where V is the electric potential, spatial variation of which gives rise to the electric field \vec{E} and \vec{v}_e^{OP} is the electron velocity operator.

The above discussion is qualitative in nature and indeed cannot explain the experimentally observed atomic spectra. Historically, this discrepancy posed a major challenge to the physicists [22]. Later, Thomas pointed out [23] that this discrepancy is resolved by a correct treatment of the Lorentz transformations connecting electron's rest frame and lab frame. Because of the acceleration of the orbiting electron, it is not enough to boost the lab frame by the electron's instantaneous velocity in order to obtain a rest frame of reference. An observer in the rest frame of the electron finds that additional rotation is required to align his coordinate axes with the ones obtained by boosting the lab frame of reference. If this consideration is taken into account, it introduces an additional factor of two in the denominator of the expression describing spin-orbit Hamiltonian (H_{SO}) in equation (1.3).

From the above discussion we can loosely say that spin-orbit interaction splits a spin-degenerate level into two spin-split levels with spins parallel and antiparallel to the spin-

orbit magnetic field. In a free atom, this is indeed the case, where the spin-split levels have same spatial wavefunctions but spinors pointing along opposite directions. However, in solids, such a splitting may be prohibited due to issues regarding crystal symmetry. In the next section we will focus on the spin-orbit coupling effects in solids and discuss these symmetry issues in detail. Depending on the origin of the potential gradient $\vec{\nabla}V$, there exist various types of spin-orbit interactions in solids. Judicious control of these effects can lead to novel spintronic devices as proposed in numerous research articles over the last decade.

1.2 Spin-orbit coupling in solids and symmetry considerations

A central theorem in solid-state physics is the Bloch's theorem which states that if the potential energy $U(r)$ is periodic with the periodicity of the lattice, then the solutions $\varphi(r)$ of the wave equation

$$H \varphi(r) = \left[-\frac{\hbar^2}{2m_e} \nabla^2 + U(r) \right] \varphi(r) = E \varphi(r) \quad (1.4)$$

are of the form $\varphi_k(r) = \exp(i\vec{k} \cdot \vec{r}) u_k(r)$ where $u_k(r)$ is periodic with the periodicity of the direct lattice and k denotes electron quasi momentum. Even in the absence of externally applied electric field or material inhomogeneity, an electron moving inside a “perfect” solid experiences electric fields $(-\vec{\nabla}U(r)/e)$ due to the periodic lattice of ions and the presence of other electrons. This “crystal electric field” may or may not produce a net spin-orbit magnetic field, depending on symmetry properties of the unit cell. Specifically, if the cell does not possess center of inversion symmetry, this electric field will result in a non-zero spin-orbit magnetic field which will in turn affect the electron spin. This is

exactly what happens in crystals of III-V (e.g. GaAs, InAs) or II-VI (e.g. CdS, ZnSe) semiconductors where the crystal lattice consists of two dissimilar atoms. These symmetry issues will be revisited in greater detail in subsections 1.2.1 and 1.2.2. The bottomline is that if an electron travels through an inversion asymmetric crystal, its spin will be reoriented due to precession about the spin-orbit magnetic field which is inherent to the crystal. This is the so-called D'yakonov-Perel' mechanism and we will discuss this in section 1.3. For crystals that possess inversion symmetry (e.g. Ge, Si), the net spin-orbit magnetic field is zero but spin re-orientation can happen via momentum relaxing collisions. This is the Elliott-Yafet mechanism which will be addressed in section 1.3.

Another point that needs to be mentioned is that real crystals contain impurities and the electrons experience electric field in the proximity of these impurities. This can also, in principle, introduce additional spin-orbit coupling effect and change the spin polarization of the electron. The impurity distribution is not periodic by any means and hence their effect cannot be incorporated in the quantity $U(r)$. Generally the impurities are treated as scatterers that scatter Bloch electrons from one momentum state \vec{k} to another state \vec{k}' . As mentioned earlier, in presence of spin-orbit interaction, these innocuous, spin-independent scattering processes can affect the spin of an electron (Elliott-Yafet). Additionally if the impurity species is magnetic in nature then there will be a direct coupling between electron spin and the magnetic moment of the impurity. Yet another source of momentum scattering in a solid is the temperature induced vibrations of lattice ions (or phonons). This introduces temperature dependence in the Elliott-Yafet spin relaxation rate.

In order to address these various effects systematically, let us first consider the spin-orbit coupling effect arising from the periodic crystal electric field $(-\vec{\nabla}U(r)/e)$ only. The effect of impurity or phonon scattering will be considered in section 1.3. Since $U(r)$ has the periodicity of the lattice, the spin-orbit coupling term arising from it (see equation (1.3)) also has the same periodicity. So the corresponding eigenfunction will have the Bloch form i.e. they will have the same spatial periodicity as the crystal lattice. *But these functions will not, in general, correspond to pure spin states.* In other words there will be no global spin quantization axis for all \vec{k} . This can be understood easily because different electrons have different velocities and hence the spin-orbit magnetic fields experienced by the electrons point along different directions in space. Analytically we can write the Bloch state as [24]

$$\varphi_{k,\uparrow}(r) = \alpha_{k,\uparrow}(r) |\uparrow\rangle_z + \beta_{k,\downarrow}(r) |\downarrow\rangle_z \equiv \begin{pmatrix} \alpha_{k,\uparrow}(r) \\ \beta_{k,\downarrow}(r) \end{pmatrix} \quad (1.5)$$

Here $\alpha_{k,\uparrow}(r)$ and $\beta_{k,\downarrow}(r)$ are the Bloch-type functions with lattice periodicity. These are the coefficients of the pure spin states given by

$$|\uparrow\rangle_z \equiv \begin{pmatrix} 1 \\ 0 \end{pmatrix}, \text{ and } |\downarrow\rangle_z \equiv \begin{pmatrix} 0 \\ 1 \end{pmatrix} \quad (1.6)$$

where \hat{z} is some arbitrary direction in space. The “ \uparrow ” sign in the suffix of $\varphi_{k,\uparrow}$ in equation (1.5) indicates that this state is “generally up” (or “pseudo spin up”) in the sense

$$\langle \varphi_{k,\uparrow} | \sigma_z | \varphi_{k,\uparrow} \rangle = |\alpha_{k,\uparrow}|^2 - |\beta_{k,\downarrow}|^2 > 0 \quad (1.7)$$

In what follows, we will continue to assume without any loss of generality that $|\alpha_{k,\uparrow}| > |\beta_{k,\downarrow}|$. In the following subsections we will see how various symmetry elements affect spin splitting of the energy bands.

1.2.1 Time reversal symmetry and Kramer's theorem

The time reversal transformation \mathbf{K} maps $\vec{r} \rightarrow \vec{r}$, $\vec{p} \rightarrow -\vec{p}$ and $\vec{\sigma} \rightarrow -\vec{\sigma}$. Mathematically, $\mathbf{K} = -i\sigma_y \mathbf{K}_0$ where \mathbf{K}_0 , in Schrödinger representation, is the operation of taking the complex conjugate [25]. When operated on $\varphi_{k,\uparrow}$, we obtain

$$\begin{aligned} \mathbf{K}\varphi_{k,\uparrow} &= -i\sigma_y \mathbf{K}_0 \begin{bmatrix} \alpha_{k,\uparrow}(r) \\ \beta_{k,\downarrow}(r) \end{bmatrix} = -i \begin{bmatrix} 0 & -i \\ i & 0 \end{bmatrix} \begin{bmatrix} \alpha_{k,\uparrow}^*(r) \\ \beta_{k,\downarrow}^*(r) \end{bmatrix} = \begin{bmatrix} 0 & -1 \\ 1 & 0 \end{bmatrix} \begin{bmatrix} \alpha_{k,\uparrow}^*(r) \\ \beta_{k,\downarrow}^*(r) \end{bmatrix} \\ &= \begin{bmatrix} -\beta_{k,\downarrow}^*(r) \\ \alpha_{k,\uparrow}^*(r) \end{bmatrix} \equiv -\beta_{k,\downarrow}^*(r) |\uparrow\rangle_z + \alpha_{k,\uparrow}^*(r) |\downarrow\rangle_z \end{aligned} \quad (1.8)$$

which is clearly a “pseudo spin down” state since $|\alpha_{k,\uparrow}|^2 > |\beta_{k,\downarrow}|^2$ (see equation (1.7)). Also, this state $\mathbf{K}\varphi_{k,\uparrow}$ belongs to wavevector $-\vec{k}$. Similarly, the time reversal operator, acting on a “pseudo spin down” state, produces a pseudo spin up state with opposite wavevector. According to Kramer's theorem, in absence of any external magnetic field, both φ and $\mathbf{K}\varphi$ are the eigenstates of the Hamiltonian with same energy eigenvalue. This implies $\varepsilon_{k,\uparrow} = \varepsilon_{-k,\downarrow}$ and $\varepsilon_{k,\downarrow} = \varepsilon_{-k,\uparrow}$ where ε denotes electron energy. This means that each energy occurs twice but not at the same value of \vec{k} . The up- and down-arrows indicate pseudo spin up and pseudo spin down states respectively.

These states are therefore non-degenerate in presence of spin-orbit coupling. This is analogous to Zeeman splitting where the degeneracy of spin up and spin down states is lifted in presence of an external magnetic field. In the present case, the pseudo Zeeman field originates from spin-orbit interaction and is different for different Bloch states. This field is a function of electron velocity.

1.2.2 Space inversion symmetry

Now let us consider the case when additional symmetry elements are present in the system. In particular, we consider the situation when the crystal has space inversion symmetry. Space inversion operator J maps $\vec{r} \rightarrow -\vec{r}$, $\vec{p} \rightarrow -\vec{p}$ and $\vec{\sigma} \rightarrow \vec{\sigma}$. If the Hamiltonian is invariant under space inversion, then the combined symmetry operations J and K yields $\varepsilon_{k,\uparrow} = \varepsilon_{k,\downarrow}$ [24]. As mentioned before, the up- and down-arrows indicate pseudo spin up and pseudo spin down states respectively. Thus, in presence of inversion symmetry, double degeneracy occurs at same energy and wavevector. This means that the energy of an electron (for a given k) does not depend on its spin orientation. Hence in crystals with inversion symmetry spin splitting is not allowed in bulk and they retain their spin degeneracy. In this case there will be no pseudo Zeeman field as described earlier. But still, momentum scattering events will re-orient electron spin polarization (see section 1.3).

Spin-orbit interaction effect can be classified depending on the origin of the electric field from which it is induced. It is evident from the above discussion that the crystals which lack inversion symmetry, there exists a spin-orbit coupling effect. This is known as “bulk inversion asymmetry” induced “Dresselhaus spin-orbit coupling” [26]. Additional asymmetry can be caused artificially by application of a “gate” electric field on quantum

confined systems (e.g. a two dimensional electron gas). This is known as “structural inversion asymmetry” induced “Rashba spin-orbit coupling” [27, 28]. Also, in case of a quantum well structure, if the well and the barrier have different ionic composition (e.g. InAs/GaSb quantum well), there exists a spin-orbit coupling term due to “interface asymmetry”.

1.3 Spin polarized transport in semiconductors in presence of spin-orbit coupling

Spin transport in semiconductor structures is a subject of much interest from the perspective of both fundamental physics and device applications. The basic problem here is as follows. We inject spin polarized electrons at one end of a semiconductor structure (say $\mathbf{r} = \mathbf{r}_0$) at time $t = t_0$. By “spin polarized injection” we mean that at $t = t_0$ (and $\mathbf{r} = \mathbf{r}_0$) the spin polarizations of all electrons are either pointing parallel or antiparallel to a particular direction (say $\hat{\theta}_0$) in space such that

$$P_0 = \frac{|n_\uparrow - n_\downarrow|}{n_\uparrow + n_\downarrow} = \frac{|n_\uparrow - n_\downarrow|}{N} > 0 \quad (1.9)$$

Here N is the total number of injected electrons and $n_{\uparrow(\downarrow)}$ is the number of electrons with spins parallel (antiparallel) to $\hat{\theta}_0$. Thus, the quantity P_0 denotes the net spin polarization of the injected electrons (pointing along $\hat{\theta}_0$). In an all-electrical spin transport experiment, this situation is realized by using ferromagnetic (or, half metallic) materials as spin injector¹. The magnitude of P_0 is not in general equal to the polarization of the spin injector, since there is always some spin flip at the injector/semiconductor interface.

¹ In chapters 6 and 7 of this dissertation we report all-electrical spin transport experiments performed on nanowire geometry. There we use nickel and cobalt as spin injector/detector.

After injection, these electrons travel through the semiconductor under the influence of a transport-driving electric field. During their transit, the electrons experience spin-orbit coupling effects originating from various sources as mentioned above. Due to these spin-orbit interactions, the spins of the electrons get re-oriented. In other words, during transit the spin polarizations are not necessarily parallel (or antiparallel) to $\hat{\theta}_0$ and the spin orientations continuously evolve with time. Spin-orbit coupling strength depends on electron velocity and hence the spin-orbit magnetic field is different for different electrons, assuming that there is a spread in electron velocities due to scattering or injection condition. As a result, spins of different electrons get re-oriented by different amounts. Thus at a later instant $t = t_1$, the net spin polarization of electron ensemble (say P_1 , which is equal to the magnitude of ensemble averaged spin polarization vector) is less than its initial value (P_0). This loss of spin polarization is termed as “spin relaxation” or “spin dephasing”.

There are various mechanisms (some of which are obviously mediated by spin-orbit interactions, while others are not) that cause spin relaxation during transport. In case of semiconductors (as well as metals), the most dominant mechanisms [29] are (a) Elliott-Yafet mechanism [30, 31], (b) D'yakonov-Perel' mechanism [32, 33], (c) Bir-Aronov-Pikus mechanism [34] and (d) Hyperfine interaction with nuclei [35]. Among these, the first two mechanisms accrue from spin-orbit interaction. The third one originates from the coupling between electron and hole spin. Hyperfine interaction is due to interaction between carrier spins and the nuclear spins. These mechanisms are briefly described below.

(a) *Elliott-Yafet mechanism:*

As we have seen in section 1.2, in presence of spin-orbit coupling, Bloch states of a real crystal are not spin eigenstates. These states are either pseudo-spin-up or pseudo-spin-down, in the sense that a particular state with a given spin orientation has a small admixture of the opposite spin state. This is an outcome of the presence of spin-orbit coupling in the crystal. This admixture is a function of electronic wavevector, and as a result, in general two different Bloch states have non-orthogonal spin orientations. Thus spin-independent momentum scattering events can couple two different Bloch states and re-orient the initial spin polarization. This is the Elliott-Yafet mechanism of spin relaxation. From the above discussion one naively expects that spin relaxation rate due to Elliott-Yafet mechanism should be proportional to the momentum scattering rate. This is indeed true, and from reference [29], we quote a formula relating these two quantities:

$$\frac{1}{\tau_{s,EY}(E_k)} = A \left(\frac{\Delta_{SO}}{E_g + \Delta_{SO}} \right)^2 \left(\frac{E_k}{E_g} \right)^2 \frac{1}{\tau_p(E_k)} \quad (1.10)$$

This formula is valid for III-V semiconductors. Here $\tau_{p(s,EY)}(E_k)$ is the momentum relaxation time (spin relaxation time due to Elliott-Yafet process) for electrons with energy E_k . The energy gap is denoted by E_g and Δ_{SO} is the spin-orbit splitting of the valence band. The prefactor A , depends on the nature of the scattering mechanism. The above equation indicates that Elliott-Yafet process is significant for semiconductors with small band gap and large spin-orbit splitting. Typical example of such a semiconductor is indium arsenide (InAs).

Note that in case of Elliott-Yafet mechanism, the mere presence of spin-orbit interaction in the system does not cause spin relaxation. Only if the carriers are scattered during transport, spin relaxation takes place. So this mechanism is weak for ballistic transport as well as for semiconductor quantum wires at low temperature. In the latter case, at low temperature, phonon scattering is suppressed, and so is the elastic scattering due to constriction in phase-space [36]. Elliott-Yafet mechanism is weak in these situations. However, this mechanism is dominant in metallic systems. Elliott-Yafet mode is expected to be more efficient in presence of magnetic field. This has been shown analytically [37] in the context of a quantum wire with an axial magnetic field.

(b) *D'yakonov-Perel' mechanism:*

This mechanism of spin relaxation is dominant in solids which lack inversion symmetry. Prototypical examples of such systems are III-V semiconductors (e.g. GaAs) or II-VI semiconductors (e.g. ZnSe) where inversion symmetry is broken by the presence of two distinct atoms in the Bravais lattice. As described earlier in section 1.2, in these systems the momentum states of pseudo spin-up and pseudo spin-down electrons are non-degenerate (recall $\varepsilon_{k,\uparrow} = \varepsilon_{-k,\downarrow} \neq \varepsilon_{k,\downarrow}$ and $\varepsilon_{k,\downarrow} = \varepsilon_{-k,\uparrow} \neq \varepsilon_{k,\uparrow}$ from our earlier discussion on spin-orbit coupling in solids in section 1.2). This spin-splitting can be described by an internal magnetic field \mathbf{B} that depends on electron velocity. As a result, when an electron travels through an inversion-asymmetric crystal, its spin precesses continuously (like a spinning top) about \mathbf{B} . This is the well known Larmor precession of spin about a magnetic field. The magnitude and direction of this magnetic field change every time the electron encounters scattering. This magnetic field is different for different electrons as long as

there is a spread in electron velocity due to scattering or electric field or injection condition. Thus the ensemble averaged spin vector decays with time. This is the D'yakonov-Perel' mode of spin relaxation. Note that unlike Elliott-Yafet mechanism, it is not necessary to have scattering in the system for D'yakonov-Perel' process to take place. As long as the electrons have different velocities (depending on the injection condition), D'yakonov-Perel' relaxation will occur.

In chapters 2, 3, 4 and 5 of this dissertation we will discuss various aspects of D'yakonov-Perel' spin relaxation in a quantum wire in presence of Rashba and Dresselhaus spin-orbit interactions.

(c) Bir-Aronov-Pikus mechanism:

This mechanism of spin relaxation is dominant in heavily p-doped semiconductors. The exchange interaction between electrons and holes is described by the Hamiltonian $H = A \vec{S} \cdot \vec{J} \delta(\vec{r})$ where A is proportional to the exchange integral between the conduction and valence states, J is the angular momentum operator for holes and S is the electron spin operator. Now, if the hole spin flips (due to strong spin-orbit interaction in the valence band), due to this electron-hole coupling, the spin of the electron will flip as well. A more detailed description is available in reference [29].

(d) Hyperfine interaction:

Hyperfine interaction is the magnetic interaction between the magnetic moments of electrons and nuclei. This is the dominant spin relaxation mechanism in quantum dots, where the electrons are strongly localized in space. Later in this chapter (see section 1.4) we will discuss this topic in detail.

If we consider unipolar (say electronic) transport in a III-V semiconductor system (bulk, 2D and 1D), the most dominant spin relaxation mechanisms are the Elliott-Yafet mode and D'yakonov-Perel' mode. In chapters 2, 3, 4 and 5 of this dissertation we will discuss various aspects of D'yakonov-Perel' spin relaxation in a semiconductor quantum wire.

Various formalisms have been used to study the problem of spin transport in semiconductor nanostructures, primary among which are a classical drift-diffusion approach [38-40], a kinetic theory approach [41] and a microscopic semiclassical approach [42-48]. As far as the classical models are concerned, a number of studies used a drift-diffusion type approach to model spin transport and spin dephasing at elevated temperatures and moderate electric fields. "Spin up" and "spin down" electrons are treated similar to electrons and holes in conventional bipolar transport. Spin dephasing is treated by a spin relaxation term that describes coupling between the "spin up" and "spin down" electrons similar to the generation-recombination term describing coupling between electrons and holes in bipolar transport. Apart from the fact that the relaxation time approximation does not fully capture the physics of spin dephasing (even if different relaxation times are used to describe different processes), the drift-diffusion formalism is invalid at relatively high electric fields when transport non-linearities become important. Furthermore this model cannot treat coherence effects arising from superposition of spin up and spin down states. Such superpositions are taken into account by the kinetic theory approach, but this model does not treat momentum dependence of spin-orbit coupling self-consistently.

In reality, the temporal evolution of spin and the temporal evolution of the momentum of an electron cannot be separated. The dephasing (or depolarization) rates are functionals

of the electron distribution function in momentum space which continuously evolves with time when an electric field is applied to drive transport. Thus spin dephasing rate is a dynamic variable that needs to be treated self-consistently in step with the dynamic evolution of the electron's momentum. Such situations are best treated by Monte Carlo simulation. In chapters 2, 3, 4 and 5 of this dissertation we adopt this angle of approach for studying spin transport in semiconductor quantum wires and highlight various inconsistencies of the classical drift-diffusion formalism.

1.4 Hyperfine interaction in semiconductor quantum dots

The spin-orbit interaction mechanism described above is the dominant source of electron spin dephasing in bulks, quantum wells and quantum wires, where the electrons are not strongly localized in space. However, in case of quantum dots electron motion is restricted in all three dimensions and hence spin-orbit interaction, being proportional to electron momentum, is extremely weak in these systems [49-51]. Thus, the most effective spin dephasing mechanism in quantum dots is the *hyperfine interaction with nuclei*. Since the spin state of an electron hosted in a semiconductor quantum dot is considered as a promising candidate for realizing solid-state qubit [18, 19, 27, 52-55], it is essential, from the perspective of quantum information processing, to preserve the coherence of the spin-qubit for sufficiently long time in order to perform fault-tolerant (quantum) computational tasks [56]. Even though spin-orbit coupling is sufficiently weak in quantum dots, it is the nuclear hyperfine interaction that poses serious limitation on spin-qubit coherence time in these systems. Motivated by this, there have been a large number of theoretical [57-63] and experimental [64-68] investigations on electron spin dynamics under the influence of

nuclear hyperfine field in quantum dots. A comprehensive review on the theoretical aspect of this topic is available in reference [69]. Here we will briefly discuss some basic concepts regarding the origin of hyperfine interaction in common semiconductor materials and how it causes electron spin dephasing in quantum dots.

1.4.1 Origin of hyperfine interaction in semiconductor materials

Electrons, protons and neutrons are fermions, which imply that they carry half integer spins. For example, an electron is a spin-1/2 particle. It is customary to represent the total angular momentum of the atomic nucleus (neutrons *plus* protons) by the symbol I , and call it *nuclear spin*. An atomic nucleus often behaves as if it is a single entity with intrinsic angular momentum I . Associated with nuclear spin I there is a *nuclear magnetic moment* defined by the relation $\vec{\mu}_I = (g_N q \hbar / 2m_N) \vec{I}$, where g_N is the g -factor of the nucleus, q is the amount of positive charge in the nucleus, m_N is the mass of a neutron/proton (\sim three orders of magnitude heavier than an electron). This nuclear magnetic moment couples with electronic spin magnetic moment and results in dephasing of electron spin in solid state systems. This is how hyperfine interaction (which is nothing but a coupling effect between nuclear and electronic magnetic moments) causes electron spin dephasing. It is interesting to note that even though a neutron is a charge-less particle, it has non-zero magnetic moment. This indicates that neutron is not an elementary particle. Indeed, it is made up of quarks which are charged entities.

Unfortunately, almost all semiconductors have isotopes that carry non-zero nuclear spins. *All* naturally occurring isotopes of Ga, In, Al, Sb and As have nuclear spins with substantial magnetic moments and hence nuclear hyperfine interaction is particularly

dominant in technologically popular III-V semiconductors e.g. Ga(Al)As, In(Al)As etc. On the other hand, materials like Cd, Zn, S, Se and Te have nuclear spin carrying isotopes with less natural abundance and hence in II-VI semiconductor materials nuclear hyperfine interaction is weaker compared to their III-V counterparts. Due to the same reason nuclear hyperfine interaction is weak in case of elemental semiconductors e.g. Si and Ge. Hyperfine interaction can be avoided in case of II-VI semiconductors, Si and Ge if we use isotopically purified material containing a greatly reduced amount of $I \neq 0$ isotopes. But due to the high cost of isotopic purification, this may not be a commercially viable option.

As mentioned before, hyperfine interaction is the coupling of nuclear magnetic moment (proportional to nuclear spin I) and electron magnetic moment (due to both orbital motion and spin S). For an s -type electron, there is no orbital contribution and in this case, the hyperfine interaction is described by the Fermi contact Hamiltonian [35, 70]

$$H_{\text{hf}} = \frac{4\mu_0}{3I} \mu_B \mu_I |\psi(\vec{r}_I)|^2 \vec{S} \cdot \vec{I} \quad (1.11)$$

where \vec{S} (\vec{I}) is the electron (nuclear) spin operator, $\psi(\vec{r}_I)$ is the value of (s -type) electronic wavefunction at the location (\vec{r}_I) of the nucleus, $\mu_0 = 4\pi \times 10^{-7} \text{ V s A}^{-1} \text{ m}^{-1}$, and μ_B is the Bohr magneton. The hole wavefunction is zero at the nuclear sites and hence the hyperfine interaction of nuclear spins with holes is considerably weaker.

The above equation is the starting point for describing nuclear hyperfine interaction on an s -type conduction band electron in a quantum dot. In this case we can write the wavefunction $\psi(\vec{r}_I)$ as a product of Bloch amplitude function $u(\vec{r}_I)$ and a modulating envelope function $\phi(\vec{r}_I)$. Thus the hyperfine Hamiltonian takes the form

$$H_{\text{hf}} = \frac{4\mu_0}{3I} \mu_B \mu_I \xi \left| \varphi(\vec{r}_I) \right|^2 \vec{S} \cdot \vec{I} \quad (1.12)$$

where $\xi = \left| u(\vec{r}_I) \right|^2 \approx \left| u(0) \right|^2$ is a constant (independent of \vec{r}_I) for a given semiconductor material. If the electron density were homogeneously smeared over the unit cell, ξ would be equal to unity. However in real crystals, $\left| u(\vec{r}_I) \right|$ has sharp maxima at the lattice sites (i.e. locations of the nuclei) and hence $\xi > 1$. The value of this quantity can be extracted from electron spin resonance experiments [70]. Typical values of ξ for different materials are as follows [69, 70]:

$$\xi_{\text{In}} = 6.3 \times 10^3, \xi_{\text{Sb}} = 10.9 \times 10^3, \xi_{\text{Ga}} = 2.7 \times 10^3, \xi_{\text{As}} = 4.5 \times 10^3, \xi_{\text{Si}} = 186.$$

The hyperfine interaction described above plays a dual role. On one hand we can view it as an effective magnetic field (B_N) created by nuclear spins which interacts with electron spins and causes dephasing. On the other hand it can also be viewed as an effective magnetic field (B_e) *created by the electron spin magnetic moment and acting on the nuclear spin*. In the latter case, this causes nuclear spin relaxation. In electron spin resonance experiments the quantity B_N gives rise to *Overhauser shift* by modifying the electron spin precession frequency. In case of nuclear spin resonance experiments, the quantity B_e results in an analogous effect which is known as *Knight shift*. This intricate interaction is schematically explained in the Figure 1.1.

An electron spin hosted in a (GaAs) quantum dot typically experiences 10^5 nuclear spins in its vicinity. So we can express the net hyperfine interaction (as experienced by the electron spin) as a summation of contributions from every individual nuclear spin:

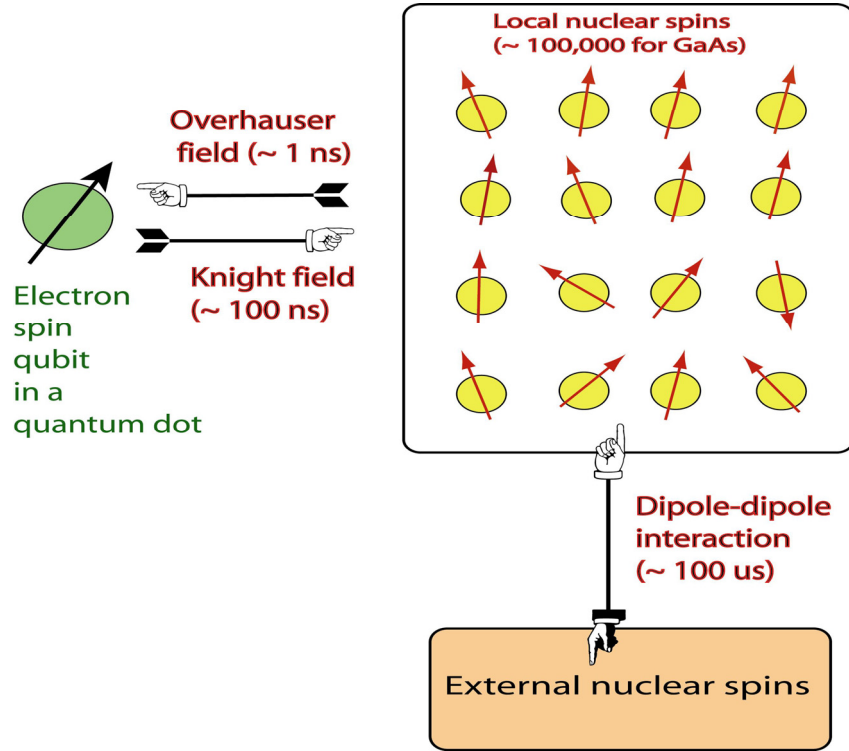


Figure 1.1 Hyperfine interaction in a quantum dot

$$H_{hf} = \vec{S} \cdot \sum_{i=1}^N A_i \vec{I}_i \quad (1.13)$$

where the subscript i denotes the i th nuclear spin and N is the total number of nuclear spin the electron is interacting with. From equation (1.12), the coupling constant A_i is given by

$$A_i = \left[\frac{4\mu_0}{3I} \mu_B \mu_I \xi n_0 \right] v_0 |\varphi(\vec{r}_i)|^2 \equiv A v_0 |\varphi(\vec{r}_i)|^2 \quad (1.14)$$

where $n_0 = 1/v_0$ is the density of the nuclei, v_0 being the volume of the unit cell. We can write the effective magnetic field experienced by the electron spin due to all nuclear spins as:

$$\vec{B}_N = \frac{\sum_{i=1}^N A_i \vec{I}_i}{g \mu_B} = \frac{A v_0 \sum_{i=1}^N |\varphi(\vec{r}_i)|^2 \vec{I}_i}{g \mu_B} \quad (1.15)$$

Clearly electrons localized in various regions of a single quantum dot will experience very different values of B_N since this quantity depends on how the electronic envelope function is spatially distributed over various nuclear sites. The value of B_N also depends on the relative alignment of the nuclear spins. To elaborate this latter point we consider two extreme cases: (1) when the nuclear spins are fully polarized and (2) when they are fully unpolarized. We will observe that relative alignment of the nuclear spins strongly affects the nuclear magnetic field.

Case 1: If all nuclei are *fully polarized* (ferromagnetic inter-nuclei coupling), i.e. if all nuclear spins \vec{I}_i point along some arbitrary direction \hat{z} , we have

$$\begin{aligned} \vec{B}_{N, \text{ fully polarized}} &= \frac{A v_0}{g \mu_B} \sum_{i=1}^N |\varphi(\vec{r}_i)|^2 \hat{z} \approx \frac{A v_0}{g \mu_B} \left[\frac{1}{v_0} \int_{\Omega} |\varphi(\vec{r})|^2 d\Omega \right] \hat{z} \\ &= \frac{A}{g \mu_B} \hat{z} \end{aligned} \quad (1.16)$$

where we have used the normalization condition $\int_{\Omega} |\varphi(\vec{r})|^2 d\Omega = 1$. Here Ω denotes that the integration has been carried out over the unit cell with volume v_0 . This “fully polarized” configuration is probably valid at zero temperature when the system is in ground state (i.e. S and I_i are antiparallel leading to minimum value of H_{hf}) and inter-nuclear coupling is ferromagnetic. Optical pumping techniques, in presence of an external magnetic field can also produce considerable alignment of the nuclear spins. This fully-

polarized nuclear configuration gives rise to strong Overhauser field acting on the electron spin qubit.

Case 2: Now let us consider the opposite limit when the nuclear spin system is *fully unpolarized*. This means that at a given time different nuclear spins point along arbitrary

directions in space implying $\sum_{i=1}^N \vec{I}_i \rightarrow 0$. In order to get an estimate of $B_{N, \text{fully unpolarized}}$, we

replace \vec{I}_i by its ‘‘fluctuation value’’ (ΔI). To calculate this quantity we proceed as

follows. Since nuclear spins \vec{I}_i vary randomly from one nuclear site to another, we can

consider it as a random variable in statistical sense. Thus, fluctuation ΔI is defined as the

standard deviation of \vec{I}_i (mean value of \vec{I}_i), which is also a random variable. Thus

$$\begin{aligned} \Delta I &= \sqrt{\text{variance}(\vec{I}_i)} = \sqrt{\text{variance}\left[\frac{\vec{I}_1 + \vec{I}_2 + \dots + \vec{I}_N}{N}\right]} = \sqrt{\frac{1}{N^2} \text{variance}[\vec{I}_1 + \vec{I}_2 + \dots + \vec{I}_N]} \\ &= \frac{1}{N} \sqrt{\text{variance}[\vec{I}_1] + \text{variance}[\vec{I}_2] + \dots + \text{variance}[\vec{I}_N]} = \frac{1}{N} \sqrt{N\sigma^2} = \frac{\sigma}{\sqrt{N}} \end{aligned} \quad (1.17)$$

where σ is a constant, being equal to the standard deviation of I_i . Following the same

procedure in the fully-polarized case we obtain, $|B_{N, \text{fully unpolarized}}| \approx \frac{A}{g \mu_B \sqrt{N}}$. Thus the

effective nuclear magnetic field (and hence the strength of the hyperfine interaction) is

reduced by a factor of \sqrt{N} . In case of GaAs, $N \approx 10^5$, which implies a reduction in the

hyperfine field by a factor of 300 in case of unpolarized nuclear spin configuration

compared to the fully-polarized version. This means that as the nuclear spin configuration

gets more depolarized, strength of the hyperfine field decreases.

It is also instructive to calculate the order of magnitude of the hyperfine interaction. Let us take the example of GaAs. ^{69}Ga ($I = 3/2$) has a nuclear magnetic moment of $2.016 \mu_N$ with natural abundance of 60.4%, ^{71}Ga ($I = 3/2$) has a nuclear magnetic moment of $2.562 \mu_N$ with natural abundance of 39.6%, and ^{75}As ($I = 3/2$) has a nuclear magnetic moment of $1.439 \mu_N$ with natural abundance of 100%. The average nuclear magnetic moment μ_I is calculated as follows:

$$\mu_I = \frac{2.016 \times 60.4 + 2.562 \times 39.6 + 1.439 \times 100}{100 + 100} = 1.8356 \text{ (in units of nuclear magneton } \mu_N \text{)}$$

Using this value of μ_I , total I of $9/2$ and $n_0 = 45.6/\text{nm}^3$, we get $A \approx 100 \mu\text{eV}$. This is the strength of the hyperfine coupling acting on the electron spin in presence of a fully polarized nuclear spin configuration. The corresponding hyperfine magnetic field in GaAs is $\sim 5\text{T}$! Thus if the nuclear spins are polarized, they can produce quite strong Overhauser field at the location of the spin qubit. Following the same recipe, we obtain $\mu_I \approx -0.07844 \mu_N$ and $A \approx 10 \mu\text{eV}$ for CdS.

1.4.2 Electron spin dephasing due to nuclear hyperfine field

Electron spin dephasing in presence of hyperfine field consists of three sub-processes: (1) precession of electron spin in the “frozen” hyperfine field of nuclei, (2) precession of nuclear spins in the hyperfine field of the electron, and (3) nuclear spin relaxation due to dipole-dipole interaction between neighboring nuclear spins. The timescales for these processes has been estimated for GaAs, whose hyperfine constants are well known. For quantum dots containing 10^5 nuclei they are found to be $\sim 1\text{ns}$, $0.1\text{-}1 \mu\text{s}$, and $\sim 100 \mu\text{s}$

respectively [59]. Therefore electron spin dephasing can be described as a precession in the quasi-stationary frozen hyperfine field of the nuclei. A formula for the spin dephasing time (T_2^*) in an ensemble of quantum dots was derived in reference [59] using this physical picture. Spin dephasing occurs due to inhomogeneous broadening of the hyperfine magnetic field over an ensemble of quantum dots. This formula is as follows

$$T_2^* = \hbar \sqrt{\frac{3}{2 \sum_j I^j (I^j + 1) (A^j)^2}} \quad (1.18)$$

assuming all nuclei in the unit cell contributes in spin dephasing, j being the nuclear spin index. We will use this formula in Chapter 8 to analyze and understand the experimental data obtained from electron spin resonance experiments. Our experimental data agrees reasonably well with this model. This is also consistent with the experimentally observed dependence of T_2^* on temperature.

1.5 This dissertation

The chapters in this dissertation are to a large extent self-contained. The amount of redundancy is however kept to a minimum for those reading this dissertation from the beginning to the end. A brief outline of each chapter is described below:

(a) *Chapter 2*: In this chapter we consider D'yakonov-Perel' spin relaxation process in a quantum wire and point out that it is not correct to describe spin and charge diffusion by the same diffusion constant D . We also indicate the necessary conditions for D'yakonov-Perel' mechanism to take place in quantum wire geometry.

(b) *Chapter 3*: In this chapter we consider the D'yakonov-Perel' process in a multi-subband quantum wire in the presence of scattering. To study this problem we have employed a semiclassical formalism that couples Boltzmann transport equation with spin density matrix evolution. We have found that spin relaxation length (limited by D'yakonov-Perel' mechanism only) is ~ 10 microns at low temperatures. This is at least an order of magnitude improvement on what has been calculated in two-dimensional systems for similar values of temperature and bias. We also indicate the physical reason for this improvement.

(c) *Chapter 4*: In this chapter we consider the spin relaxation of "upstream" electrons due to D'yakonov-Perel' mechanism. We show that spatial decay of spin polarization is non-exponential which is in direct contradiction with the claims of the drift-diffusion model.

(d) *Chapter 5*: In this chapter we consider the problem of spin fluctuation and spin noise. We show that the D'yakonov-Perel' mode is indeed a very efficient mechanism of spin relaxation that erases any long term memory of initial spin in an ensemble.

(e) *Chapter 6*: In this chapter we describe the spin transport experiment performed on Ni-Cu-Co nanowire spin valves. We have extracted the spin relaxation length and spin relaxation time in this system and identified the dominant spin relaxation mechanism in Cu.

(f) *Chapter 7*: In this chapter we describe the spin transport experiment performed on Ni-Al₃-Co nanowire spin valves. Spin relaxation time in this system is extremely long, approaching a few seconds at low temperatures. This result establishes organic semiconductors (e.g. Al₃) as an ideal platform for spintronics.

(g) *Chapter 8*: In this chapter we describe our preliminary results on measurements of ensemble averaged spin dephasing time in self-assembled cadmium sulfide quantum dots using an electron spin resonance technique.

CHAPTER 2. Spin Relaxation in Time versus Space: The Difference between Charge and Spin Diffusion Constants*

Overview

Drift-diffusion models of spin transport tacitly assume that the diffusion coefficients describing charge and spin diffusion are the same. In this chapter we will show that this is generally incorrect. The two diffusion coefficients can be vastly different. We highlight this with the extreme example of spin transport in a quantum wire where a *single subband* is occupied and spin relaxation occurs via the D'yakonov-Perel' mode. In this case, the spin diffusion coefficient is infinite even though the charge diffusion coefficient is finite. We also show that there is a difference between spin relaxation in time and in space. Spin can relax in time even when it does not relax in space. We also point out the necessary conditions for D'yakonov-Perel' spin relaxation in a quantum wire and indicate the pathways to eliminate it.

* Publications based on this chapter:

[71] S. Pramanik, S. Bandyopadhyay, and M. Cahay, "Spin relaxation in the channel of a spin field-effect transistor," *IEEE Transactions on Nanotechnology*, vol. 4, pp. 2-7, 2005 and

[72] S. Pramanik, S. Bandyopadhyay, and M. Cahay, "The inequality of charge and spin diffusion coefficients," *submitted*.

2.1 Introduction

The drift-diffusion theory of (bipolar) charge transport and spin transport, in the absence of spin-charge coupling and/or spin accumulation processes (e.g. spin Hall effect [73]), is based on the following two equations [74-77]:

$$\frac{\partial n}{\partial t} - [\mathbf{D}] \frac{\partial^2 n}{\partial x_j^2} - [\mathbf{A}] \frac{\partial n}{\partial x_j} = -[\mathbf{B}] n \quad (2.1a)$$

$$\frac{\partial n_\sigma}{\partial t} - [\mathbf{D}] \frac{\partial^2 n_\sigma}{\partial x_j^2} - [\mathbf{C}] \frac{\partial n_\sigma}{\partial x_j} = -[\mathbf{E}] n_\sigma \quad (2.1b)$$

where n is the electron density (qn is the charge density), and n_σ is the density of electrons having a particular spin σ . Generally, $[\mathbf{A}]$, $[\mathbf{B}]$, $[\mathbf{C}]$, $[\mathbf{D}]$ and $[\mathbf{E}]$ are dyadics (9 component tensors) [38, 78], but in the simplest case, they reduce to scalars, so that the above equations simplify to:

$$\frac{\partial n}{\partial t} - D \frac{\partial^2 n}{\partial x^2} - \hat{\alpha} \frac{\partial n}{\partial x} = -\frac{n}{\tau} \quad (2.2a)$$

$$\frac{\partial n_\sigma}{\partial t} - D \frac{\partial^2 n_\sigma}{\partial x^2} - \hat{\beta} \frac{\partial n_\sigma}{\partial x} = -\frac{n_\sigma}{\tau_s} \quad (2.2b)$$

where D is the particle (or charge) diffusion constant, τ_s is the spin relaxation time and τ is the electron-hole recombination time. The quantities $\hat{\alpha}$ and $\hat{\beta}$ are proportional to the electric field driving transport. Unless this field is very large, the third terms in the above two equations can be neglected, so that the steady-state solution of equation (2.2b) is: $n_\sigma(x) = n_\sigma(0) \exp(-x/L_s)$ where

$$L_s = \sqrt{D\tau_s} \quad (2.3)$$

Here L_s is the spin diffusion length. Similarly, the steady state solution of equation (2.2a) is $n(x) = n(0) \exp(-x/L_D)$ where L_D is the charge diffusion length given by

$$L_D = \sqrt{D\tau} \quad (2.4)$$

In equations (2.1) – (2.4), it is tacitly assumed that the same diffusion constant “ D ” describes charge transport and spin transport. This assumption is commonplace in the literature (see, for example, references [38, 74-76, 79]). Reference [80] considers a two-dimensional system with different spin and charge diffusion constants but ultimately assumes that the bare spin diffusion constant is the same as the charge diffusion constant. Reference [81] also examines this issue, and based on an heuristic assumption that spin transport is analogous to bipolar charge transport, reaches the conclusion that the two diffusion coefficients are equal as long as the populations of upspin and downspin carriers are equal. In spin polarized transport, the two populations are unequal by definition. Therefore, it is imperative to examine if these two diffusion constants are still equal in spin polarized transport, and if not, then how unequal they can be. In this chapter we will show that these two diffusion coefficients are vastly different. In fact, in one case, the spin diffusion constant D_s can be infinite when the charge diffusion constant D_c is finite. We show this analytically. We also show that there is an essential difference between spin relaxation in time and spin relaxation in space. The system where it happens is a semiconductor quantum wire where only the lowest subband is occupied at all times and spin relaxation occurs via the D’yakonov-Perel’ mechanism [32, 33]. In the following section we will show analytically that in this system charge and spin diffusion constants are vastly unequal. When multiple subbands are occupied, D_s is finite but still it is several orders of magnitude larger than the charge diffusion constant D_c in the same system.

2.2 Analytical proof that $D_c \neq D_s$

Consider an ensemble of electrons injected in a quantum wire at time $t = 0$ from the end $x = 0$ as shown in Figure 2.1. Only the lowest subband is occupied in the wire at all times. There is an electric field E_x driving charge transport, and there is also a transverse “gate” electric field ($E_y \hat{y}$) breaking structural inversion symmetry, thereby causing a Rashba spin-orbit interaction [28]. This structure mimics the configuration of a spin interferometer [9]. We will assume that the quantum wire axis is along the [100] crystallographic direction and that there is crystallographic inversion asymmetry along this direction giving rise to Dresselhaus spin-orbit interaction [26]. We choose this system because it is the simplest. Reference [79] has considered this system within the framework of drift-diffusion model and shown that there is a single time constant describing spin relaxation. In contrast, spin relaxation in a two-dimensional system (quantum well) may be described by more than one time constant [79]. For illustration purposes, we will assume hypothetically that the spin injection efficiency is 100%, so that at $x = 0$, all electrons are spin polarized along some particular, though arbitrary, direction $\hat{\eta}_0$ in space. Their injection velocities are not necessarily the same. We are interested in finding out how the net spin polarization of the ensemble, $\left| \langle \vec{S} \rangle \right|$, decays in time or space due to the D’yakonov-Perel’ process. In the quantum wire, the electrons experience various momentum relaxing scattering events. Between successive scattering events, they undergo free flight and during this time, their spins precess about a velocity-dependent pseudo-magnetic field $\vec{B}_{SO}(v_x)$ caused by Rashba and Dresselhaus spin-orbit interactions. This field is related to the spin-orbit

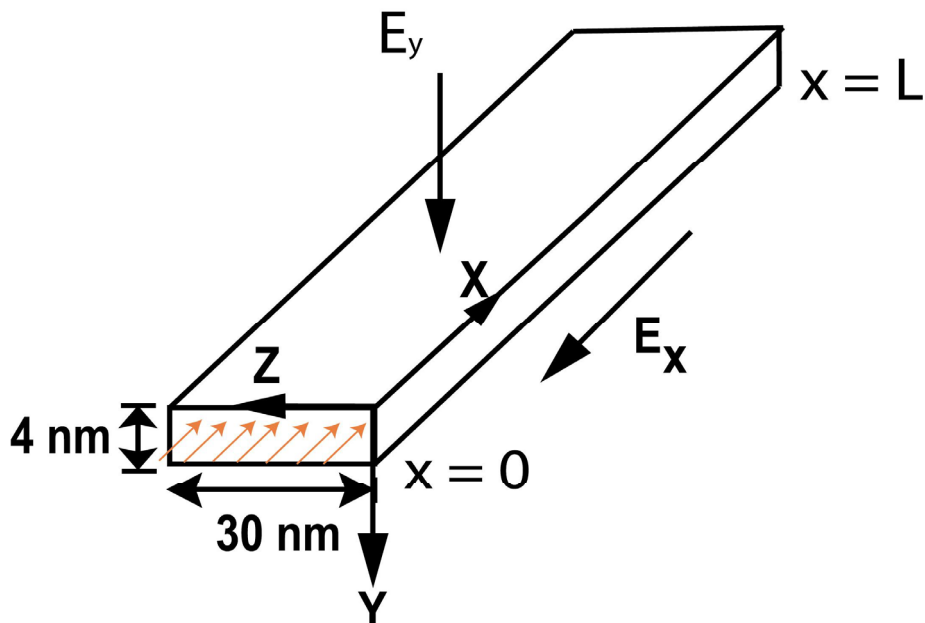


Figure 2.1 Geometry of the quantum wire. Here E_x is the longitudinal electric field that drives transport. The transverse electric field E_y induces Rashba spin-orbit coupling. The orange arrows indicate spin polarized (along x) electron injection in the quantum wire channel from $x = 0$ at time $t = 0$. Clearly at $x = 0$ (and $t = 0$), $\langle S_x \rangle = 1$, $\langle S_y \rangle = \langle S_z \rangle = 0$ and $|\langle \mathbf{S} \rangle| = 1$, where $\langle \rangle$ indicates ensemble averaging over the entire electron population. As these electrons travel along the channel under the influence of transport driving electric field E_x , their initial spin orientations change due to spin-orbit coupling effects in the quantum wire channel. The strength of this spin-orbit coupling effect depends on electron velocity v_x as well as on the subband indices. Thus each electron experiences different spin-orbit coupling and hence spins of different electrons are rotated by different angles. Thus at $t > 0$, different electrons have different spin orientations and $|\langle \mathbf{S} \rangle| (t > 0) < 1$. This is the D'yakonov-Perel' mechanism of spin relaxation. We are interested in finding out how $|\langle \mathbf{S} \rangle|$ evolves in time as well as in space (i.e. along the quantum wire channel).

interaction Hamiltonian H_{SO} as

$$H_{SO} = (g/2)\mu_B \vec{\sigma} \cdot \vec{B}_{SO}(v_x) \quad (2.5)$$

where μ_B is the Bohr magneton, g is the g -factor, $\vec{\sigma} = \sigma_x \hat{x} + \sigma_y \hat{y} + \sigma_z \hat{z}$, with σ_i ($i = x, y, z$) being the Pauli spin matrix, and v_x is the electron velocity along the wire axis. The spin precession occurs according to the equation

$$\frac{d\vec{S}}{dt} = \vec{\Omega}(v_x) \times \vec{S} \quad (2.6)$$

where \vec{S} is the spin polarization vector and $\vec{\Omega}(v_x)$ is a vector whose magnitude is the angular frequency of spin precession. It is related to $\vec{B}_{SO}(v_x)$ as $\vec{\Omega}(v_x) = (q/m^*)B_{SO}(v_x)$ where q is the magnitude of the electronic charge and m^* is the electron's effective mass.

The precession vector $\vec{\Omega}(v_x)$ has two orthogonal components due to Rashba and Dresselhaus interactions:

$$\vec{\Omega}(v_x) = \vec{\Omega}_D(v_x) + \vec{\Omega}_R(v_x) \quad (2.7)$$

where the first term is the Dresselhaus and the second term is the Rashba contribution.

These two contributions are given by

$$\vec{\Omega}_D(v_x) = \frac{2m^* a_{42}}{\hbar^2} \left[\left(\frac{m\pi}{W_z} \right)^2 - \left(\frac{n\pi}{W_y} \right)^2 \right] v_x \hat{x} \equiv \xi_{DO} v_x \hat{x} \quad (2.8a)$$

$$\vec{\Omega}_R(v_x) = \frac{2m^* a_{46}}{\hbar^2} E_y v_x \hat{z} \equiv \xi_{RO} v_x \hat{z} \quad (2.8b)$$

where W_y and W_z are the transverse dimensions of the wire (m and n are the respective subband indices), a_{42} and a_{46} are material constants, \hat{x} is the unit vector along the x axis,

which coincides with the axis of the channel and \hat{z} is the unit vector along the z -direction.

In the present case, when transport takes place via the lowest subband, $m = n = 1$.

Note that the precession vector $\vec{\Omega}(v_x)$ lies in the $x-z$ plane. The angle θ that $\vec{\Omega}$ makes with the channel axis (\hat{x}) is given by

$$\theta = \arctan \left[\frac{\xi_{RO}}{\xi_{DO}} \right] = \arctan \left[\frac{a_{46} E_y}{a_{42} \left\{ \left(\frac{m\pi}{W_z} \right)^2 - \left(\frac{n\pi}{W_y} \right)^2 \right\}} \right] \quad (2.9)$$

which is independent of electron velocity v_x , but depends only on m and n . In the present case, since only the lowest subband is occupied during transport, θ is the same for all electrons. This means that the precession axis is fixed for all electrons but the magnitude of the precession frequency is different for different electrons. Thus, every electron, regardless of its velocity, precesses about the same axis, as long as only one subband is occupied. The direction of precession (clockwise or counter-clockwise) depends on the sign of the velocity and therefore can change if the velocity changes sign, but the precession axis remains unchanged. However, the precession frequency depends on the velocity and is therefore different for different electrons as long as there is a spread in their velocities caused by varying injection conditions or random scattering. As a result, when we ensemble average over all electrons, the quantity $\langle \vec{S} \rangle$ decays in time, leading to spin relaxation *in time*.

To show this more clearly, we start from equation (2.6).

$$\begin{aligned}
\frac{d\vec{S}}{dt} &= \hat{x} \frac{dS_x}{dt} + \hat{y} \frac{dS_y}{dt} + \hat{z} \frac{dS_z}{dt} \\
&= \vec{\Omega}(v_x) \times \vec{S} \\
&= \det \begin{bmatrix} \hat{x} & \hat{y} & \hat{z} \\ \Omega_D(v_x) & 0 & \Omega_R(v_x) \\ S_x & S_y & S_z \end{bmatrix} \\
&= -\hat{x} [\Omega_R(v_x) S_y] - \hat{y} [\Omega_D(v_x) S_z - \Omega_R(v_x) S_x] + \hat{z} [\Omega_D(v_x) S_y]
\end{aligned} \tag{2.10}$$

where $S_n (n = x, y, z)$ is the spin component along the n -axis. Equating each component separately we get

$$\begin{aligned}
\frac{dS_x}{dt} &= -\xi_{RO} v_x S_y \\
\frac{dS_y}{dt} &= \xi_{RO} v_x S_x - \xi_{DO} v_x S_z \\
\frac{dS_z}{dt} &= \xi_{DO} v_x S_y
\end{aligned} \tag{2.11}$$

If every electron had the same v_x , then we could replace every spin component S_n in the last equation by its ensemble averaged value $\langle S_n \rangle$, so that

$$\begin{aligned}
\frac{d\langle \vec{S} \rangle^2}{dt} &= \frac{d\langle S_x \rangle^2}{dt} + \frac{d\langle S_y \rangle^2}{dt} + \frac{d\langle S_z \rangle^2}{dt} \\
&= 2\langle S_x \rangle \frac{d\langle S_x \rangle}{dt} + 2\langle S_y \rangle \frac{d\langle S_y \rangle}{dt} + 2\langle S_z \rangle \frac{d\langle S_z \rangle}{dt} \\
&= -2\xi_{RO} v_x \langle S_y \rangle \langle S_x \rangle + 2\xi_{RO} v_x \langle S_x \rangle \langle S_y \rangle - 2\xi_{DO} v_x \langle S_y \rangle \langle S_z \rangle + 2\xi_{DO} v_x \langle S_y \rangle \langle S_z \rangle \\
&= 0
\end{aligned} \tag{2.12}$$

In that case, $\langle \vec{S} \rangle$ will not decay in time and there will be no D'yakonov-Perel' spin relaxation in time. However, if v_x is different for different electrons either due to different injection conditions, or because of scattering, then we cannot replace S_n by $\langle S_n \rangle$ in

equation (2.11). As a result, $\frac{d\langle\vec{S}\rangle}{dt} \neq 0$, and there will be a D'yakonov-Perel' relaxation in time. To establish this, we show results of Monte Carlo simulation of D'yakonov-Perel' spin relaxation in time in Figure 2.2. The system studied is the one in Figure 2.1. The details about the simulator is available elsewhere [46, 82] and will not be repeated here. We inject \hat{x} polarized electrons in the lowest subband of the quantum wire (Figure 2.1). They suffer intra-subband scattering due to interactions with phonons, which randomly change their velocities. We then study the temporal decay of ensemble averaged spin components.

The electric field and temperature are kept low enough that no electron transitions to a higher subband by inter-subband scattering. From this simulation we observe that the decay of spin with time is not exponential, but at least monotonic. We find τ_s (defined as the time taken for $\langle\vec{S}\rangle$ to decay to $1/e$ times its initial value at $t = 0$) to be about 10 nsec at 30 K, when the driving electric field is 0.5 kV/cm. This is a standard method, and has been used by, for example, Kim and Kiselev in reference [83]. The exact value of τ_s is not important here. We only stress that τ_s is finite for diffusive transport in a quantum wire, even if transport occurs via a single channel. Spin dephasing time is expected to increase as we reduce the driving electric field [46, 82]. But even in the zero-field limit, when transport takes place only by diffusion and there is no drift, τ_s will be *finite* according to the physical picture presented here.

Next, let us consider D'yakonov-Perel' spin relaxation in *space*. From equation (2.11) we obtain (using the simple chain rule of differentiation)

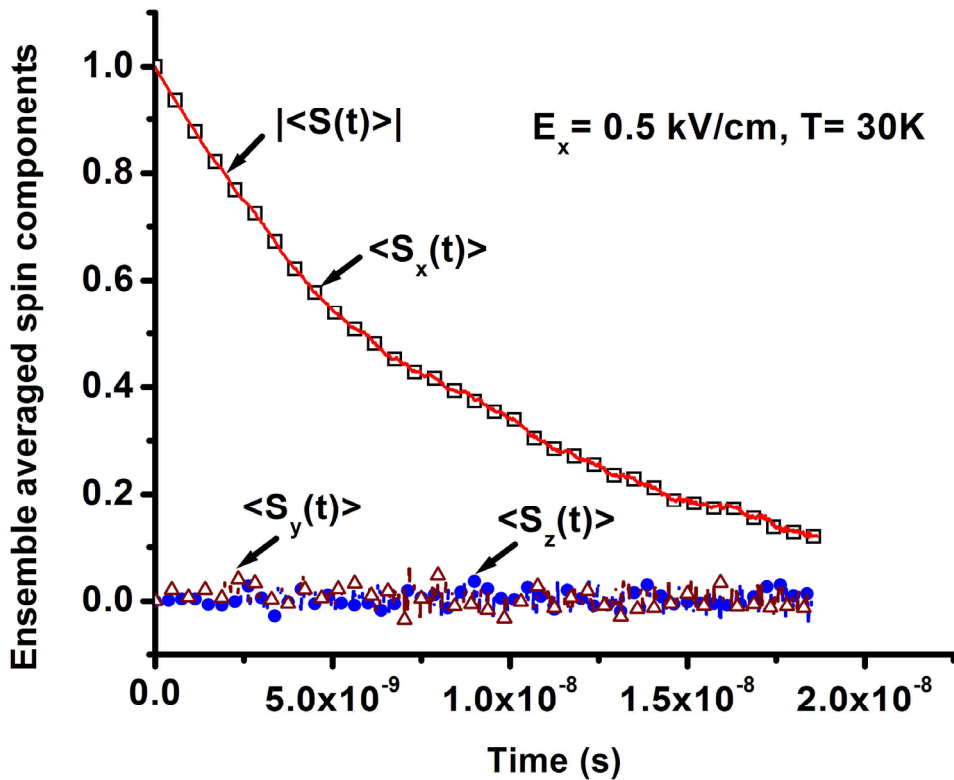


Figure 2.2 Temporal decay of ensemble averaged spin components as calculated using Monte Carlo simulator. The quantum wire material is GaAs and $E_y = 100$ kV/cm. Injected spins are all polarized along \hat{x} and occupy the lowest subband during transport. The simulation is based on the model depicted in Figure 2.1. The spin diffusion time is approximately 10 ns at 30 K and driving field of 0.5 kV/cm. This low field and low temperature ensure that the second subband is not occupied.

$$\begin{aligned}
\frac{dS_x}{dx} \frac{dx}{dt} &= \frac{dS_x}{dx} v_x = -\xi_{RO} v_x S_y \\
\frac{dS_y}{dx} \frac{dx}{dt} &= \frac{dS_y}{dx} v_x = \xi_{RO} v_x S_x - \xi_{DO} v_x S_z \\
\frac{dS_z}{dx} \frac{dx}{dt} &= \frac{dS_z}{dx} v_x = \xi_{DO} v_x S_y
\end{aligned} \tag{2.13}$$

In this case, even if different electrons have different velocities, it does not matter since the spatial rates $\frac{dS_n}{dx}$ are *independent* of velocity. Therefore we can always replace S_n in the above equation by its ensemble averaged value $\langle S_n \rangle$ whether or not there is scattering causing a spread in the electron velocity. Consequently,

$$\begin{aligned}
\frac{d\langle \bar{S} \rangle^2}{dx} &= \frac{d\langle S_x \rangle^2}{dx} + \frac{d\langle S_y \rangle^2}{dx} + \frac{d\langle S_z \rangle^2}{dx} \\
&= 2\langle S_x \rangle \frac{d\langle S_x \rangle}{dx} + 2\langle S_y \rangle \frac{d\langle S_y \rangle}{dx} + 2\langle S_z \rangle \frac{d\langle S_z \rangle}{dx} \\
&= -2\xi_{RO} \langle S_y \rangle \langle S_x \rangle + 2\xi_{RO} \langle S_x \rangle \langle S_y \rangle - 2\xi_{DO} \langle S_y \rangle \langle S_z \rangle + 2\xi_{DO} \langle S_y \rangle \langle S_z \rangle = 0
\end{aligned} \tag{2.14}$$

Thus there is never any D'yakonov-Perel' relaxation in space as long as a single subband is occupied. This is true whether or not there is any intra-subband scattering. In Figure (2.3) we show a Monte Carlo simulation result to show this [71].

What we have shown is that in a quantum wire with single subband occupancy and D'yakonov-Perel' as the only spin relaxation mechanism, there is a fundamental difference between spin relaxation in *time* and spin relaxation in *space*. The physical origin of this difference is explained below:

The precession frequency is given by

$$\Omega \equiv \frac{d\varphi(t)}{dt} = \sqrt{\xi_{DO}^2 + \xi_{RO}^2} v_x(t) \equiv \xi_O v_x(t) \tag{2.15}$$

If all electrons are injected with the same spin polarization at $t = 0$, then the angle by which any given electron's spin has precessed at time $t = t_0$ is

$$\varphi(t_0) = \xi_0 \int_0^{t_0} v_x(t) dt = \xi_0 [x(t_0) - x(0)] = \xi d_0 \quad (2.16)$$

where d_0 is the distance between the location of the electron at time t_0 and the point of injection. Obviously d_0 is *history-dependent*, because different electrons with different

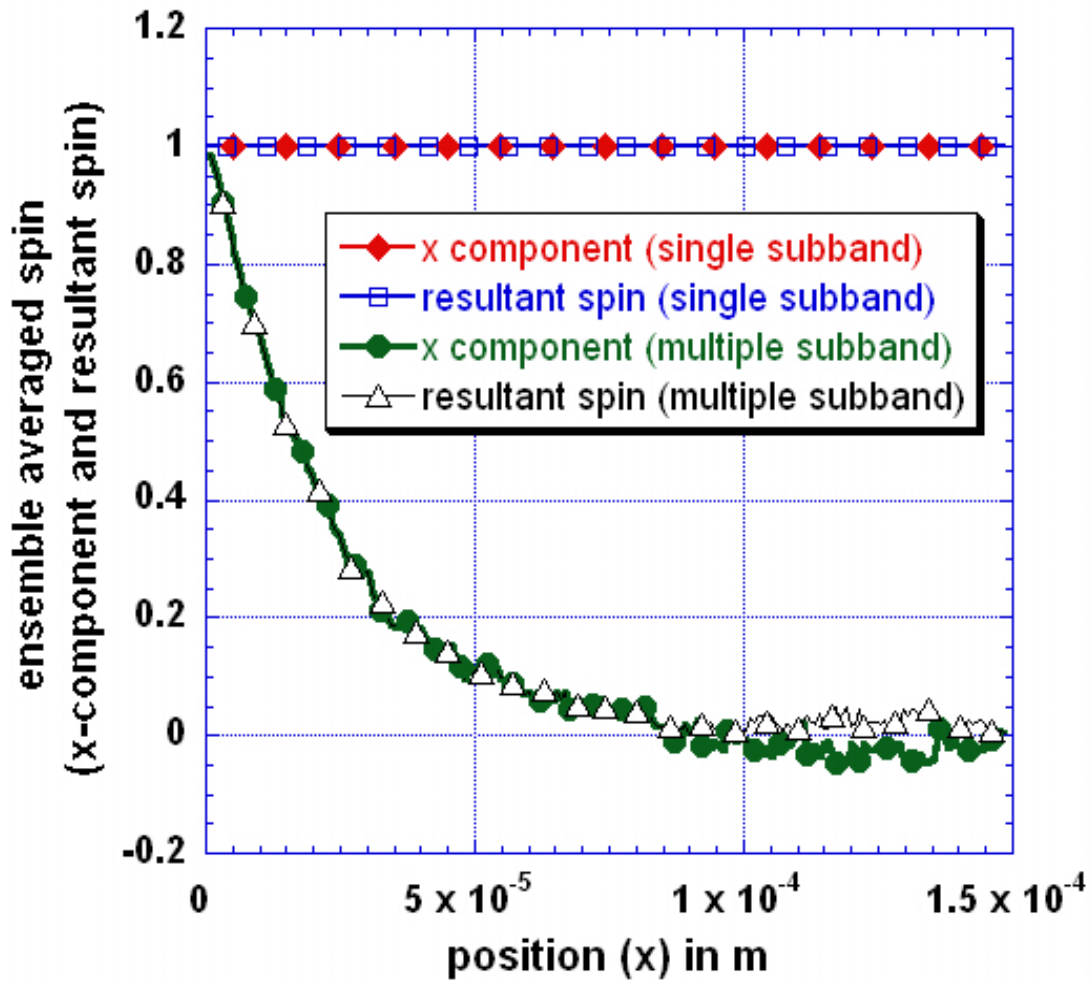


Figure 2.3 Spatial spin relaxation in a GaAs quantum wire as described in Figure 2.1. The driving electric field is 2 kV/cm and lattice temperature is 30 K. These results are obtained from Monte Carlo simulation. Spin does not relax for single-channelled (single-subband) transport but does relax for multi-channelled transport.

injection velocities and/or scattering histories would traverse different distances in time t_0 . Consequently, if we denote the angle by which the n th electron's spin has precessed in time t_0 as $\varphi_n(t_0)$, then $\varphi_1(t_0) \neq \varphi_2(t_0) \neq \dots \neq \varphi_m(t_0)$. As a result, if we take a snapshot at t_0 , we will find that the spin polarization vectors of different electrons are pointing in different directions. Therefore, ensemble averaged spin at t_0 is less than what it was at time $t = 0$. Consequently, spin depolarizes with time leading to D'yakonov-Perel' relaxation.

The spatial rate of precession, on the other hand, is obtained as

$$\begin{aligned}\Omega(t) &\equiv \frac{d\varphi(t)}{dt} = \frac{d\varphi(x)}{dx} \frac{dx}{dt} = \sqrt{\xi_{DO}^2 + \xi_{RO}^2} v_x(t) \\ \Rightarrow \Omega(x) &= \frac{d\varphi(x)}{dx} = \sqrt{\xi_{DO}^2 + \xi_{RO}^2} \equiv \xi_O\end{aligned}\tag{2.17}$$

Therefore, the angle by which any given electron's spin has precessed when it arrives at a location $x = X_0$ is

$$\varphi(X_0) = \int_0^{X_0} \frac{d\varphi(x)}{dx} dx = \xi_O \int_0^{X_0} dx = \xi_O X_0\tag{2.18}$$

This angle is obviously *history-independent* since it depends only on the coordinate X_0 which is the same for all electrons at location X_0 , regardless of how and when they arrived at that location. In fact, an electron may have visited the location X_0 earlier, gone past it, and then scattered back to X_0 . Or it may have arrived at X_0 for the first time. It does not matter. Regardless of the past history, the angle by which an electron's spin has precessed when it is located at X_0 is a constant. Therefore every single electron at $x = X_0$ has its spin polarization vector pointing in the *same* direction, and the ensemble averaged spin at $x =$

X_0 is the same as that at $x = 0$. Therefore spin does not depolarize in space and there is no D'yakonov-Perel' spin relaxation in space, unlike time.

2.3 Spin diffusion constant and charge diffusion constant

Since spin relaxes in time but not in space, the relaxation time τ_s is finite whereas the relaxation length L_s is infinite. Therefore, the fact that $L_s = \infty$, but $\tau_s \neq \infty$, implies spin diffusion constant D_s is infinite, according to equation (2.3). But the diffusion constant D_c associated with charge transport is certainly finite since we have frequent momentum relaxing scattering in our system. Therefore, the only way to reconcile these facts is to postulate that there are two very different diffusion constants D_s and D_c associated with spin and charge diffusion. This completes our analytical proof that $D_c \neq D_s$.

One final question remains, namely how general is the above result. Is it only valid for a quantum wire with single subband occupancy? The answer is negative. To show this we considered a quantum wire with multi-subband occupancy. Here there is D'yakonov-Perel' relaxation in both time and space [46, 47, 71] and one could extract a finite value of the spin diffusion constant D_s from equation (2.3) provided we can calculate L_s and τ_s . We have carried out this exercise. In Chapter 3 we will report our studies on multisubband spin transport in a quantum wire. The value of L_s extracted from that study is $\sim 10 \mu m$ at low temperatures. On the other hand, the value of $\tau_s \sim 1 ns$ [46]. This yields $D_s = 10^3 \text{ cm}^2/\text{s}$ (from equation (2.3)) which is still several orders of magnitude higher than the charge diffusion constant D_c in the same quantum wire under the same conditions [84-86]. Thus $D_s \neq D_c$, in general, and the two quantities can be vastly different.

2.4 Necessary conditions for D'yakonov-Perel' spin relaxation in space

It is quite straightforward to deduce the spatial variation of individual spin components from equation (2.13). We will not show the derivation here, but leave it as an exercise for the curious reader. We only write down the final result:

$$\begin{aligned}
 S_x(x) &= \frac{\beta^2(m,n) + (a_{46}E_y)^2 \cos \gamma(m,n)x}{(a_{46}E_y)^2 + \beta^2(m,n)} \\
 S_y(x) &= \frac{a_{46}E_y \sin \gamma(m,n)x}{\sqrt{(a_{46}E_y)^2 + \beta^2(m,n)}} \\
 S_z(x) &= \frac{2a_{46}E_y \beta(m,n)}{(a_{46}E_y)^2 + \beta^2(m,n)} \sin^2 \frac{\gamma(m,n)x}{2}
 \end{aligned} \tag{2.19}$$

where $\beta(m,n) = a_{42} \left[\left(\frac{m\pi}{W_z} \right)^2 - \left(\frac{n\pi}{W_y} \right)^2 \right]$, and $\gamma(m,n) \equiv \Omega_0 = \frac{2m^*}{\hbar^2} \sqrt{(a_{46}E_y)^2 + \beta^2(m,n)}$

It has been assumed that injected spin polarizations point along \hat{x} . From these equations, we can identify the necessary conditions for (spatial) D'yakonov-Perel' spin relaxation to take place in a quantum wire.

2.4.1 Rashba interaction

We can immediately see from the “boxed” equations derived above that if there is no Rashba interaction ($a_{46} = 0$ or, $E_y = 0$), then at all positions x , $\langle S_x(x) \rangle = 1$, $\langle S_y(x) \rangle = 0$ and

$\langle S_z(x) \rangle = 0$. This implies $\left| \langle \vec{S}(x) \rangle \right| = \sqrt{\langle S_x(x) \rangle^2 + \langle S_y(x) \rangle^2 + \langle S_z(x) \rangle^2} = 1, \forall x$. As

described earlier, here, the angular bracket $\langle \dots \rangle$ denote ensemble average over the entire electron population and $\left\langle \vec{S}(x) \right\rangle$ is the ensemble averaged spin vector at position x . Thus we infer that as long as the electrons are injected in the quantum wire channel with their spins polarized along the axis of the wire, there is no D'yakonov-Perel' spin relaxation, since the ensemble averaged spin $\left\langle \vec{S}(x) \right\rangle$ does not decay at all. Therefore Rashba interaction is a necessary ingredient for ensemble averaged spin to relax.

It is possible to furnish a physical explanation of this phenomenon. In absence of Rashba interaction, the only spin-orbit magnetic field in the channel is due to bulk inversion asymmetry which points along $\pm \hat{x}$ (depending on the sign of v_x , see equations (2.8)). We are injecting electrons with spins polarized along \hat{x} . Clearly there will be no spin precession as the cross product of two collinear vectors cancels out. It does not matter even if different electrons experience different spin-orbit magnetic fields (i.e. if they are occupying different subbands or have different velocities). Since the injected spins are collinear with the spin-orbit magnetic field, they are immune to its presence.

There is a second possible way of looking into this issue. In case of a quantum wire, Dresselhaus spin-orbit coupling is proportional to the x component of Pauli spin matrix with eigenspinors pointing along $\pm \hat{x}$. Thus when electrons with spins polarized along \hat{x} enter the channel, they find themselves in one of the stationary states of the channel implying no temporal (and hence spatial) evolution.

Thus, in a III-V quantum wire, if there is no Rashba interaction present in the system, D'yakonov-Perel' mechanism of spin relaxation (in space) will be completely eliminated.

2.4.2 Dresselhaus interaction

If there is no Dresselhaus interaction (i.e. $a_{42} = 0$) then from equations (2.19) we have

$$\langle S_x(x) \rangle = \cos\left(\frac{2m^* a_{46} E_y}{\hbar^2}\right), \quad \langle S_y(x) \rangle = \sin\left(\frac{2m^* a_{46} E_y}{\hbar^2}\right), \quad \text{and} \quad \langle S_z(x) \rangle = 0 \quad \text{for any } 0 < x < L.$$

Therefore the magnitude of ensemble averaged spin vector

$$\left| \langle \vec{S}(x) \rangle \right| = \sqrt{\langle S_x \rangle^2 + \langle S_y \rangle^2 + \langle S_z \rangle^2} = 1, \quad \text{for all values of } x. \quad \text{Again, we see that the ensemble}$$

averaged spin does not decay. In this case the ensemble averaged spin vector rotates in the xy plane (the z polarization remains zero), but the amplitude of this oscillation does not decay. Therefore there can be no D'yakonov-Perel' spin relaxation without Dresselhaus interaction.

The physical picture is as follows: in absence of Dresselhaus interaction, the only spin-orbit magnetic field in the quantum wire channel is due to the Rashba interaction which is pointing along $\pm \hat{z}$ (depending on the orientation of v_x). The injected \hat{x} polarized spins precess about this magnetic field like a spinning top, the plane of precession being the xy plane. In this case, the Rashba spin orbit magnetic field is different for different electrons since it is a function of electron velocity. Indeed, if we compute the temporal evolution of ensemble averaged spin vector, it will decay with time. The reason being at a given instant of time spins of different electrons will rotate by different amounts resulting in temporal spin dephasing. However, there will be no dephasing in space because v_x cancels out in quantum wire geometry (as described before). Thus in a quantum wire, if Dresselhaus interaction is absent, there will no D'yakonov-Perel' spin relaxation in space.

2.4.3 Multichanneled transport

If both Rashba and Dresselhaus interactions are present, but transport is single channeled i.e. $m = m_0$, $n = n_0$, then every electron is in the same subband (m_0, n_0) . In that case

$$\begin{aligned}\langle S_x(x) \rangle &= \frac{\beta_0^2 + (a_{46} E_y)^2 \cos \gamma_0 x}{(a_{46} E_y)^2 + \beta_0^2} \\ \langle S_y(x) \rangle &= \frac{a_{46} E_y \sin \gamma_0 x}{\sqrt{(a_{46} E_y)^2 + \beta_0^2}} \\ \langle S_z(x) \rangle &= \frac{2a_{46} E_y \beta_0}{(a_{46} E_y)^2 + \beta_0^2} \sin^2 \frac{\gamma_0 x}{2}\end{aligned}\tag{2.20}$$

where $\beta_0 = \beta(m_0, n_0)$ and $\gamma_0 = \gamma(m_0, n_0)$

Once again it is straightforward to verify that the magnitude of ensemble averaged spin vector is unity for all values of x inside the channel. Consequently there is no D'yakonov-Perel' spin relaxation if the transport is single channeled. This is true regardless whether the electrons are into the lowest subband or any other subband, as long as there is no intersubband scattering.

2.4.4 What is necessary for D'yakonov-Perel' spin relaxation (in space)?

If transport is multichanneled then different electrons at position x occupy different subbands i.e. the subband indices are different for different electrons. As pointed out earlier, this leads to D'yakonov-Perel' spin relaxation. Therefore multichanneled transport, in presence of both Rashba and Dresselhaus interaction leads to D'yakonov-Perel' spin relaxation. It is important to note that "scattering" or intersubband transitions are not necessary for D'yakonov-Perel' spin relaxation. Even if every electron remains in the subband in which it was originally injected, there will be a D'yakonov-Perel' relaxation as

a consequence of ensemble averaging over all electrons. Of course, if there is scattering and intersubband transitions then the subband indices become functions of x , in which case the effect of ensemble averaging is exacerbated and the relaxation will be more rapid. Thus we have established that three conditions are needed for D'yakonov-Perel' spin relaxation in space: (a) Rashba interaction, (b) Dresselhaus interaction and (c) multichanneled transport. All three of these conditions are necessary for D'yakonov-Perel' spin relaxation in space.

2.5 Conclusion

In this chapter we have shown that spin diffusion coefficient and charge diffusion coefficient are vastly different and have established the conditions required for D'yakonov-Perel' spin relaxation in a quantum wire. This relaxation is harmful for most spintronic devices (one example is the spinFET [9]), because it leads to spin randomization. Since optimum materials for spinFET type devices (e.g. InAs) usually possess strong Rashba and also some Dresselhaus spin-orbit interactions, the only effective way to eliminate the D'yakonov-Perel' spin relaxation is to ensure and enforce single channeled transport. There has been some proposals that advocate using multichanneled devices for spinFET, along with the claim that they provide better spin control via the use of multiple gates [87]. While it is unlikely that spin control is improved by using multiple gates, since synchronizing these gates is an additional engineering burden that can only degrade device operation and gate control, it is even more important to understand that multichanneled devices have serious drawbacks. The original proposal for spinFET pointed out that multichanneled transport is harmful because it dilutes the spin interference effect which is the basis of the spinFET device [9]. Here we have pointed out an additional motivation to

avoid multichanneled devices: they will suffer from D'yakonov-Perel' spin relaxation, while the single-channeled device will not.

In Chapter 3 we will describe our study of multisubband spin transport based on a Monte Carlo simulation technique.

CHAPTER 3. D'yakonov-Perel' Spin Relaxation in a Quantum Wire: Multichanneled Transport¹

Overview

In this chapter we study the spatial decay of *spin-polarized hot carrier current* in a spin-valve structure consisting of a semiconductor quantum wire flanked by half-metallic ferromagnetic contacts. The current decays because of D'yakonov-Perel' spin relaxation in the semiconductor caused by Rashba and Dresselhaus spin-orbit interactions in multichanneled transport. The associated relaxation length is found to decrease with increasing lattice temperature (in the range 30 K to 77 K) and exhibit a non-monotonic dependence on the electric field driving current. The relaxation lengths are several tens of microns which are at least an order of magnitude larger than what has been theoretically calculated for two-dimensional structures at comparable temperatures, spin-orbit interaction strengths and electric fields. This improvement is a consequence of one-dimensional confinement that does not necessarily suppress carrier scattering, but nevertheless suppresses D'yakonov-Perel' spin relaxation. As we have observed in the previous chapter, as long as

¹ This chapter has been published as [47] S. Pramanik, S. Bandyopadhyay, and M. Cahay, "Decay of spin-polarized hot carrier current in a quasi-one-dimensional spin-valve structure," *Applied Physics Letters*, vol. 84, pp. 266-268, 2004.

the carriers reside in one particular subband, there is no D'yakonov-Perel' relaxation in space. It is necessary to have *inter-subband scattering* in the system for this mechanism to take place. Intra-subband scattering, however frequent it may be, will not cause D'yakonov-Perel' spin relaxation in space.

3.1 Introduction

In the previous chapter we pointed out that multichanneled transport in presence of both Rashba and Dresselhaus interaction leads to D'yakonov-Perel' spin relaxation in a quantum wire. Thus, in order to suppress this mechanism of spin relaxation it is essential to enforce single channeled transport. However, in general, multiple subbands are occupied by electrons during transport and hence there will be D'yakonov-Perel' spin relaxation in space. In this chapter, we study D'yakonov-Perel' spin relaxation in presence of multichanneled transport in quantum wires and find out spin relaxation length limited by this process.

The model we study here has the spin FET configuration as described before (see Figure 2.1). A quasi-one dimensional semiconductor channel is flanked between two half-metallic ferromagnetic contacts. One contact (called "source") injects spin polarized electrons (or spin polarized current) into the channel and thus acts as a "spin polarizer". The other contact acts as a "spin-analyzer" and is termed the "drain". Carriers drift from the source to the drain under the influence of a driving electric field. When they arrive at the drain, they are transmitted with a probability $|T|^2 = \cos^2\left(\frac{\theta}{2}\right)$ where θ is the angle between the electron's spin polarization at the drain end and the drain's magnetization. With increasing

degree of spin depolarization in the channel (caused by spin relaxation), the average “misalignment angle” θ (for the electron ensemble) increases and consequently the transmitted current decreases. Ultimately, when there is no residual spin polarization in the current (i.e. electrons are equally likely to have their spins aligned parallel or antiparallel to the drain’s magnetization), the transmitted current will fall to 50% of its maximum value. We are interested to find out how the (transmitted) spin polarized current falls off with distance along the channel at different driving fields and temperatures.

As mentioned above, we only focus on D’yakonov-Perel’ mechanism of spin relaxation. In this mechanism, spins depolarize in the channel primarily because of spin-orbit interactions caused by bulk inversion asymmetry (Dresselhaus spin-orbit coupling) and structural inversion asymmetry (Rashba spin-orbit coupling). The spatial decay due to D’yakonov-Perel’ mechanism was studied in the past by Bournel et al. [42-45, 88-91] and Saikin et al. [48, 92-98] in two-dimensional channels. They mostly dealt with low driving electric fields so that transport is linear or quasi-linear. In contrast, we have studied the spatial decay in quasi-1D structures of both spin and spin-polarized current at high driving electric fields of 1 – 10 kV/cm, which result in hot carrier transport and nonlinear effects.

3.2 Theoretical model

In a 1D structure, the spin polarized current due to a single electron is proportional to $q v_x |T|^2$ where q is the electronic charge, v_x is the velocity of the electron, and $|T|^2$ is the transmission probability of the electron through the drain contact. As stated before, the quantity $|T|^2$ depends on the component of the electron’s spin polarization along the

magnetization of the drain. We will assume that the source and drain are both magnetized along the channel's axis (x axis). This results in the initial spin orientation to be along the channel axis. Accordingly,

$$|T|^2 = \cos^2\left(\frac{\theta}{2}\right),$$

$$\cos\theta = \frac{S_x}{\sqrt{S_x^2 + S_y^2 + S_z^2}} = \bar{S}_x \quad (3.1)$$

where S_n is the spin component along the n ($=x, y, z$) axis, and \bar{S}_x is the normalized value of S_x .

The ensemble averaged spin polarized current at any position x is given by

$$I_s(x) = q \sum_{v_x, \bar{S}_x} f(v_x, \bar{S}_x, x) v_x |T(\bar{S}_x)|^2 \quad (3.2)$$

where the velocity (v_x) and spin (\bar{S}_x) dependent distribution function $f(v_x, \bar{S}_x, x)$ at any position x is found directly from the Monte Carlo simulator described in references [46, 82] and will not be repeated here. In this simulator we use a parabolic energy versus velocity dispersion relation

$$E = \frac{\hbar^2}{2m^*} \left(\frac{m\pi}{W_y}\right)^2 + \frac{\hbar^2}{2m^*} \left(\frac{n\pi}{W_z}\right)^2 + \frac{1}{2} m^* v_x^2 \quad (3.3)$$

where m and n are the subband indices along y and z respectively, neglecting any band structure non-parabolicity, which is not important in the energy range encountered. It is possible to introduce some band structure non-parabolicity by using an energy-dependent effective mass. However, this is not important. The carrier kinetic energies remain small in

every subband so that non-parabolicity effects are never significant. If the energy of a carrier in the lowest subband begins to increase, the carrier suffers intersubband transition to a higher subband by absorbing or emitting phonons. This process keeps the kinetic energy in every subband small and the carrier temperature remains very close to the lattice temperature. The intersubband scattering (not intervalley scattering) is also responsible for velocity saturation in the quantum wire.

The dispersion relation in equation (3.3) allows us to calculate the velocity v_x from the carrier energy E and subband indices m and n (which are tracked in the simulator) very easily. If instead we used the energy versus wave-vector relation (which is traditional) and then attempted to find v_x from the velocity versus wave-vector relation, it would have been immensely complicated. The reason is that the velocity (or energy) versus wavevector relation is *spin-dependent* in the presence of Rashba effect [99] and becomes even more complicated if the Rashba effect is strong which leads to spin-mixing effects [100]. These complications would have been overwhelming in our case since we have a continuous distribution of spins and hence would have been faced with a denumerably infinite number of energy versus wavevector relations. The way to avoid this daunting complication and the associated numerical cost is to use the energy-velocity relation, which is spin-independent, instead of energy-wavevector relation which is spin-dependent.

In the simulation, carriers are injected into a quasi-1D GaAs channel of rectangular cross-section ($30 \text{ nm} \times 4 \text{ nm}$) as described in Figure 2.1. We have assumed that there is a transverse electric field of 100 kV/cm (in the y direction) that gives rise to structural

inversion asymmetry and induces a Rashba effect in the channel. This field perturbs the subband energies in the channel but only slightly. The transverse voltage drop over a 4 nm wide channel due to this field is 40 meV, while the lowest subband energy is 355 meV. Therefore the perturbation is 11% for the lowest subband and progressively decreases for higher subbands. Consequently, we neglect this perturbation. Electrons are injected from a Fermi-Dirac distribution with their spins all aligned along the channel axis (x axis) in order to simulate the spin polarizer. At any given position x , we find the spin vector \bar{S}_x and compute the quantity $|T(\bar{S}_x)|^2$ for every electron. We also find the velocity v_x for every electron at position x and then compute the spin polarized current I_S by performing the ensemble averaging as described earlier. We have calculated I_S versus position x for channel electric fields in the range 1 – 10 kV/cm at two different temperatures of 30 K and 77 K.

3.3 Results and discussion

In Figure 3.1 we show the spatial decay of the normalized spin polarized current I_S for the four different (x directed) channel electric fields at a temperature of 30 K. In figure 3.2, we show the same quantity (along with the spatial decay of the ensemble averaged spin component \bar{S}_x) at an electric field of 2 kV/cm at temperatures of 30 K and 77 K. Spin depolarization is complete when the normalized spin current I_S reaches a value of 0.5. At this point an electron is equally likely to have its spin aligned parallel or antiparallel to the drain's magnetization (and therefore it is equally likely to be transmitted or blocked).

We can define a “spin relaxation length” as the distance over which the injected spin polarized current decays to 50% of its initial value (i.e., becomes completely depolarized).

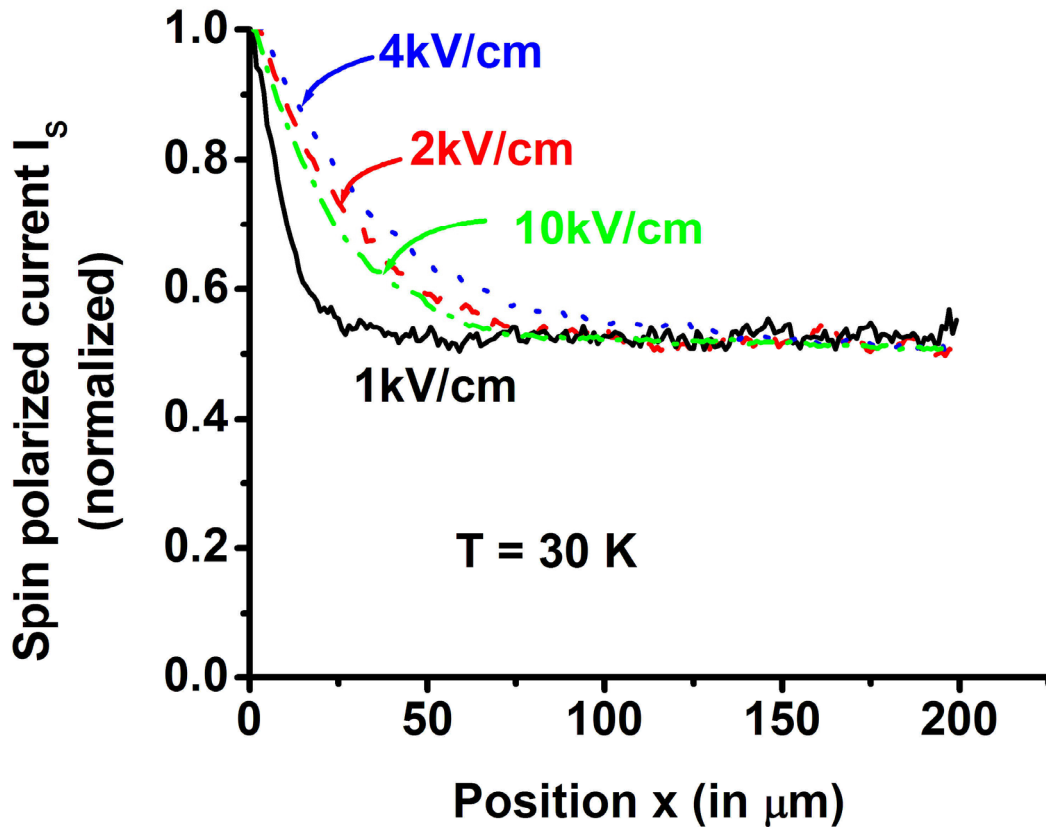


Figure 3.1 Spatial decay of the normalized spin polarized current in a GaAs quantum wire channel of rectangular cross section $30 \text{ nm} \times 4 \text{ nm}$. The results are shown for four different channel electric fields (1, 2, 4 and 10 kV/cm) at lattice temperature of 30K.

It is clear from Figure 3.2 that the spin relaxation length decreases with increasing carrier temperature because of increased scattering that causes increased spin depolarization. The electric field, on the other hand, has two opposing effects. The scattering rate increases slowly with the electric field, but so does the ensemble averaged electron drift velocity

until the saturation velocity is reached. A larger drift velocity makes the electrons travel a greater distance before getting depolarized. Consequently, the relaxation length at first increases with increasing electric field, but once the drift velocity begins to saturate, the

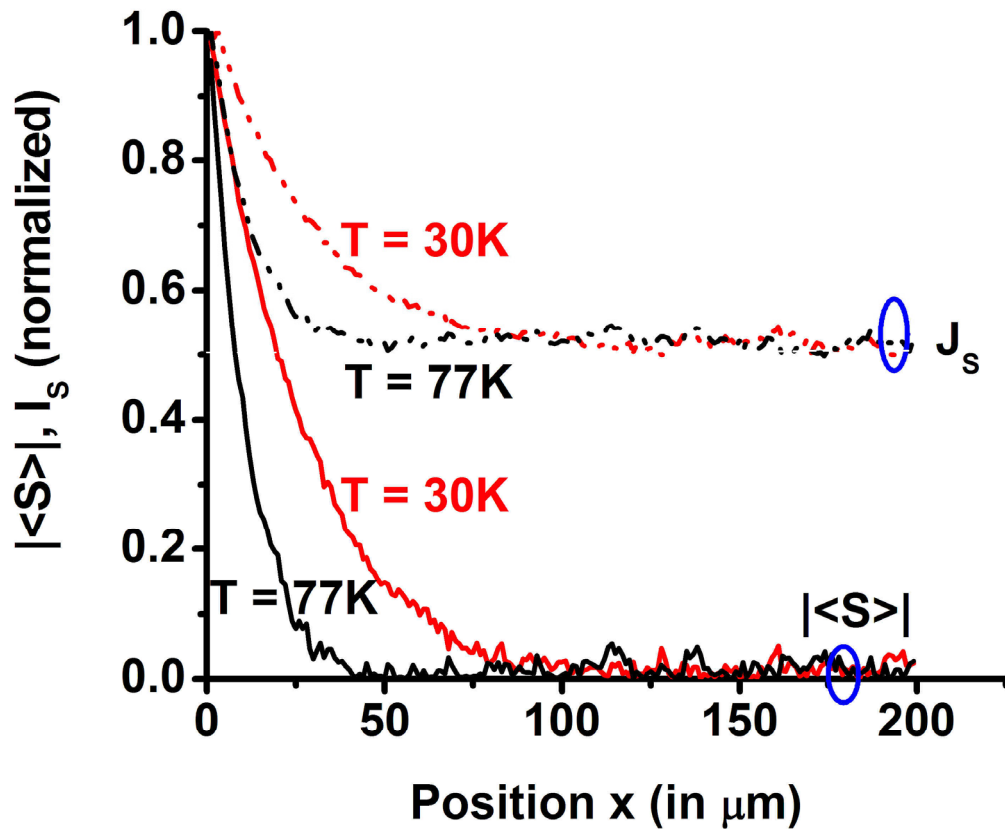


Figure 3.2 Spatial decay of the normalized spin polarized current and the injected spin vector in the GaAs quantum wire channel. The results are shown for two different temperatures of 30 K and 77 K at a fixed channel electric field of 2 kV/cm.

increased scattering takes over and the relaxation length starts to decrease with increasing electric field. The dependence of relaxation length on the electric field is therefore nonmonotonic. This non-monotonicity is shown in Figure 3.3. Based on the data presented

in this plot, we find that the relaxation length for spin polarized current is very large (between 20 and 100 μm for the cases considered). This is at least an order of magnitude larger than what was calculated for two-dimensional structures at comparable temperatures and driving electric fields [95, 96].

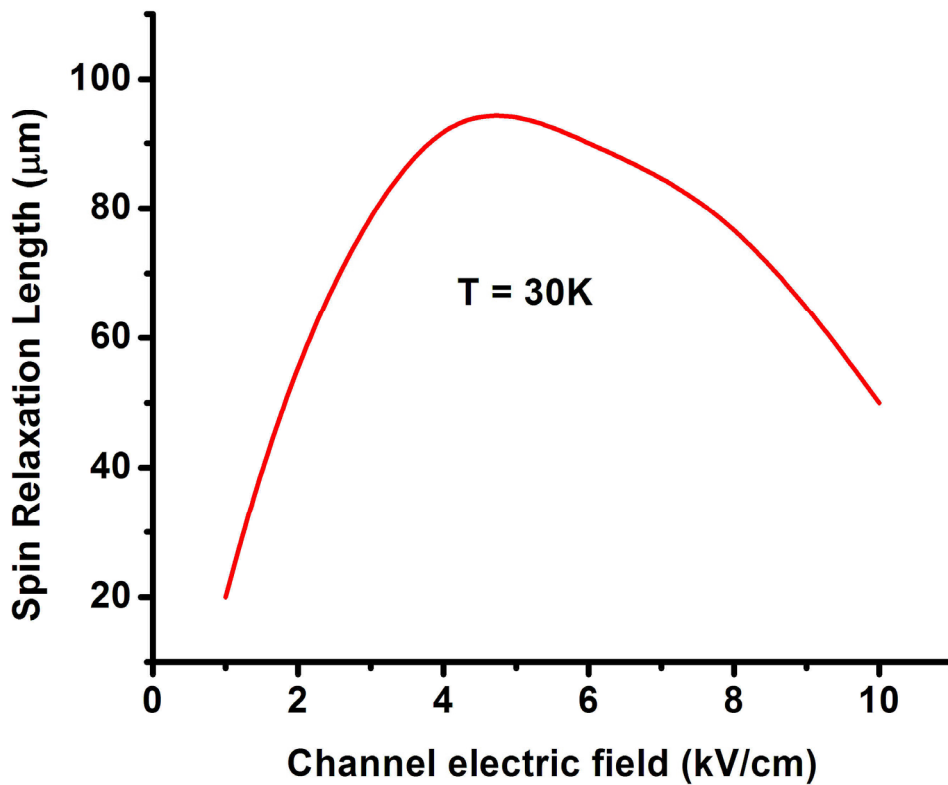


Figure 3.3 Dependence of spin relaxation length on transport-driving electric field

This difference is not due to any suppression of scattering. Even though elastic scattering is suppressed in quasi-1D structures [36], inelastic scattering is not [101], and the calculated mobility in 1D structure in this temperature range is less than that in bulk [86]. The true origin of the difference lies in the fact that Dresselhaus and Rashba interactions cause an

electron's spin to precess slowly (during free flight) about a so called "spin precession vector" that is independent of electron's velocity but depends only on subband indices and gate electric field. Intrasubband scattering cannot change the direction of this precession vector. Only when an electron undergoes an intersubband transition, this vector changes its direction. This leads to slow spin relaxation. In contrast, intrasubband scattering can change the direction of the spin precession vector in two- or three-dimensional structures. Therefore spin depolarizes at a faster rate in multi-dimensional structures.

Before concluding this chapter, we should mention that in a spin-valve type of structure, there is always a magnetic field in the channel, caused by the ferromagnetic contacts. This field, however weak, ensures that the eigenstates in the channel are not spin eigenstates [102, 103]. Therefore, even non-magnetic scatterers can cause spin relaxation [37]. This mechanism has not been considered here, since we have not considered the channel magnetic field.

Thus we have shown that spin relaxation length of electrons is very large in quasi-1D systems, even at elevated temperatures and high electric fields. Large spin relaxation lengths have been observed before in multidimensional structures, but only at low driving electric fields and low temperatures [104-106]. One-dimensional confinement can extend the range to high electric fields and elevated temperatures, which are required for realistic device applications.

CHAPTER 4. D'yakonov-Perel' Spin Relaxation of "Upstream" Electrons in a Quantum Wire: Failure of the Traditional "Drift-Diffusion" Model¹

Overview

The classical drift-diffusion model of spin transport treats spin relaxation via an empirical parameter known as the *spin diffusion length*. According to this model, the ensemble averaged spin of electrons drifting and diffusing in a solid decays exponentially with distance due to spin dephasing interactions. The characteristic length scale associated with this (spatial) decay is the spin diffusion length. The drift-diffusion model also predicts that this length is different for "upstream" electrons traveling in a decelerating electric field than for "downstream" electrons traveling in an accelerating electric field. However, this picture ignores energy quantization in confined systems (e.g. quantum wires) and therefore fails to capture the nontrivial influence of subband structure on spin relaxation. In this chapter we highlight this influence by simulating upstream spin transport in a multisubband quantum wire, in the presence of D'yakonov-Perel' spin relaxation, using a semiclassical model that accounts for the subband structure rigorously. We find that the

¹ This chapter has been published as [107] S. Pramanik, S. Bandyopadhyay, and M. Cahay, "Spin relaxation of "upstream" electrons in quantum wires: Failure of the drift diffusion model," *Physical Review B*, vol. 73, pp. 125309-1--125309-7, 2006.

upstream spin transport has a complex dynamics that defies the simplistic definition of a “spin diffusion length”. In fact spin does not decay exponentially or even monotonically with distance, and the drift-diffusion picture fails to explain the qualitative behavior, let alone predict the quantitative features accurately. Unrelated to spin transport, we also find that upstream electrons undergo a “population inversion” as a consequence of the energy dependence of the density of states in a quasi-one-dimensional structure.

4.1 Drift-diffusion model of spin transport

The central result of the drift diffusion model is a differential equation that describes the spatial and temporal evolution of carriers with a certain spin polarization n_σ . Reference [38] derived this equation for a number of special cases starting from the Wigner distribution function. In a coordinate system where the x axis coincides with the direction of electric field driving transport, this equation is of the form

$$\frac{\partial n_\sigma}{\partial t} - \mathbf{D} \frac{\partial^2 n_\sigma}{\partial x^2} - \mathbf{A} \frac{\partial n_\sigma}{\partial x} + \mathbf{B} n_\sigma = 0 \quad (4.1)$$

where

$$\mathbf{D} = \begin{bmatrix} D & 0 & 0 \\ 0 & D & 0 \\ 0 & 0 & D \end{bmatrix} \quad (4.2)$$

D is the diffusion coefficient, and \mathbf{A} and \mathbf{B} are dyadics (nine component tensors) that depend on D , the mobility μ , and the spin-orbit interaction strength in the material. Solution of equation (4.1), with appropriate boundary conditions, predict that the ensemble

averaged spin $|\langle \vec{S}(x) \rangle| = \sqrt{\langle S_x(x) \rangle^2 + \langle S_y(x) \rangle^2 + \langle S_z(x) \rangle^2}$ should decay exponentially with x according to

$$|\langle \vec{S}(x) \rangle| = |\langle \vec{S}(0) \rangle| \exp\left(-\frac{x}{L}\right) \quad (4.3)$$

where

$$\frac{1}{L} = \frac{\mu E}{2D} + \sqrt{\left(\frac{\mu E}{2D}\right)^2 + C^2} \quad (4.4)$$

Here E is the strength of the driving electric field and C is a parameter related to the spin-orbit interaction strength.

The quantity L is the characteristic length over which $|\langle \vec{S}(x) \rangle|$ decays to $\frac{1}{e}$ times its original value. Therefore it is defined as the ‘‘spin diffusion length’’. Equation (4.4) clearly shows that spin diffusion length depends on the sign of the electric field E . It is smaller for upstream transport (when E is positive) than for downstream transport (when E is negative).

This difference assumes importance in the context of spin injection from a metallic ferromagnet into a semiconducting paramagnet. Reference [40] pointed out that spin injection efficiency across the interface between these materials depends on the difference between the quantities L_s/σ_s and L_m/σ_m , where L_s is the spin diffusion length in the semiconductor, σ_s is the conductivity of the semiconductor, σ_m is the conductivity of the metallic ferromagnet, and L_m is the spin diffusion length in the metallic ferromagnet. Generally $\sigma_m \gg \sigma_s$. However, at sufficiently high retarding field, $L_s \ll L_m$, so that

$L_s / \sigma_s \approx L_m / \sigma_m$. When this equality is established, the spin injection efficiency is maximized. Thus reference [40] claimed that it is possible to circumvent the infamous “conductivity mismatch” problem [108], which inhibits efficient spin injection across a metal-semiconductor interface, by applying a high retarding electric field in the semiconductor close to the interface. A tunnel barrier between the ferromagnet and the semiconductor [109], or a Schottky barrier [110, 111] at the interface does essentially this and therefore improves spin injection.

The result of reference [40] depends on the validity of the drift diffusion model and equation (4.3) which predicts an exponential decay of spin polarization in space. Without the exponential decay, one cannot even define a “spin diffusion length” L . The question then is whether one expects to see the exponential decay under all circumstances, particularly in quantum confined structures such as quantum wires. The answer to this question is in the negative. Equation (4.1) and similar equations derived within the drift diffusion model, do not account for energy quantization in quantum confined systems and neglect the influence of subband structure on spin depolarization. This is a serious shortcoming, since in a semiconductor quantum wire, the spin-orbit interaction strength is different in different subbands. It is this difference that results in D’yakonov-Perel’ spin relaxation in quantum wires. Without this difference, the D’yakonov-Perel’ relaxation will be completely absent in quantum wires and the corresponding spin diffusion length will be always infinite [71]. The subband structure is therefore vital to spin relaxation. In the next section we will briefly repeat the semiclassical model which we used in earlier chapters.

4.2 Semiclassical model of spin relaxation

We have studied spin relaxation using a microscopic semiclassical model that is derived from the Liouville equation for the spin density matrix [112]. This model has been described in detail in previous chapters and will not be repeated here. Instead, for sole purpose of easy reference we will only highlight its essential features. This model allows us to study D'yakonov-Perel' spin relaxation taking into account the detailed subband structure in the system being studied.

In technologically important semiconductors, such as GaAs, spin relaxation is dominated by the D'yakonov-Perel' mechanism [32, 33]. This mechanism arises from Dresselhaus [26] and Rashba [27, 28] spin-orbit interactions that act as velocity dependent effective magnetic fields $\vec{B}(\mathbf{v})$. An electron's spin polarization vector \vec{S} precesses about $\vec{B}(\mathbf{v})$ according to the equation

$$\frac{d\vec{S}}{dt} = \vec{\Omega}(\mathbf{v}) \times \vec{S} \quad (4.5)$$

where $\vec{\Omega}(\mathbf{v})$ is the angular frequency of spin precession and is related to $\vec{B}(\mathbf{v})$ as $\vec{\Omega}(\mathbf{v}) = (e/m^*) \vec{B}(\mathbf{v})$, where m^* is the electron's effective mass. If the direction of $\vec{B}(\mathbf{v})$ changes randomly due to electron scattering which changes \vec{v} , then ensemble averaging over the spins of a large number of electrons will lead to a decay of the ensemble averaged spin in space and time. This is the physics of D'yakonov-Perel' spin relaxation in bulk and quantum wells. In a quantum wire, the direction of \vec{v} never changes in spite of scattering, it is always along the axis of the quantum wire ($\pm \hat{x}$). The direction of the magnetic field

$\vec{B}(\nu)$ is always fixed as long as an electron does not suffer intersubband scattering. Nevertheless, there can be D'yakonov-Perel' relaxation in a multisubband quantum wire, as we explain in the next paragraphs.

We will consider a quantum wire of rectangular cross section (as before) with its axis along the [100] crystallographic orientation, which we label the x axis. A symmetry breaking electric field E_y is present along \hat{y} to induce Rashba interaction (see Figure 2.1, for example). Then the components of the vector $\vec{\Omega}(\nu_x)$ due to the Dresselhaus and Rashba interactions are given by

$$\vec{\Omega}_D(\nu_x) = \frac{2m^* a_{42}}{\hbar^2} \left[\left(\frac{n\pi}{W_y} \right)^2 - \left(\frac{m\pi}{W_z} \right)^2 \right] \nu_x \hat{x} \quad (4.6 \text{ a})$$

$$\vec{\Omega}_R(\nu_x) = \frac{2m^* a_{46}}{\hbar^2} E_y \nu_x \hat{z} \quad (4.6 \text{ b})$$

where a_{42} and a_{46} are material constants, m and n are the transverse subband indices, ν_x is the electronic wavevector along the axis of the quantum wire, and W_y, W_z are the transverse dimensions of the quantum wire along y and z respectively. Therefore

$$\begin{aligned} \vec{B}(\nu_x) &= \frac{m^*}{e} \left[\vec{\Omega}_D(\nu_x) + \vec{\Omega}_R(\nu_x) \right] \\ &= \frac{2m^{*2} a_{42}}{e\hbar^2} \left[\left(\frac{n\pi}{W_y} \right)^2 - \left(\frac{m\pi}{W_z} \right)^2 \right] \nu_x \hat{x} + \frac{2m^{*2} a_{46}}{e\hbar^2} E_y \nu_x \hat{z} \end{aligned} \quad (4.7)$$

Thus $\vec{B}(\nu_x)$ lies in the $x-z$ plane and subtends an angle θ with the wire axis (\hat{x}) given by

$$\theta = \arctan \left[\frac{a_{46} E_y}{a_{42} \left\{ \left(\frac{n\pi}{W_y} \right)^2 - \left(\frac{m\pi}{W_z} \right)^2 \right\}} \right] \quad (4.8)$$

Note from the above equation that in any given subband in a quantum wire, the direction of $\vec{B}(v_x)$ is fixed, irrespective of the magnitude of the velocity v_x since θ is independent of v_x . Only the precession frequency $\vec{\Omega}$ depends on v_x . In case of bulk or 2D, both θ and $\vec{\Omega}$ depend on electron velocity even if the electron resides in the same subband. This is the reason why D'yakonov-Perel' process is suppressed in a quantum wire.

However, θ is different in different subbands because the Dresselhaus interaction is different in different subbands. Consequently, as electrons transition between subbands because of intersubband scattering, the angle θ , and therefore the direction of the effective magnetic field $\vec{B}(v)$ changes. This causes D'yakonov-Perel' spin relaxation in a multisubband quantum wire. Since spins precess about different axes in different subbands, ensemble averaging over electrons in all subbands results in a gradual decay of net spin polarization. Thus there is no D'yakonov-Perel' spin relaxation in a quantum wire if a single subband is occupied, but it is present if multiple subbands are occupied and intersubband scattering occurs. This was discussed thoroughly in Chapters 2 and 3 of this dissertation [71].

The subband structure is therefore critical to D'yakonov-Perel' spin relaxation in a quantum wire. In fact, if a situation arises whereby all electrons transition to a single

subband and remain there, further spin relaxation due to D'yakonov-Perel' process will cease thereafter. In this case, spin no longer decays, let alone decay exponentially with distance. Hence spin relaxation cannot be parameterized by a constant spin diffusion length.

The rest of this chapter is organized as follows. In the next section, we describe our model system, followed by results and discussions in section 4.4. Finally we conclude in section 4.5.

4.3 Model of upstream spin transport

We consider a non-centrosymmetric (e.g. GaAs) quantum wire with axis along [100] crystallographic direction. We choose a three-dimensional Cartesian coordinate system with \hat{x} coinciding with the axis of the quantum wire (Figure 4.1). The structure is of length $L_x = 1.005 \mu m$ with rectangular cross section $W_y = 4 nm$, $W_z = 30 nm$. A metal gate is placed on the top (not shown in Figure 4.1) to induce symmetry breaking electric field $E_y \hat{y}$, which causes the Rashba interaction. In a quantum wire defined by split Schottky gates on a two dimensional electron gas, $E_y \hat{y}$ arises naturally because of the triangular potential confining carriers near the heterointerface. We assume $E_y = 100$ kV/cm [46]. In addition, there is another electric field $-E_x \hat{x}$ ($E_x > 0$) which drives transport along the axis of the quantum wire. Consider the case when spin polarized monochromatic electrons are constantly injected into the channel at $x = x_0 = 1 \mu m$ with injection velocities along $-\hat{x}$. If these electrons occupy only the lowest subband at all

times, then there will be no D'yakonov-Perel' spin relaxation [71]. Therefore in order to study multisubband effect on spin dephasing of upstream electrons, we inject them with

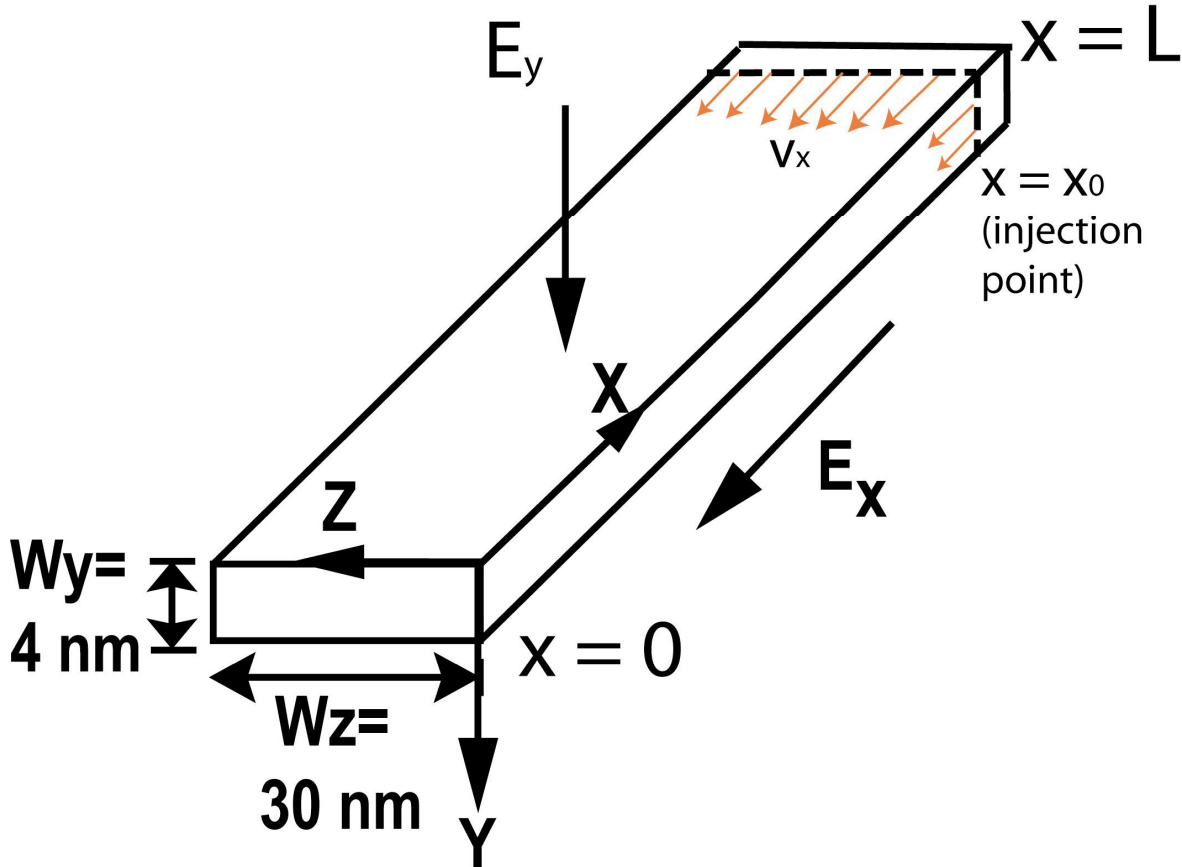


Figure 4.1. A quantum wire structure of length $L = 1.005 \mu m$ with rectangular cross section $30 \text{ nm} \times 4 \text{ nm}$. A top gate (not shown) applies a symmetry breaking electric field E_y to induce the Rashba interaction. A battery (not shown) applies an electric field $-E_x \hat{x}$, $E_x > 0$, along the channel. Monochromatic spin polarized electrons are injected at $x = x_0 = 1 \mu m$ with injection velocity $-v_{inj}$. These electrons travel along $-\hat{x}$ (upstream electrons) until their directions of motion are reversed due to the electric field $-E_x \hat{x}$. We investigate spin dephasing of these upstream electrons.

enough energy E_0 that they initially occupy multiple subbands. We ignore any thermal broadening of injection energy [38] since $E_0 \gg k_B T$ for the range of temperatures (T) considered, k_B being Boltzmann's constant. Let E_i denote the energy at the bottom of i th subband ($i = 1, 2, \dots, n, n+1, \dots$, etc.). We place E_0 between the n th and $(n+1)$ th subband bottoms as shown in Figure 4.2.

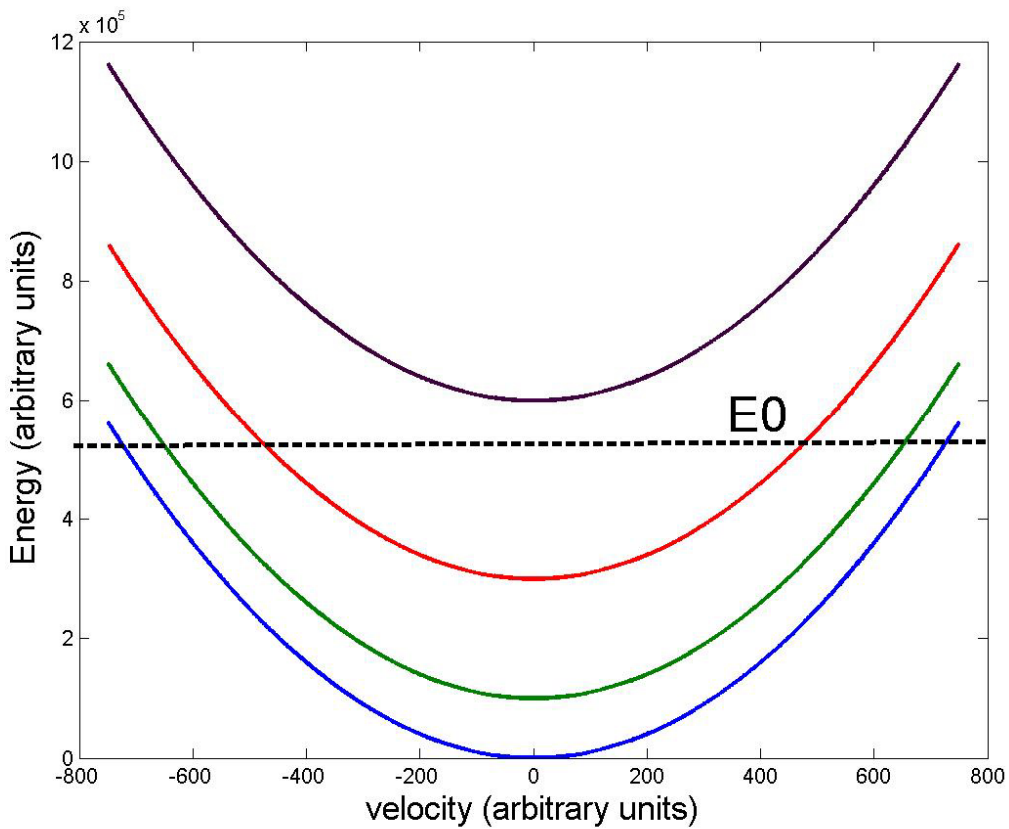


Figure 4.2 Subband energy dispersion in the quantum wire

In other words, $E_n < E_0 < E_{n+1}$. We assume that the injected electrons each with energy E_0 , are uniformly distributed over the lowest n subbands. In other words, at time $t = 0$,

electron population of the i th ($1 \leq i \leq n$) subband is given by $N_i(x, t=0) = (N_0/n) \delta(x-x_0) \delta(E-E_0)$, where N_0 is the total number of injected electrons and E denotes their energies. At any subsequent time t , these distributions spread out in space ($x < x_0$), as well as in energy, due to interaction of the injected electrons with the electric field E_x and numerous scattering events. Relative population of electrons among different subbands will change as well due to intersubband scattering events. Upstream electrons originally injected into, say, subband i with velocity $-v_i \hat{x}$ ($v_i > 0$), gradually slow down because of scattering and the decelerating electric field. They change their direction of motion (i.e. become downstream) beyond a distance $|\bar{x}_i - x_0|$ measured from the injection point x_0 . Thus, no upstream electrons will be found in the i th subband beyond \bar{x}_i . Note that the value of $|\bar{x}_i - x_0|$ depends on three factors: the initial injection velocity in subband i , the decelerating electric field and the scattering history. On the other hand, the “classical turning distance” of monochromatic electrons injected into the i th subband with energy E_0 for a given electric field E_x is given by

$$E_0 - E_i = \frac{1}{2} m^* v_i^2 = e E_x |x_i - x_0| \quad (4.9)$$

where E_i is the energy at the bottom of the i th subband and v_i is the injection velocity in the i th subband. Note that x_i does not depend on scattering history and $x_i = \bar{x}_i$ in ballistic transport. Clearly $v_n < v_{n-1} < \dots < v_2 < v_1$ for a given E_0 (see Figure 4.2). Thus for a given channel electric field E_x , $x_n - x_0 = \min\{x_i - x_0\}$, $i = 1, 2, \dots, n$. Hence we concentrate only

on the region $\{x_n, x_0\}$ where almost all electrons are upstream electrons. In the simulation, the velocity of every electron is tracked and as soon as an electron alters direction and goes downstream (i.e. its velocity becomes positive) it is ignored by the simulator and another upstream electron is simultaneously injected from $x = x_0$ randomly in any of the n lowest subbands with equal probability. This process is continued for a sufficiently long time until electron distributions over different subbands, $N_i(x, t)$, $i = 1, 2, \dots, n$, no longer change with time. Under this condition we say that the steady state is achieved for the upstream electrons. These steady state electron distributions are extended from $x = x_n$ to $x = x_0$ and heavily skewed near the region $x = x_0$. This steady state distribution of upstream electrons does not represent the local equilibrium electron distribution because of two reasons (a) upstream electrons are constantly injected into the channel at $x = x_0$; this is the reason why the distributions are skewed near $x = x_0$, and (b) we exclude any downstream electrons from the distribution. At local equilibrium, there will be of course both upstream and downstream electrons in the distribution.

The model described above allows us to separate upstream electrons from downstream electrons and therefore permits us to study upstream electrons in isolation. Of course, in a real quantum wire, both upstream and downstream electrons will be present at any time, even in the presence of a strong electric field, since there will always be some nonvanishing contribution of backscattered electrons to the upstream population.

The semiclassical model and the simulator used to simulate spin transport have been described in reference [46]. Based on that model, at steady state, the magnitude of the ensemble averaged spin vector at any position x inside the channel is given by

$$\left| \langle \vec{S}(x) \rangle \right| = \frac{\sqrt{\left(\sum_{i=1}^n N_i(x) \langle S_{ix}(x) \rangle \right)^2 + \left(\sum_{i=1}^n N_i(x) \langle S_{iy}(x) \rangle \right)^2 + \left(\sum_{i=1}^n N_i(x) \langle S_{iz}(x) \rangle \right)^2}}{\sum_{i=1}^n N_i(x)} \quad (4.10)$$

Here $\langle S_{i\zeta}(x) \rangle$, $\zeta = x, y, z$ denotes the ensemble average of ζ component of spin at position x . Subscript i implies that ensemble averaging is carried out over electrons only in the i th subband. The above equation can be simplified to

$$\left| \langle \vec{S}(x) \rangle \right| = \frac{\sqrt{\left(\sum_{i=1}^n N_i(x) \left| \langle S_i(x) \rangle \right| \right)^2 - 2 \sum_{i,j=1}^n N_i(x) N_j(x) \left| \langle S_i(x) \rangle \right| \left| \langle S_j(x) \rangle \right| \sin^2 \frac{\theta_{ij}}{2}}}{\sum_{i=1}^n N_i(x)} \quad (4.11)$$

where $\langle \vec{S}_i(x) \rangle = \langle S_{ix}(x) \rangle \hat{x} + \langle S_{iy}(x) \rangle \hat{y} + \langle S_{iz}(x) \rangle \hat{z}$ and $\theta_{ij}(x)$ is the angle between $\langle \vec{S}_i(x) \rangle$ and $\langle \vec{S}_j(x) \rangle$. Note that in absence of any intersubband scattering event, $\left| \langle \vec{S}_i(x) \rangle \right| = 1$ for all x (i.e. initial spin polarization of the injected electrons) [71].

Simulation results that we present here can be understood using equation (4.11).

4.4 Results and discussion

We examine how ensemble averaged spin polarization of upstream electrons $\left| \langle \vec{S}(x) \rangle \right|$ varies in space for different values of driving electric field E_x and injection energy E_0 for a

fixed lattice temperature T . We vary E_x in the range $0.5 - 2$ kV/cm for constant injection energy 426 meV and $T = 30$ K, where E_0 is measured from the bulk conduction band energy. The lowest subband bottom is 351 meV above the bulk conduction band edge. To study the influence of injection energy, we also present results corresponding to $E_0 = 441$ meV with $E_x = 1$ kV/cm and $T = 30$ K. In all cases mentioned above, injection energies lie between subband 3 and subband 4. Injected electrons are equally distributed among the three lowest subbands initially. Obviously, this corresponds to a non-equilibrium situation. All injected electrons are 100% spin polarized transverse to the wire axis (i.e. either \hat{y} or \hat{z}). Figures 4.3 – 4.8 show how ensemble averaged spin components $\langle S_x(x) \rangle, \langle S_y(x) \rangle, \langle S_z(x) \rangle$ and $|\langle \vec{S}(x) \rangle|$ of upstream electrons evolve over space. Figures 4.3 – 4.6 show the influence of the driving electric field on spin relaxation. Figure 4.7 shows the influence of initial injection energy, and Figure 4.8 shows the influence of initial spin polarization. It is evident that neither the driving electric field, nor the initial injection energy, nor the initial spin polarization has any significant effect on spin relaxation. Note that $|\langle \vec{S}(x) \rangle|$ does not decay exponentially with distance, contrary to equation (4.3). Spatial distribution of electrons over different subbands is shown in Figures 4.9 – 4.13. The classical turning point of each electron in the third subband (x_3) has been indicated in each case. Figures 4.9 – 4.12 show the influence of initial injection energy on the spatial evolution of subband population. As expected, $|x_0 - x_3|$ decreases with increasing electric field in accordance with equation (4.9). Note that at low electric field (Figures 4.9 and

4.10) $\bar{x}_3 \approx x_3$ since all subbands are getting nearly depopulated of “upstream” electrons at $x = x_3$. Recall that $\bar{x}_3 = x_3$ only if transport is ballistic; therefore we can conclude that upstream transport is nearly ballistic in the range $|x_0 - x_3|$ when $E_x < 1$ kV/cm. At high electric fields, when $E_x > 1.5$ kV/cm (Figure 4.12), $|\bar{x}_3 - x_0| > |x_3 - x_0|$. This indicates that there are many upstream electrons even beyond the classical turning point. It can only happen if there is significant scattering that drives electrons against the electric field,

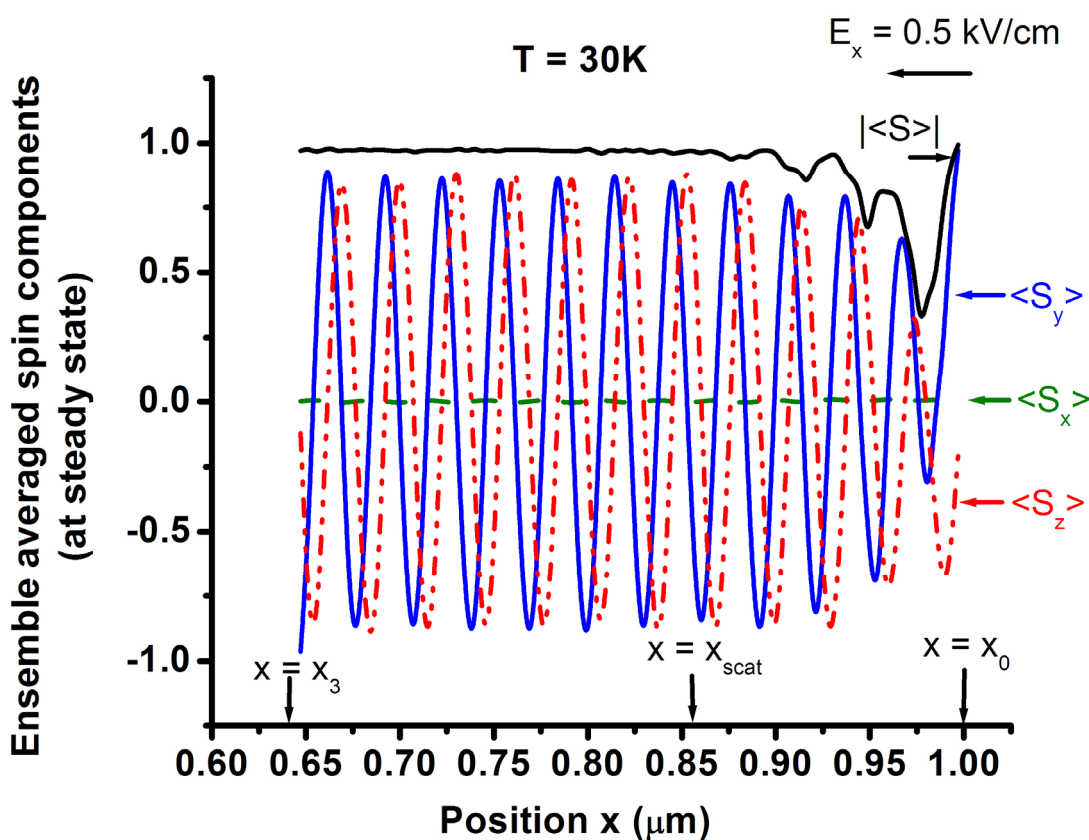


Figure 4.3. Spatial variation of ensemble averaged spin components for driving electric field 0.5 kV/cm at steady state. Lattice temperature is 30 K, injection energy is 426 meV. Electrons are injected with equal probability into the three lowest subbands. Classical turning point of subband 3 electrons is denoted by x_3 and x_{scat} indicates the point along the channel axis where subbands 1 and 2 get virtually depopulated. Injected electrons are y polarized and $x = x_0 = 1 \mu\text{m}$ is the point of injection.

making them go beyond the classical turning point. We can also deduce that most of these scattering events impart momentum to the carriers to aid upstream motion rather than oppose it since there are electrons beyond the classical turning point. This behavior is a consequence of the precise nature of the scattering events and would not have been accessible in drift-diffusion models that typically treat scattering via a relaxation time approximation.

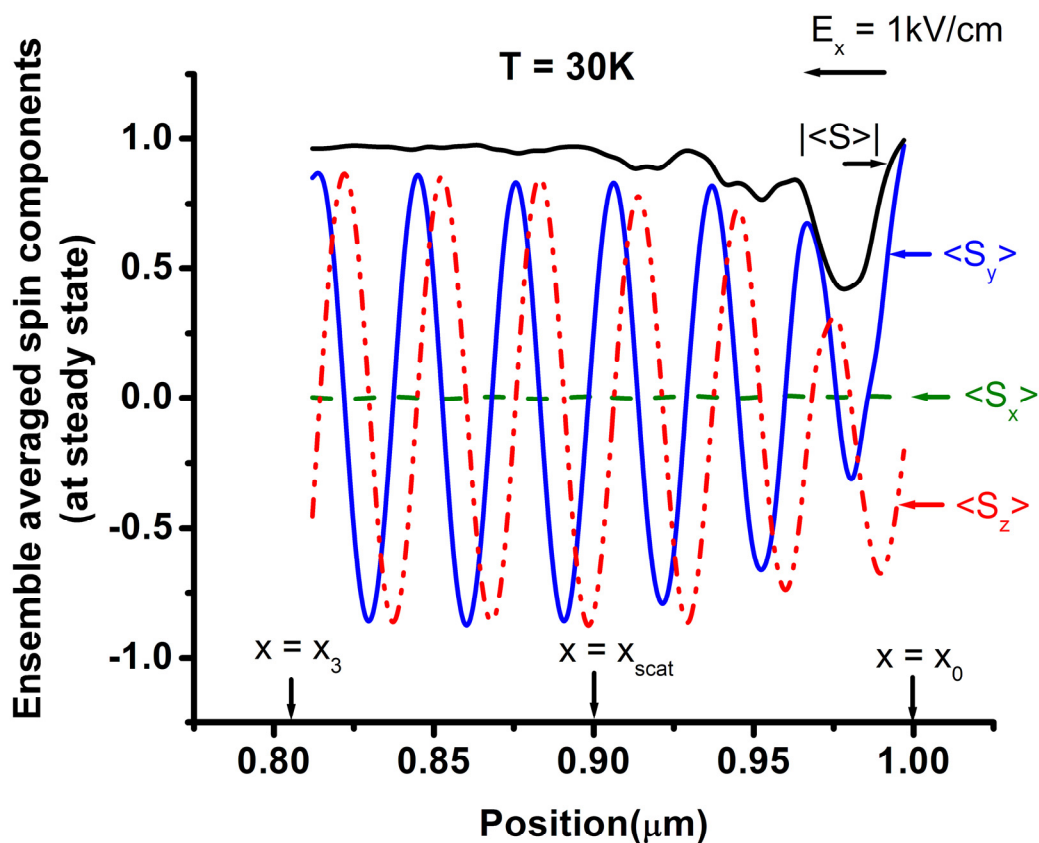


Figure 4.4. Spatial variation of ensemble averaged spin components for driving electric field 1 kV/cm at steady state. Other conditions are same as in Figure 4.3.

4.5 Population inversion of upstream electrons

Note that even though electrons are injected equally in all three subbands, most electrons end up in subband 3 – the highest occupied subband initially – soon after injection. Beyond a certain distance ($x = x_{scat} \approx 0.9 \mu m$) subbands 1 and 2 become virtually depopulated. This feature is very counterintuitive and represents a population inversion of upstream electrons. It can be understood as follows: scattering rate of an electron with energy E is

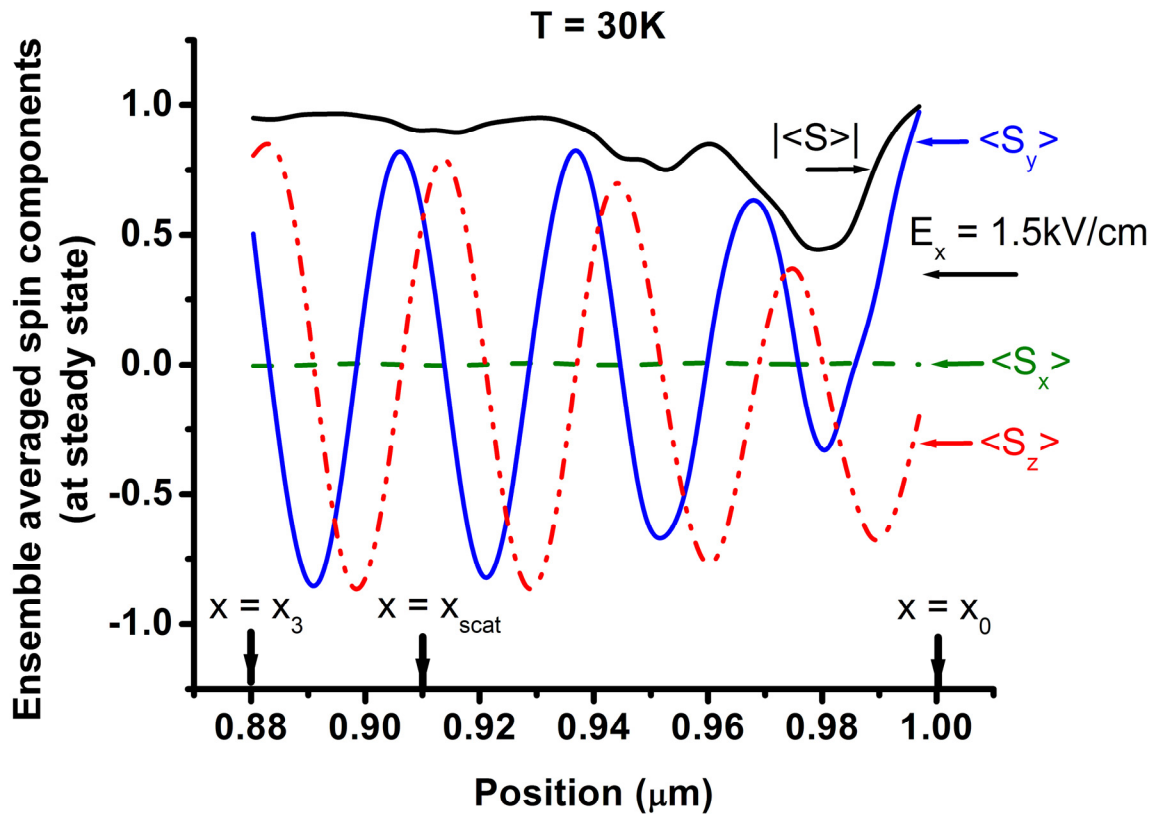


Figure 4.5. Spatial variation of ensemble averaged spin components for driving electric field 1.5 kV/cm at steady state. Other conditions are same as in Figure 4.3.

proportional to the density of the final state. In a quantum wire, density of states has $1/\sqrt{E - E_i}$ dependence where E_i is the energy at the bottom of the i th subband. As the injected electrons move upstream they gradually cool down and their energies approach the energy at the bottom of the subband 3 (E_3). To visualize this, imagine the horizontal dashed line E_0 in Figure 4.2 sliding down with passage of time. As the bottom of subband 3 is approached, electrons will increasingly scatter into subband 3 since the density of final

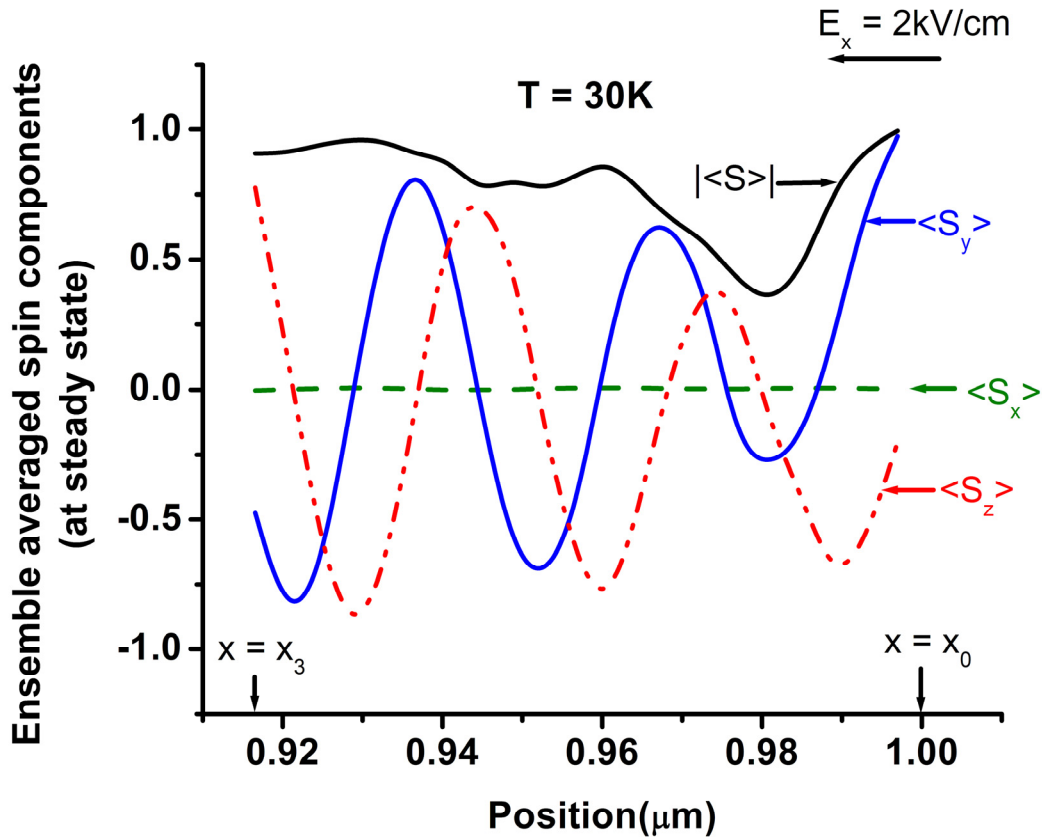


Figure 4.6. Spatial variation of ensemble averaged spin components for driving electric field 2 kV/cm at steady state. Other conditions are same as in Figure 4.3.

state in subband 3 is increasing rapidly. To scatter into a final state in subband 2 or 1 that has the same density of states as in subband 3 will require a much larger change in energy and hence a much more energetic phonon which is rare since the phonons obey Bose-Einstein statistics. Therefore subband 3 is the overwhelmingly preferred destination and this preference increases rapidly as electrons cool further. Consequently, beyond a certain

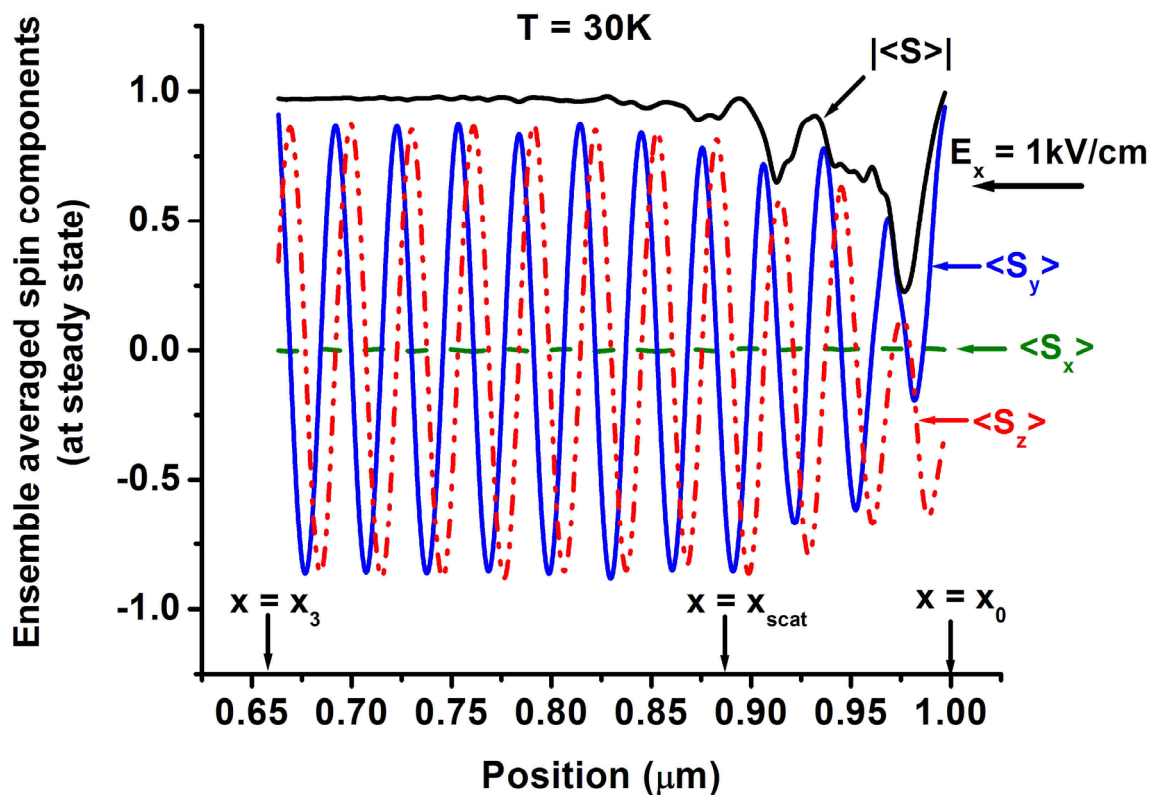


Figure 4.7. Spatial variation of ensemble averaged spin components at steady state. Driving electric field is 1 kV/cm, lattice temperature = 30 K and injection energy is 441 meV. Injected electrons are y polarized.

distance, virtually all electrons are scattered to subband 3 leaving subbands 1 and 2 depleted. This feature is a peculiarity of quasi-one-dimensional system and will *not* be

observed in bulk or quantum wells. Exact values of x_3 and x_{scat} depend on injection energy and electric field. In the field range 0.5 – 1.5 kV/cm and injection energy 426 meV, $|x_3| > |x_{\text{scat}}|$. However, for higher values of electric field (e.g. 2 kV/cm) or, smaller values of injection energies, electrons reach classical turning point before subbands 1 and 2 get depopulated.

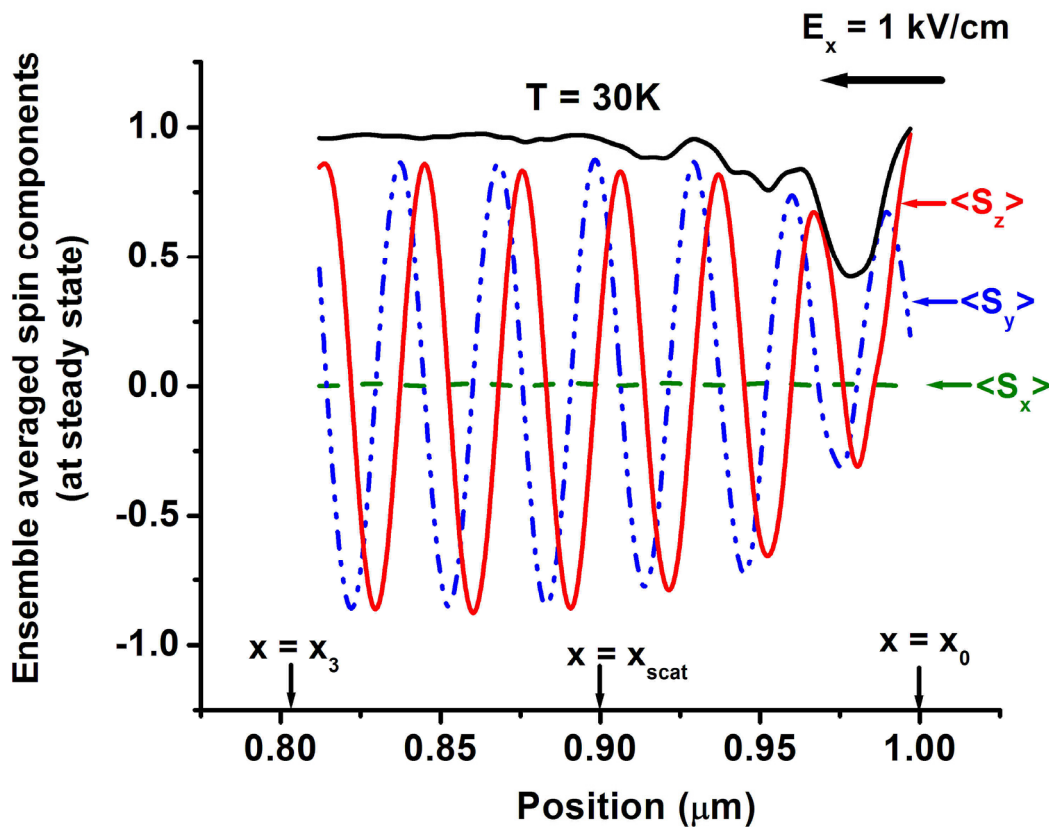


Figure 4.8. Spatial variation of ensemble averaged spin components at steady state. Driving electric field is 1 kV/cm, lattice temperature = 30 K and injection energy is 426 meV. Injected electrons are z polarized.

Spin dephasing in the region (x_{scat}, x_0) is governed by equation (4.11). We observe a few subdued oscillations in $|\langle \mathbf{S} \rangle|(x)$ in this region because of the “sine term” in equation

(4.11). However, in the region (x_3, x_{scat}) , subbands 1 and 2 are almost depopulated. Therefore, there is no D'yakonov-Perel' relaxation in the interval (x_3, x_{scat}) since only a single subband is occupied [71]. Consequently, the ensemble averaged spin assumes a constant value $|\langle S_3 \rangle| < 1$ and does not change any more. Thus in this region, one can say

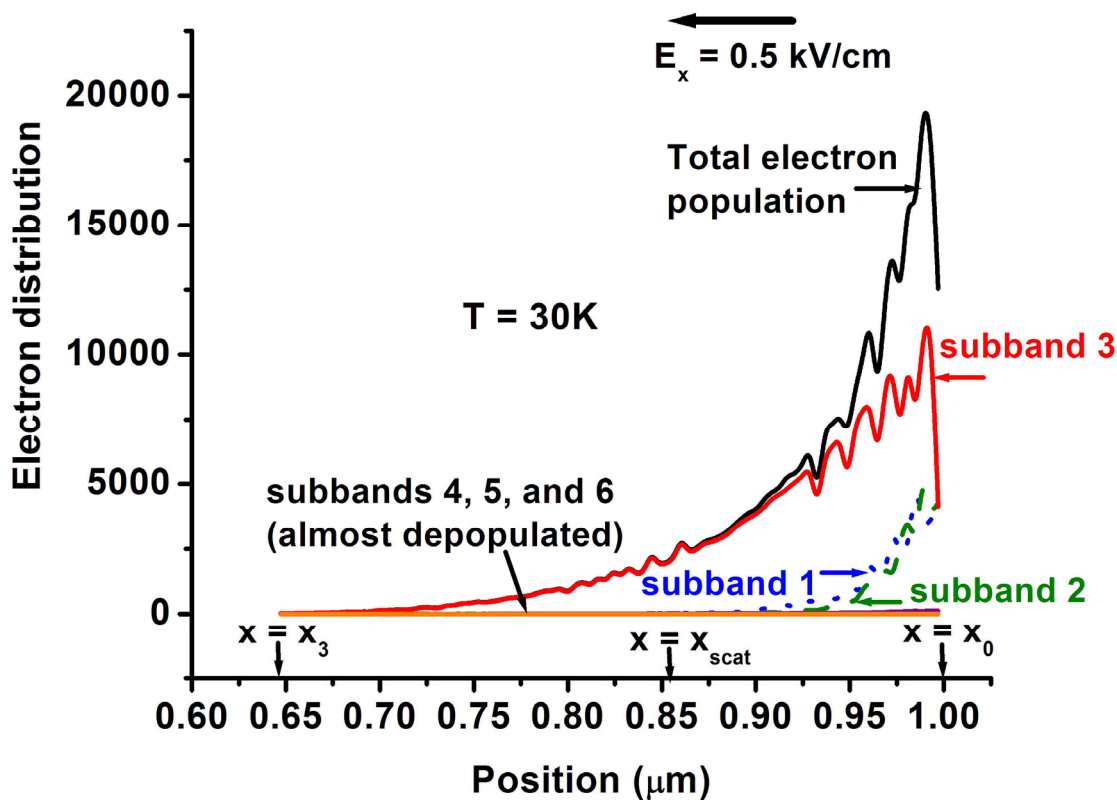


Figure 4.9. Spatial variation of electron population over different subbands at steady state. Driving electric field is 0.5 kV/cm, lattice temperature = 30 K and injection energy is 426 meV. Injected electrons are y polarized.

that spin dephasing length becomes infinite. It should be noted that it is meaningless to study spin dephasing in the region $x < x_3$ because electrons do not even reach this region.

4.6 Conclusion

In this chapter, we have used a semiclassical model to study spin dephasing of upstream electrons in a quantum wire, taking into account the subband formation. We showed that the subband structure gives rise to rich features in the spin dephasing characteristics of the

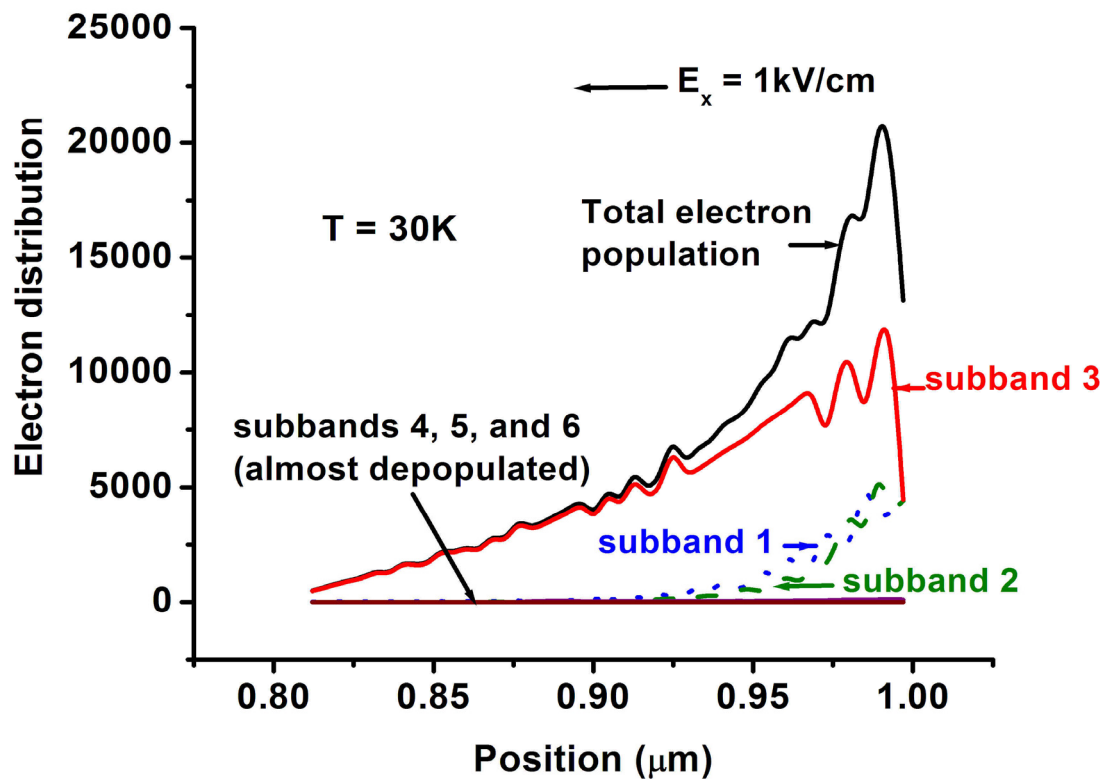


Figure 4.10. Spatial variation of electron population over different subbands at steady state. Driving electric field is 1 kV/cm, lattice temperature = 30 K and injection energy is 426 meV. Injected electrons are y polarized.

upstream electrons that cannot be captured in models which fail to account for the precise physics of spin dephasing and the fact that it is different in different subbands. Because spin relaxation in a multisubband quantum wire is non-exponential (even non-monotonic)

in space, it does not make sense to invoke a “spin diffusion length”, let alone use such a heuristic parameter to model spin dephasing. Finally, we have found a population inversion effect for upstream electrons. It is possible that downstream electrons also experience a similar population inversion. This scenario is currently being investigated.

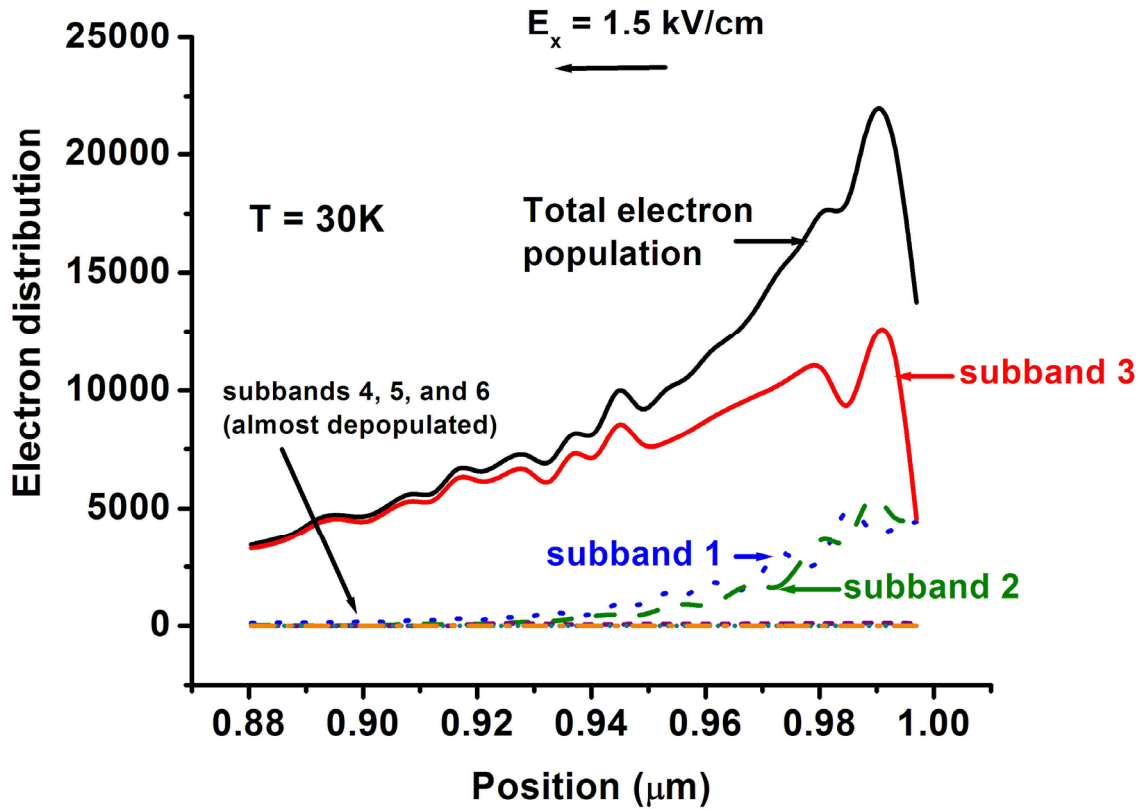


Figure 4.11. Spatial variation of electron population over different subbands at steady state. Driving electric field is 1.5 kV/cm, lattice temperature = 30 K and injection energy is 426 meV. Injected electrons are y polarized.

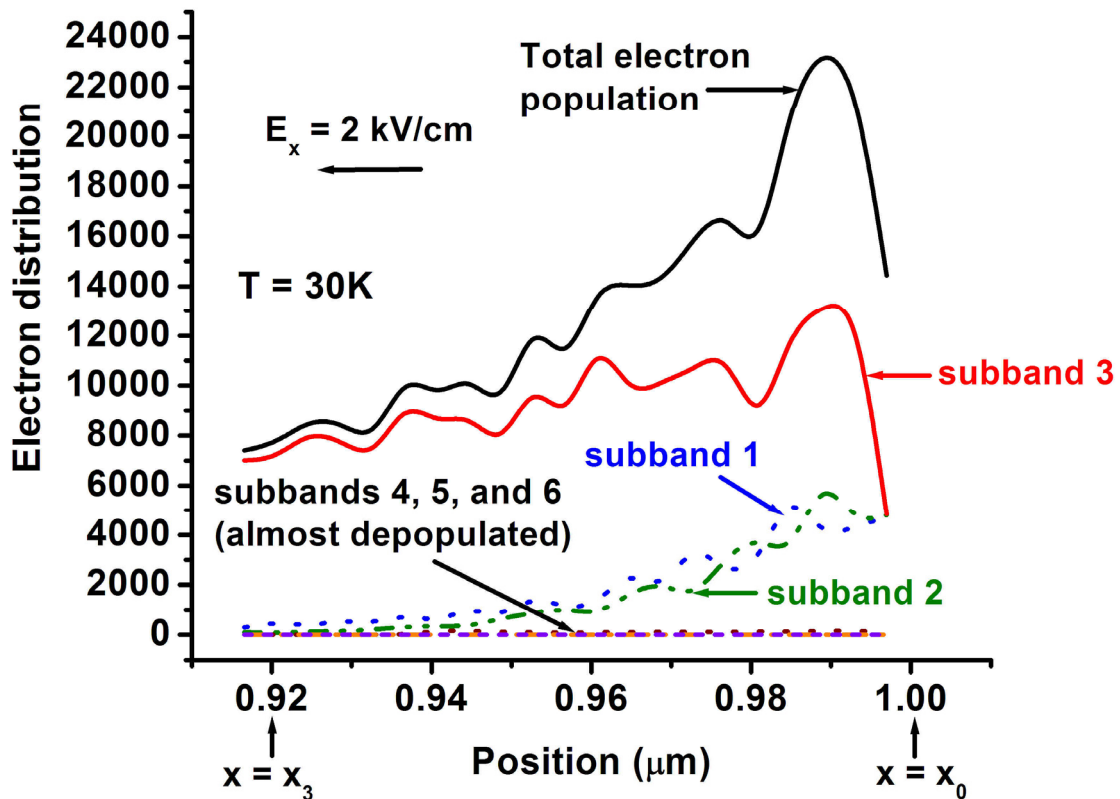


Figure 4.12. Spatial variation of electron population over different subbands at steady state. Driving electric field is 2 kV/cm, lattice temperature = 30 K and injection energy is 426 meV. Injected electrons are y polarized.

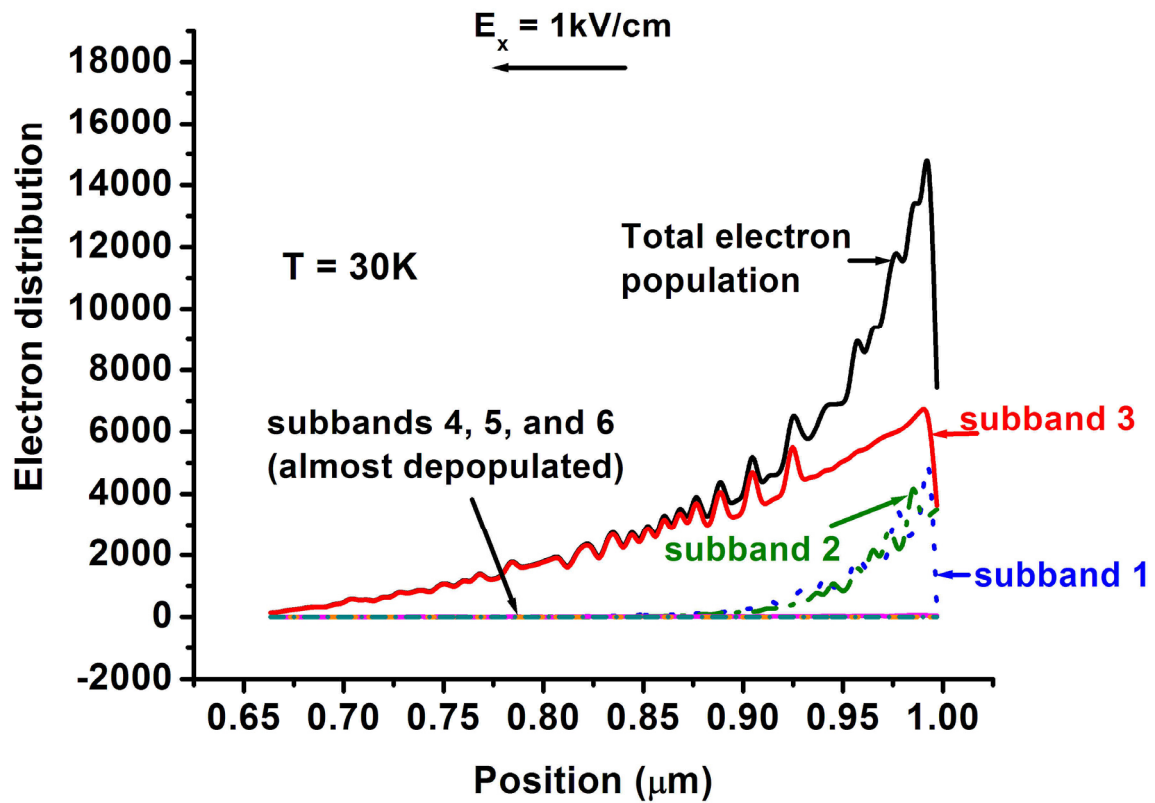


Figure 4.13. Spatial variation of electron population over different subbands at steady state. Driving electric field is 1 kV/cm, lattice temperature = 30 K and injection energy is 441 meV. Injected electrons are y polarized.

CHAPTER 5. Spin Fluctuations and “Spin Noise”

Overview

We have theoretically studied the temporal fluctuations and the resulting kinetic noise in the average spin polarization of an electron ensemble drifting and diffusing in a quantum wire under a high electric field. Electrons are initially injected in the wire from a ferromagnetic contact with all their spins polarized along the wire axis. The average spin polarization of the ensemble decays during transport because of D'yakonov-Perel' relaxation caused by both Rashba and Dresselhaus interactions. Once steady state is reached, the average spin fluctuates randomly around zero. The time average of this fluctuation is zero. The autocorrelation function of this fluctuation approximates a Lorentzian and so does the spectral density. To our knowledge, this is the first study of spin fluctuations and “spin noise” in a nanostructure.

5.1 Introduction

Semi-classical non-linear model of spin transport couples spin density matrix evolution (based on a fully quantum mechanical Sturm-Liouville type equation) with the semi-classical Boltzmann transport equation. From our discussions in the previous chapters, we

observed that this approach can account for non-linear transport effects, as well as interference effects between orthogonal spin states. So far, this model has revealed surprising features of spin transport in semiconductor quantum wires. For instance, it has been shown that spin relaxation rate can be very anisotropic (spin injected along the wire is much longer lived than spin injected transverse to the wire axis) [46] and the relaxation rate can be suppressed by at least an order of magnitude by quasi one-dimensional quantum confinement (see Chapter 3, for example). This model is ideal for studying spin relaxation due to D'yakonov-Perel' mechanism. It is also capable of producing information about spin fluctuations since they are microscopic and deal with a *spin distribution function* unlike the drift diffusion models that deal only with ensemble averaged “moments” of the distribution function. In this chapter, we have used such a model to study temporal spin fluctuations of a steady state electron ensemble drifting and diffusing in a quantum wire under a high electric field when hot carrier effects (non-local and non-linear effects) are important. To our knowledge, this is the first study of spin fluctuation and noise in a nanostructure. We present results pertaining to the autocorrelation function of the fluctuations as well as the spectral density of the associated kinetic “spin noise”.

5.2 Theoretical model

We consider a “spin-valve” type quantum wire structure consisting of a GaAs quantum wire capped by half-metallic ferromagnetic contacts with 100% spin polarization. The wire has a rectangular cross section of $30 \text{ nm} \times 4 \text{ nm}$. The confining potential in the wire is slightly asymmetric which gives rise to a uniform electric field of 100 kV/cm transverse to

the wire axis (y -axis, see Figure 2.1). An electric field $E_x \hat{x}$ is applied along the axis of the wire (\hat{x} axis) to drive transport. As the electrons traverse the wire, they experience velocity dependent spin-orbit coupling interactions due to the Rashba effect (structural inversion asymmetry) and the Dresselhaus effect (bulk inversion asymmetry). As a result, the spin vector of each electron precesses around an effective magnetic field. This precession is randomized by inter-subband scattering between different subbands that have different Dresselhaus interaction strengths. As a result, the *ensemble averaged spin vector* decays with time resulting in D'yakonov-Perel' type relaxation. This mechanism has been discussed in details in last three chapters.

We have considered a case where $E_x = 2$ kV/cm and the lattice temperature $T = 30$ K. The details of the simulation approach (which is based on a Monte Carlo simulator modified to study spin transport) can be found in reference [46] and will not be repeated here. In the simulation, we consider only the D'yakonov-Perel' relaxation and ignore the Elliott-Yafet, Bir-Aronov-Pikus and all other relaxation mechanisms (including relaxation due to hyperfine interactions with the nuclei), since these are insignificant compared to the D'yakonov-Perel' relaxation in the present case.

5.3 Results and discussion

In Figure 5.1, we show that the ensemble average spin component along the wire axis $\langle S_x \rangle(t)$ decays to zero after 6 ns and thereafter continues to fluctuate around zero, signaling the onset of complete depolarization. We will study the nature of this spin fluctuation. We define spin autocorrelation function as follows:

$$C(\tau) = \int_{t_0}^{\infty} [\langle S_x \rangle(t) - \langle S_x \rangle_{av}] [\langle S_x \rangle(t + \tau) - \langle S_x \rangle_{av}] dt$$

(5.1)

where

$$\langle S_x \rangle_{av} = \int_{t_0}^{\infty} \langle S_x \rangle(t) dt \quad (5.2)$$

and the variable τ is generally referred to as “delay time”. We observe from Figure 5.1 that $\langle S_x \rangle(t)$ varies randomly around zero for $t \geq t_0$ where t_0 is the time taken to reach steady state. Hence, $\langle S_x \rangle_{av} = 0$. The noise spectral density is defined as the cosine transform of the autocorrelation function and is expressed as follows:

$$S(f) = \int_0^{\infty} [C(\tau) \cos(2\pi f \tau)] d\tau \quad (5.3)$$

Figure 5.2 shows the autocorrelation function of the spin fluctuations at a driving electric field of 2 kV/cm and the lattice temperature of 30 K. The autocorrelation function decays rapidly and becomes almost zero for $\tau = 0.375$ ns. Beyond this point it shows very small fluctuation around zero. The associated noise spectral density is shown in Figure 5.3. It decays rapidly within 10 GHz.

5.4 Conclusion

In this work we have studied, for the first time, “spin noise” in a semiconductor structure using a semi-classical approach. The autocorrelation function has no long-duration component indicating that once steady state is reached, there is no long-lived “memory” of

the initial spin state in the fluctuations. The D'yakonov-Perel' relaxation is therefore an efficient relaxation mechanism that completely erases any long-lived memory of the initial spin state.

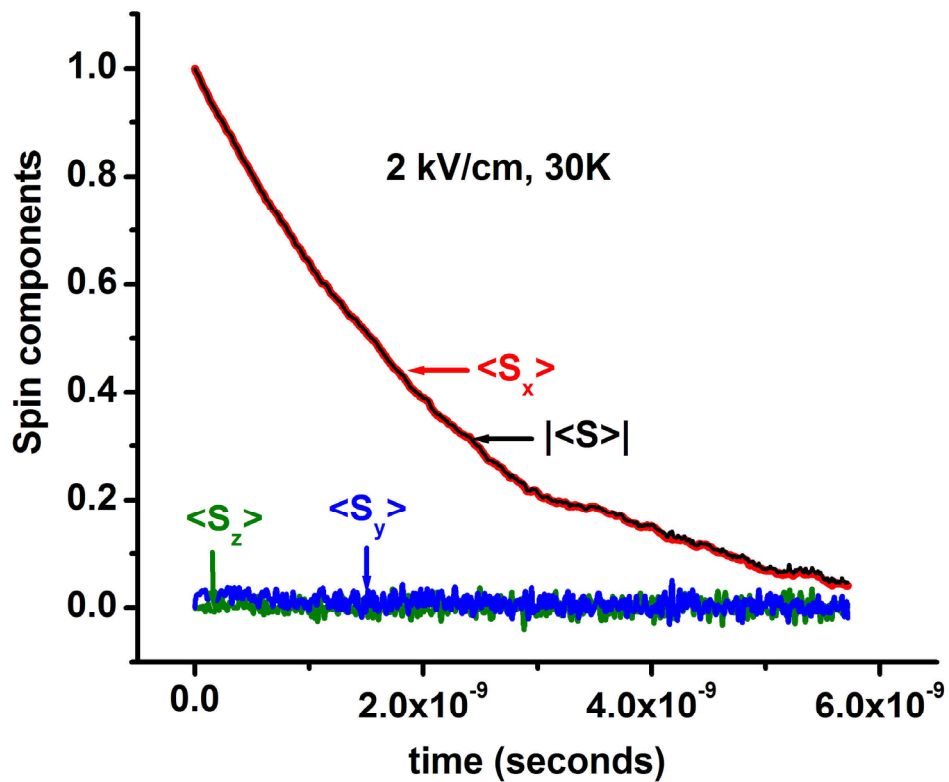


Figure 5.1. Temporal dephasing of the x , y and z components of ensemble average spin in the GaAs quantum wire at 30 K. The driving electric field is 2 kV/cm, and the spins are injected with their polarizations initially aligned along the wire axis (x -axis).

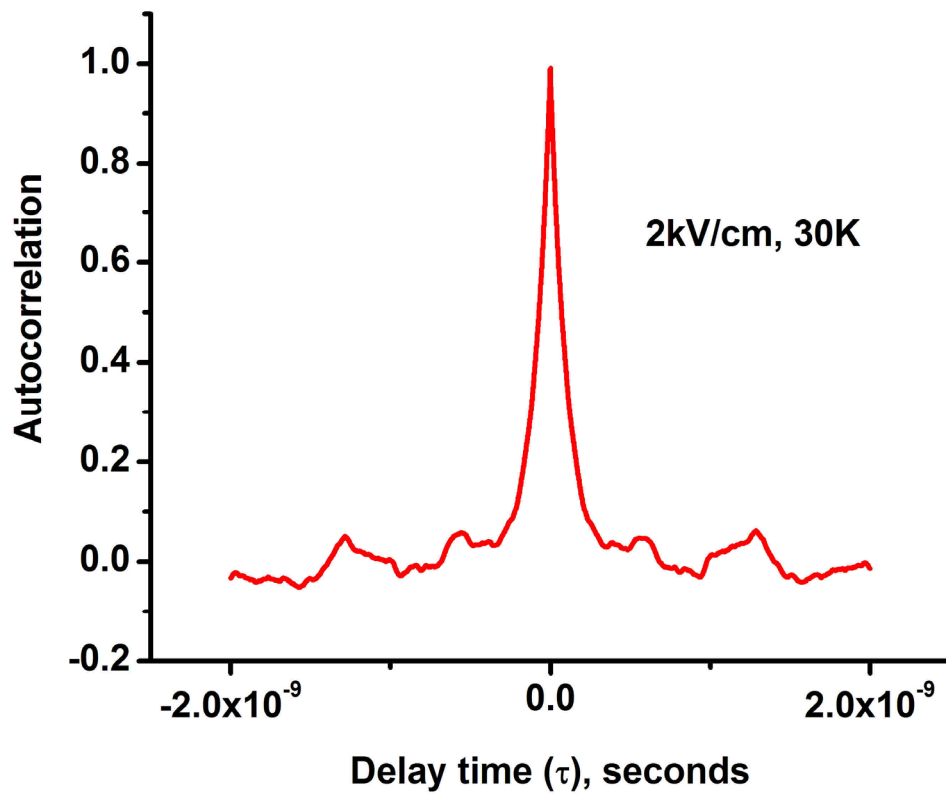


Figure 5.2. Autocorrelation function of the spin fluctuations in the GaAs quantum wire at a driving electric field of 2 kV/cm and at a lattice temperature of 30 K.

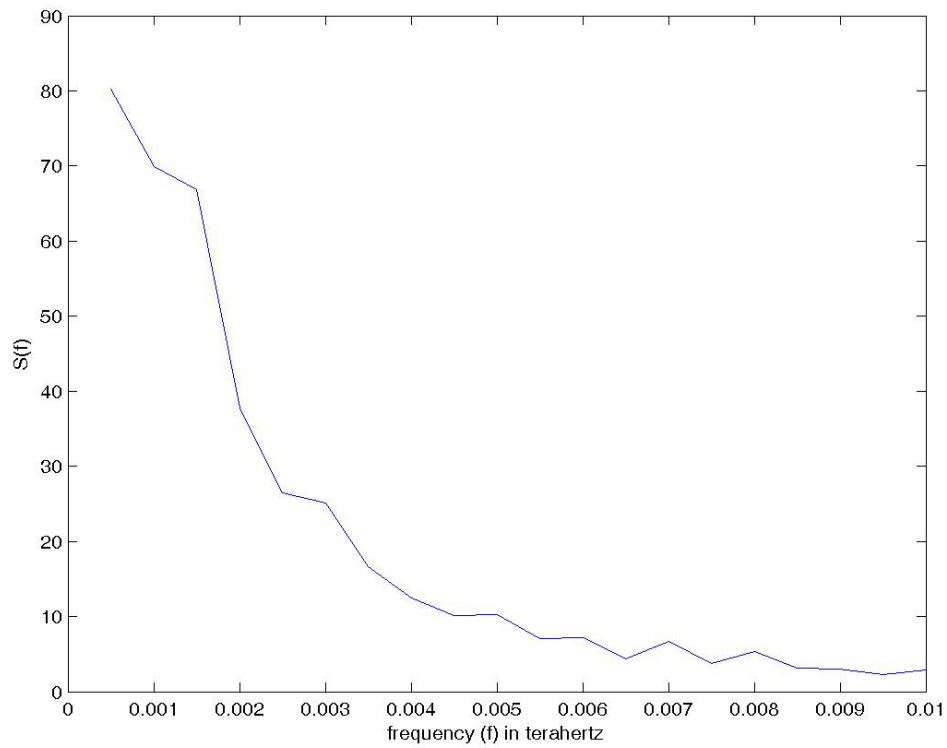


Figure 5.3. The spectral density of “spin-noise” in the quantum wire for driving electric field = 2 kV/cm and lattice temperature = 30 K.

CHAPTER 6. Spin Transport Experiment in Self-Assembled All-Metal Nanowire Spin Valves: A Study of the Pure Elliott-Yafet Mechanism*

Overview

In this chapter we report an experimental study of spin transport in all metal nanowire spin valve structures. The nanowires have a diameter of 50 nm and consist of three layers – cobalt, copper and nickel. Based on the experimental observations, we determine that the primary spin relaxation mechanism in the paramagnet layer – copper – is the Elliott-Yafet mode associated with elastic scattering caused by charged states on the surface of the nanowires. This mode is overwhelmingly dominant over all other modes, so that we are able to study the pure Elliott-Yafet mechanism in isolation. We deduce that the spin diffusion length associated with this mechanism is about 16 nm in our nanowires and is fairly temperature independent in the range 1.9 K – 100 K, which is consistent with the spin relaxation being associated with elastic scattering by surface states. The corresponding spin relaxation time is about 100 femtoseconds. We also find that the spin relaxation rate is fairly independent of the electric field driving the current in the field range 0.3 – 3 kV/cm.

* This chapter has been published as [113] S. Pramanik, C-G. Stefanita, and S. Bandyopadhyay, "Spin transport in self assembled all-metal nanowire spin valves: A study of the pure Elliott-Yafet mechanism," *Journal of Nanoscience and Nanotechnology*, vol. 6, pp. 1973-1978, 2006.

6.1. Introduction

All-metal spin valve devices with Cu as the spacer material have been studied in various configurations [114-116] by several groups in the past. However, the dominant spin relaxation mechanism in the Cu spacer was never conclusively identified. There exist four possible mechanisms that can cause spin relaxation in Cu. These are (1) the D'yakonov-Perel' (DP) mechanism [32, 33], (2) the Elliott-Yafet (EY) mechanism [30, 31], (3) the Bir-Aronov-Pikus (BAP) mechanism [34] and (4) hyperfine interaction (HFI) between nuclear and carrier (electron/hole) spins [35]. The most likely candidates for spin relaxation in Cu are the DP and EY processes because the BAP mechanism is absent for unipolar transport and the HFI mechanism is much weaker compared to the DP and the EY in most solids, including Cu.

The DP mechanism comes about because of spin orbit coupling in Cu which gives rise to a momentum-dependent effective magnetic field. The carrier spin precesses about this effective field, and the precession rate is different for different carriers since they all have different momenta owing to scattering. As a result, the spins of different carriers are randomized and the average spin of an ensemble of carriers decays with time (as well as distance). This decay is the DP relaxation.

In the presence of spin-orbit interaction, the Bloch states in a crystal are not spin eigenstates. Consequently, even a non-magnetic scatterer can couple two Bloch states that have slightly non-orthogonal spins. The resulting scattering event will cause spin rotation and thus contribute to both momentum and spin relaxation. This is the EY mechanism.

Neither the DP nor the EY relaxation rate has been individually measured in Cu since it is not normally possible to separate the two. However, there is a way to make one rate much higher than the other. We measure the spin relaxation length in a *nanowire* spin valve consisting of Co-Cu-Ni as shown in Figure 6.1.

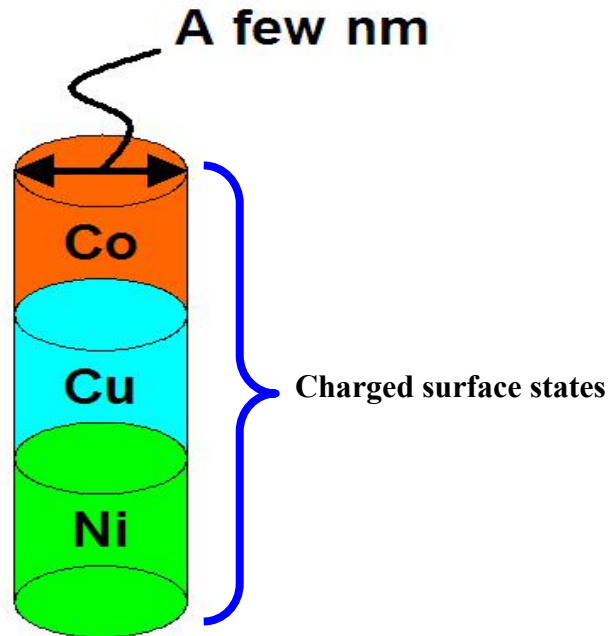


Figure 6.1 Schematic description of a nanowire spin valve structure consisting of Co, Cu and Ni.

In this type of nanowire, electrons will experience increased elastic scattering (Coulomb scattering) due to a very high concentration of charged surface states (approximately $10^{13}/\text{cm}^2$) [117], which will decrease carrier mobility. Now the DP mechanism is suppressed by frequent elastic scattering [32], while the Elliott-Yafet mechanism is enhanced [30]. Thus, confining carriers in a nanowire will make the EY rate overwhelmingly dominant over the DP rate and thus allow us to measure the relaxation

rate due to the EY mechanism alone. This, then, will permit us to probe various features of the EY mechanism in a metal, such as the temperature and electric field dependence of the EY relaxation rate.

6.2 Experimental results

In order to fabricate a nanowire spin valve structure, we start with a high purity (99.997%) metallic aluminum foil (0.1 mm thick), which is electropolished in a suitable organic solution [118] to produce a mirror like surface. An anodic alumina film with highly ordered nanopores is formed on this electropolished surface by a multistep anodization procedure [119]. The anodization conditions (e.g. the nature of the acidic electrolyte, anodization voltage, duration of final step anodization etc.) determine the dimensions of the nanopores. In this work we have used 0.3 M oxalic acid as the electrolyte and anodization voltage has been kept constant at 40V dc. Under these conditions we get a porous alumina film with nominal pore diameter of 50 nm (Figure 6.2).

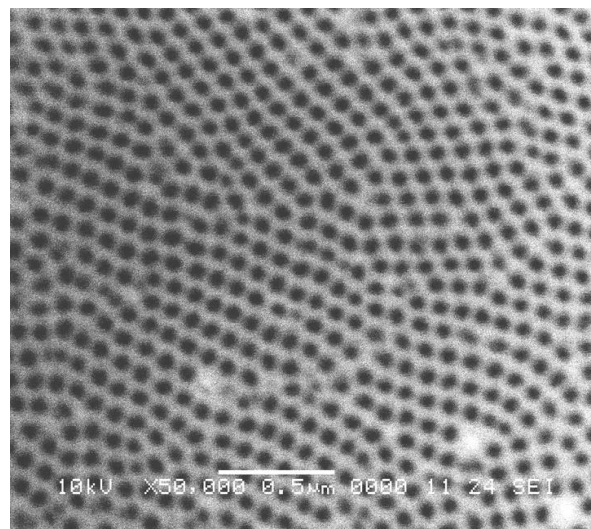


Figure 6.2 SEM micrograph of the top surface of the alumina template formed by anodization using 3% oxalic acid at 40V dc.

Final step anodization was carried out for 90 seconds which makes the pores ~ 100 nm deep. The insulating alumina barrier layer at the pore bottom is removed by a “reverse polarity etching” technique [120], which results in a “through hole” nanopattern on the bulk aluminum. Figure 6.3 shows an SEM micrograph of the porous film from the back side showing that the pores have opened up at the back creating a “through hole” structure. This “through hole” structure allows dc electrodeposition of materials selectively within the pores since it makes the conducting aluminum substrate electrically accessible at the pore bottom.

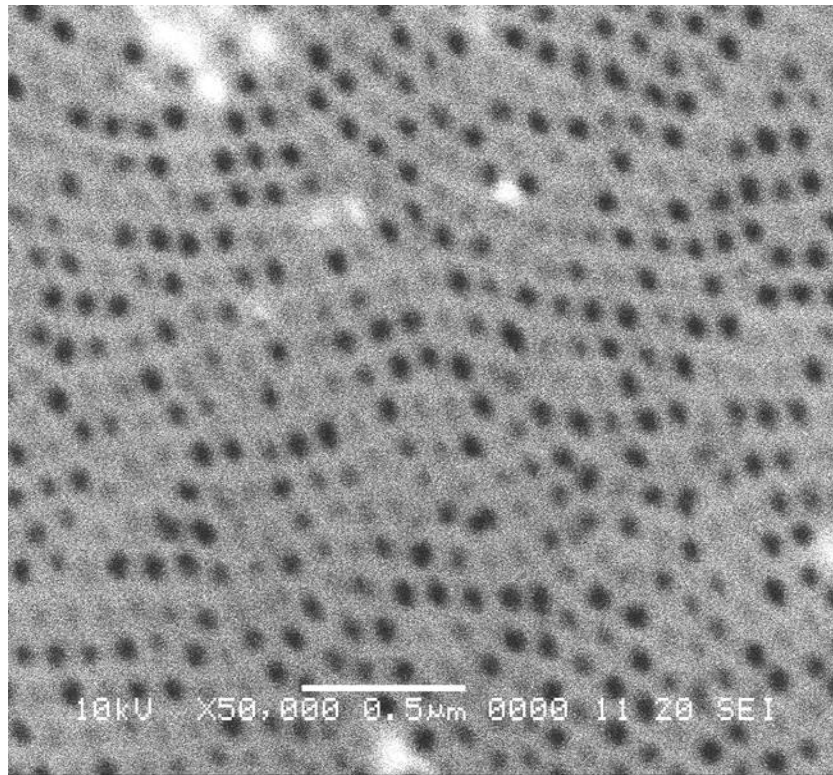


Figure 6.3 SEM micrograph of the bottom surface of the alumina template after removing the bulk aluminum. This shows that the reverse polarity etching technique has successfully removed the barrier layer.

A spin-valve configuration is a trilayered structure in which a nonmagnetic layer is sandwiched between two ferromagnetic electrodes. In this work, the nonmagnetic “spacer” layer is Cu and the ferromagnetic electrodes are Co and Ni. These tri-layered nanowires are produced by sequentially electrodepositing Ni, Cu and Co inside the pores. Electrodeposition has been carried out by applying a small dc bias of 1.5 V at a platinum counter electrode with respect to the aluminum foil. The electrolyte is a dilute aqueous solution of the metal-sulfate salt with slightly acidic pH. Small deposition current ($\sim \mu\text{A}$) ensures slow and well-controlled electrodeposition of metals inside the pores. We calibrated the deposition rate of each metal under these experimental conditions. To achieve this, we monitor the deposition current during electrodeposition of each metal inside an anodic alumina template of known pore length. The deposition current increases drastically when the pores are completely filled. The deposition rate is determined by calculating the ratio of pore length to pore filling time. According to this calibration, for the spin-valve structure, thicknesses of Ni and Cu layers are estimated to be approximately 40 nm each and the Co layer is approximately 20 nm thick. As a final verification step, we prepared a test sample where the ferromagnetic layers were intentionally made thick (in order to have a sufficiently long wire for characterization), while the Cu layer thickness was kept at 40 nm. These wires were then released from their alumina host by dissolution in hot chromic-phosphoric acid, washed, and captured on TEM grids for imaging. Figure 6.4 shows a TEM micrograph of a tri-layered nanowire. The Cu layer is indeed 40 nm thick which attests to the reliability of our calibration procedure.

After the electrodeposition step, we are left with a two dimensional array of trilayered nanowires vertically standing in an insulating alumina matrix. The alumina film is slightly etched from top side in dilute phosphoric acid in order to expose the tips of the nanowires for electrical contact from the top. This process exposes the tips of some, but not all, nanowires. At the bottom, the nanowires form an ohmic contact with the aluminum substrate.

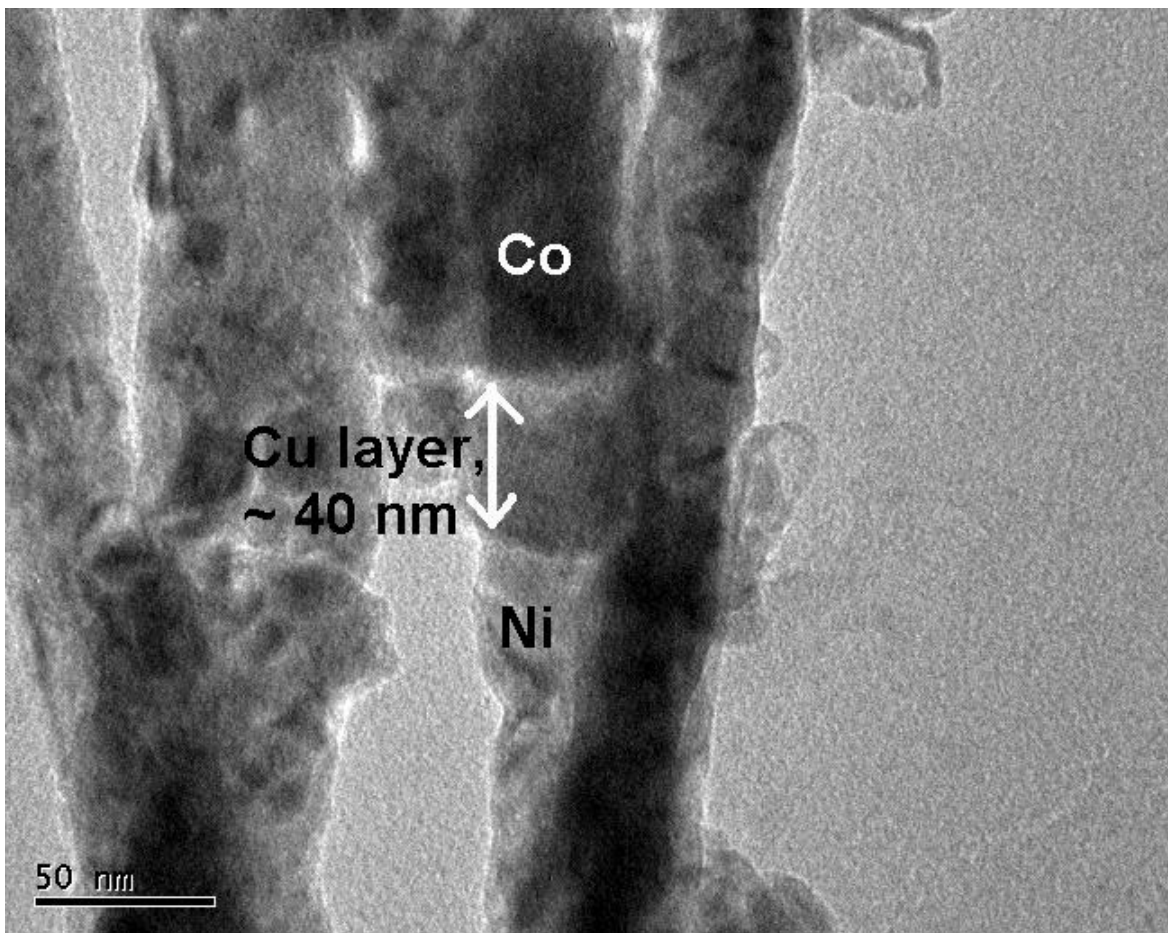


Figure 6.4 Transmission electron micrograph of released tri-layered nanowires showing that the Cu layer is ~ 40 nm thick.

Again not all nanowires are contacted from the bottom either, since not all pores open up at the bottom as seen in Figure 6.3. Overall, the fraction of nanowires that are electrically contacted from both top and bottom (and are therefore electrically probed) is rather small. This is a boon since it allows us to interrogate a small number of nanowires with relatively large contact pads. Contacts pads are made to the top (Co layer) and bottom (Al) using silver paste and gold wires are attached to the contact pads for electrical characterization. The contact areas are $\sim 1\text{mm} \times 1\text{mm}$. The schematic cross-section of the spin-valve structure is shown in Figure 6.5.

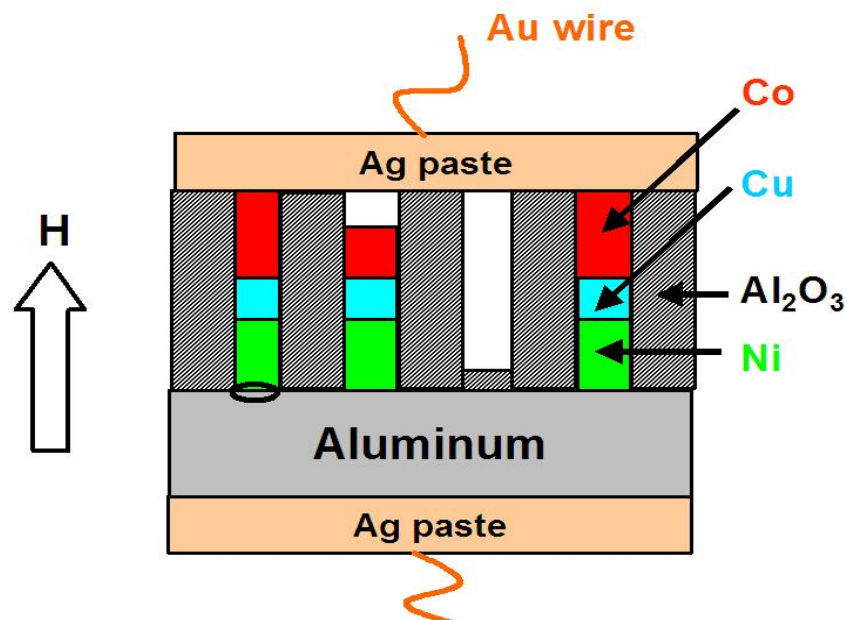


Figure 6.5 A schematic representation of the all-metal nanowire spin valve device. Note that not all nanowires are connected from both sides. Here only two wires are shown connected (electrically) from both ends.

Magneto-resistance of this device is measured in a Quantum Design Physical Property Measurement System. Sample temperature is varied in the range 1.9 – 300 K while magnetic field is swept from -70 kOe to $+70\text{ kOe}$. Applied bias current is $10\ \mu\text{A}$.

The device resistance is $\sim 300\Omega$ which is quite large for an all-metal device. Since the contact pad area is $1\text{ mm} \times 1\text{ mm}$, and the pore density is 10^{10} cm^{-2} , the pads must have covered 10^8 wires. Yet the resistance is this large. This can only be explained if a very small fraction of 10^8 wires are actually contacted from both ends. Later we will show that only about one in 10 million wires are electrically contacted from both ends. This is consistent with our earlier finding [121]. Thus we are fortuitously able to test just a few wires in parallel, thereby avoiding the deleterious effects of ensemble averaging.

Another reason for the high device resistance is that the conductivities of metal nanowires fabricated by self-assembly technique can be much less than those of bulk metal [122]. If we assume that the composite conductivity σ of a trilayered metal nanowire is $\sim 1 \times 10^5\ \Omega^{-1}\text{ m}^{-1}$, which is an order of magnitude smaller than typical thin-film conductivity values of metals [116], then we can estimate the resistance of a single wire using the formula $R = l/(\sigma A)$. With $l = 100\text{ nm}$, $A = \pi(50\text{ nm})^2/4$, we get $R \sim 509\ \Omega$. Thus, we can say that very few (~ 2) wires are electrically connected from both sides since the total device resistance is $\sim 300\ \Omega$. That means that only one in 50 million wires are electrically contacted from both ends, on the average. This feature is unique to these structures [121].

The current-voltage characteristic of this device is linear (Figure 6.6) at all temperatures, which indicates that the electrical contacts to the few wires that are connected are ohmic.

6.3 Results and discussion

The magnetoresistance traces at three different temperatures (for a fixed bias current of $10\ \mu\text{ A}$) are shown in Figures 6.7(a) – (c). As indicated in Figure 6.5, the magnetic field is

along the length of the nanowires. This coincides with the easy axes of magnetization for

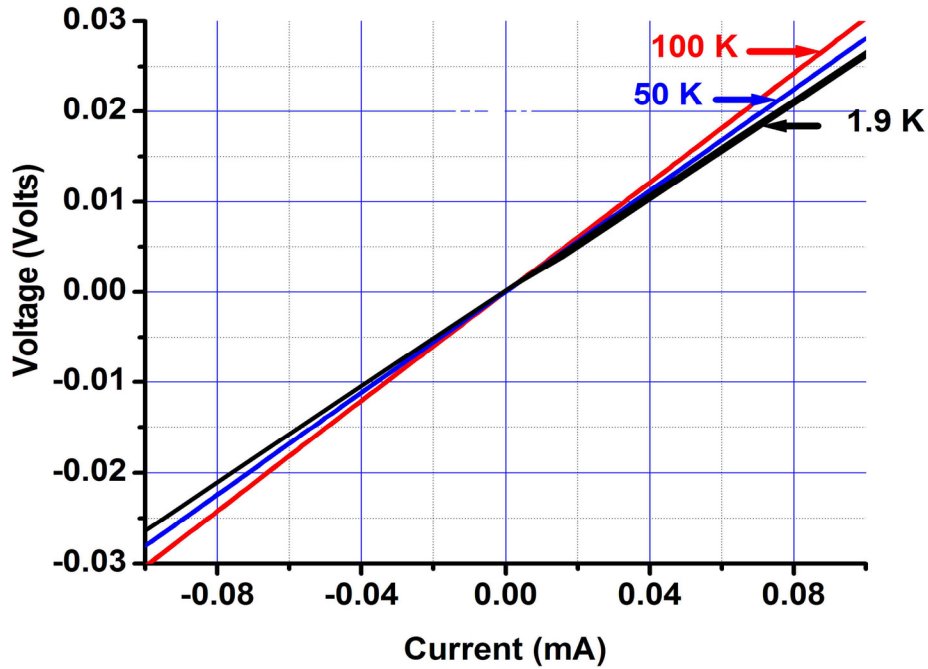


Figure 6.6 The linear I - V characteristics of the device shown in Figure 6.5. The linearity indicates that the various heterojunctions and electrical contacts are ohmic in nature.

the ferromagnetic electrodes. We observe a global positive magnetoresistance which has been reported earlier in similar studies. The background positive magnetoresistance comes about from the anisotropic Hall effect [122]. Against this background, we observe tell-tale magnetoresistance peaks between the coercive fields of the magnetic contacts ($|H_{c,Ni}|$ and $|H_{c,Co}|$, with $|H_{c,Ni}| < |H_{c,Co}|$ in general) which is the characteristic signature of the spin valve effect. In the region $|H_{c,Ni}| < |H| < |H_{c,Co}|$ magnetizations of the nanomagnets are

antiparallel which results in a high device resistance since one contact injects spins of a particular polarization and the other contact blocks these electrons from getting through.

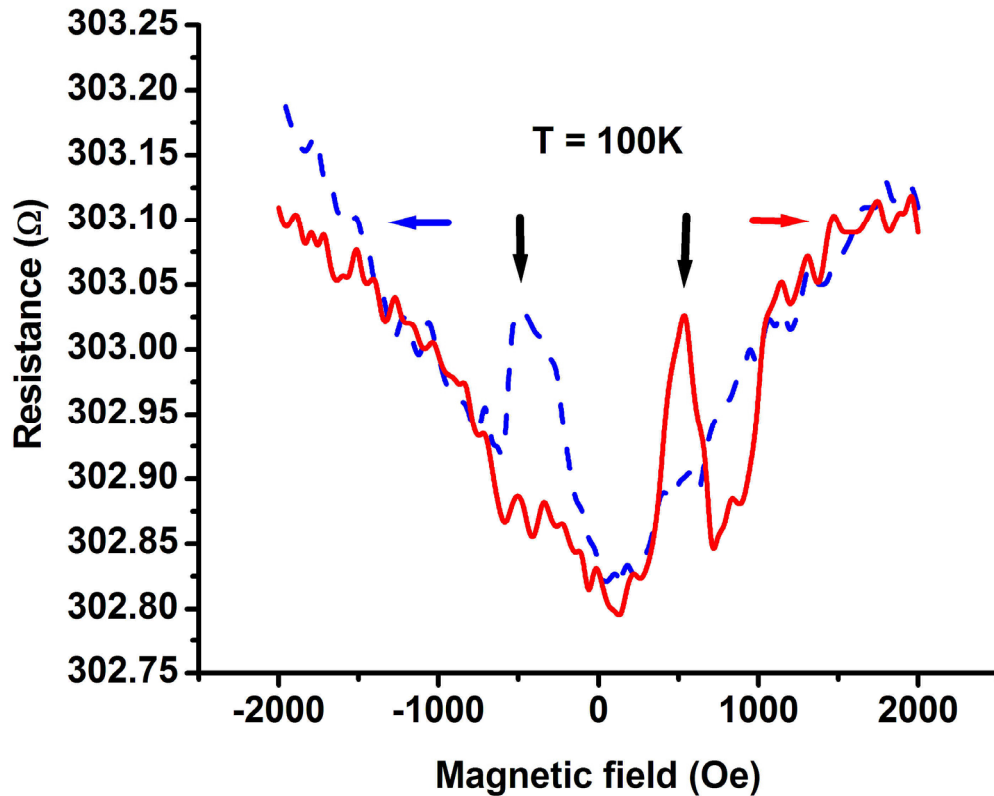


Figure 6.7(a) Magnetoresistance characteristics at 100 K and bias current of 10 microamperes. The spin valve peaks are indicated by the vertical arrows.

This effect manifests itself as the peaks in the magnetoresistance curves. Outside the region $|H_{c,Ni}| < |H| < |H_{c,Co}|$, the magnetizations of the two ferromagnetic contacts are parallel resulting in smaller device resistance. This is the basic spin valve effect, which we observe. Coercivities of Ni and Co nanomagnets electrodeposited in porous alumina template have

been well calibrated in the past [123, 124]. Reference [123] reports coercivity of electrodeposited cylindrical Co nanomagnets as a function of diameter and length.

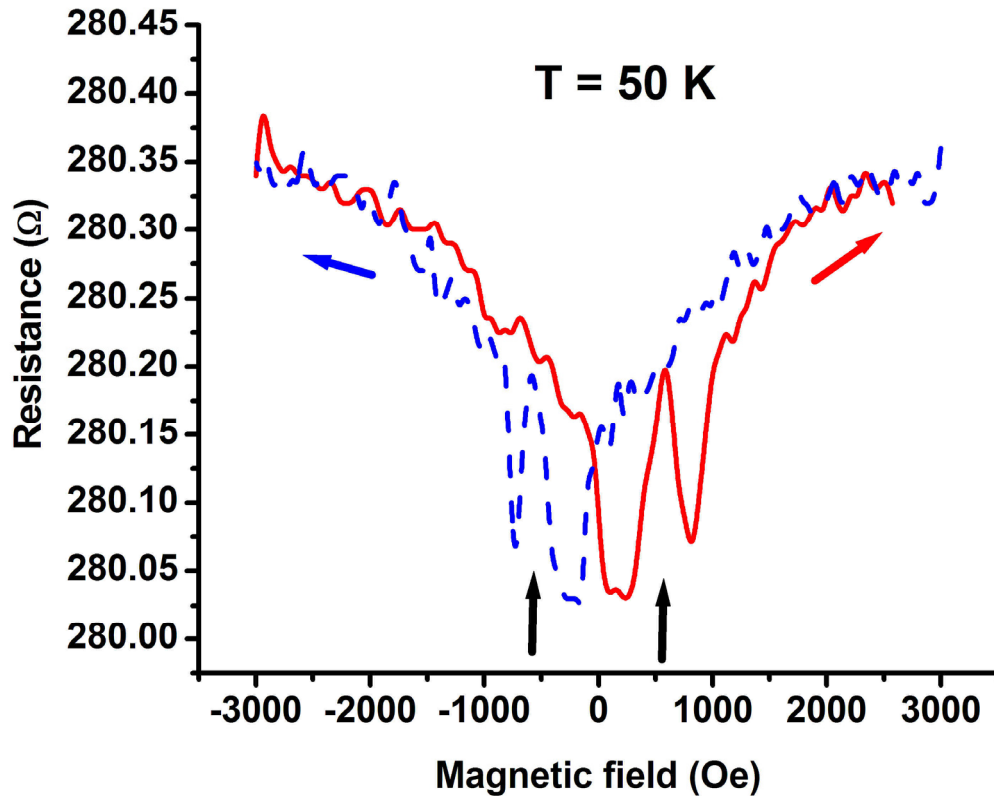


Figure 6.7(b) Magnetoresistance characteristics at 50 K and bias current of 10 microamperes. The spin valve peaks are indicated by the vertical arrows.

Co nanowires with 20 nm length and 10 nm diameter have coercivity ~ 1000 Oe at room temperature. Also coercivity decreases as dot diameter is increased. Extrapolating this trend, in the present case, where Co nanodots have 50 nm diameter (and 20 nm length), coercivity is estimated to be ~ 700 Oe at room temperature. At lower temperatures we

expect to see a somewhat higher value than this estimate. Thus, in the temperature range 1.9 K – 100 K, $|H_{c,Co}| \sim 750$ Oe is reasonable. Similarly, for Ni, extrapolating the data in reference [124] we expect room temperature coercivity of Ni nanodots of 50 nm diameter

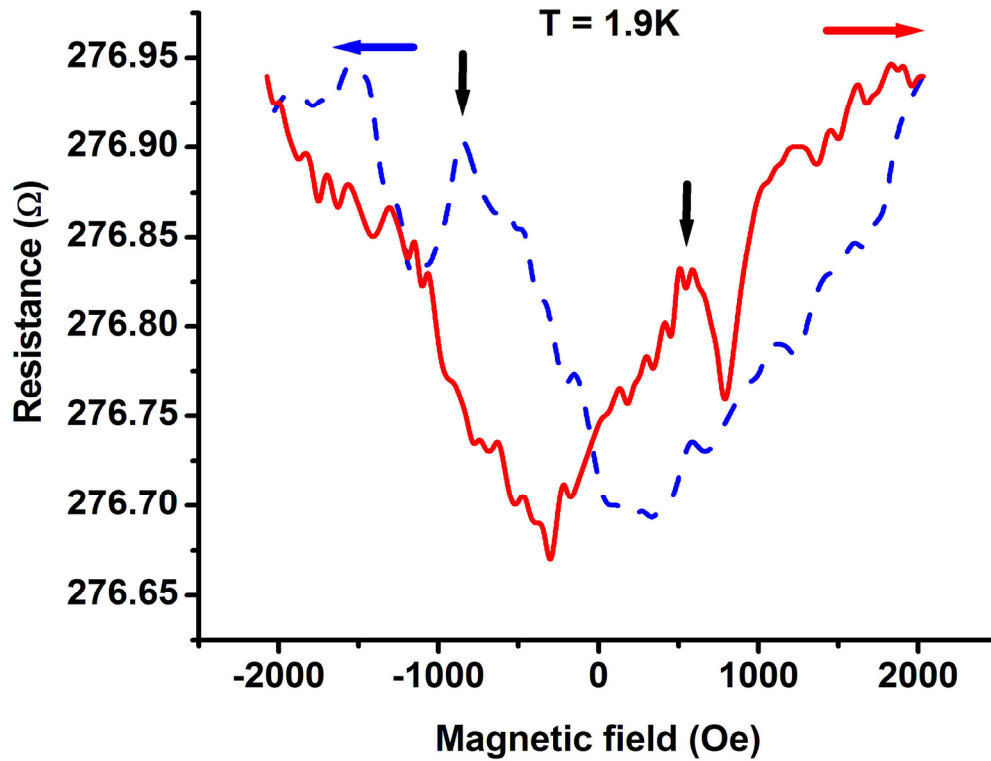


Figure 6.7(c) Magnetoresistance characteristics at 1.9 K and bias current of 10 microamperes. The spin valve peaks are indicated by the vertical arrows.

to be ~ 200 Oe. Thus in the temperature range 1.9 K – 100 K, $|H_{c,Ni}| \sim 250$ Oe is quite likely. Therefore, the magnetizations of the nanomagnets are antiparallel in the range [250 Oe, 750 Oe] in the temperature range 1.9 K – 100 K. We observe magnetoresistance peaks in this field range which confirms that what we observe is indeed the spin valve effect.

It should be noted that the leading edges and trailing edges of the spin valve peaks do not occur at the same magnetic fields at different temperatures. This is expected since the coercivities of the ferromagnets are temperature sensitive. Additionally, we note that the data at 1.9 K are more “noisy” than those at higher temperatures. This is due to telegraph noise caused by surface traps, which is more prominent at lower temperatures.

It is possible to estimate the spin relaxation length in Cu spacer from the knowledge of the spin valve signal ΔR which is the change in device resistance from parallel to antiparallel configuration. We follow the model of reference [116] modified for the classical spin valve geometry:

$$\Delta R = \frac{2 \alpha_F^2 \frac{\lambda_N}{\sigma_N A} e^{(-L/2\lambda_N)}}{(M+1)[M \sinh(L/2\lambda_N) + \cosh(L/2\lambda_N)]} \quad (6.1)$$

where $M = \frac{\lambda_N \sigma_F (1 - \alpha_F^2)}{\lambda_F \sigma_N}$, $\alpha_F = \frac{\sigma_\uparrow - \sigma_\downarrow}{\sigma_\uparrow + \sigma_\downarrow} \equiv$ bulk current polarization of the ferromagnetic

electrodes (assuming they are made of same material), σ_\uparrow (σ_\downarrow) indicates the spin up (down) conductivity of the ferromagnet, σ_N (σ_F) denote the total conductivity of the Cu (ferromagnetic) layer, λ_N (λ_F) is the spin relaxation length in the Cu (ferromagnetic) layer, $L = 40 \text{ nm}$ is the distance between the two ferromagnetic electrodes and A is the cross sectional area through which current flows into the spin valve device. We make the following reasonable estimates to calculate λ_N , which is the spin relaxation length in Cu:

- (a) $\alpha_F = 0.375$ (“average” spin polarization of Ni (33%) and Co electrodes (42%).
- (b) $\sigma_N = 1 \times 10^5 \Omega^{-1} \text{ m}^{-1}$ (electrical conductivity of nanowire Cu embedded in alumina)

(c) $\sigma_F = 1 \times 10^5 \Omega^{-1} m^{-1}$ (“average” electrical conductivity of the nanowire ferromagnets)

(d) $\lambda_F = 5 \text{ nm}$ (spin relaxation length in the ferromagnets, see reference [125])

(e) $A = \pi(50 \text{ nm})^2 \times 2/4 = 3.927 \times 10^{-15} m^2$ (current carrying cross sectional area of the device, assuming ~ 2 nanowires are electrically connected from both sides; each wire has a diameter of 50 nm)

(f) $L = 40 \text{ nm}$ (thickness of the Cu layer, as discussed earlier)

Equation (6.1) ignores any loss of spin polarization at the interfaces between the ferromagnets and the paramagnet. We can ignore this for two reasons: first, the interface area is very small (only $\pi \times 25 \text{ nm}^2$), and second the loss at the interface becomes significant only if there is a large conductivity mismatch between the paramagnet and the ferromagnet. In our case, both the paramagnet and the ferromagnet are metals with similar conductivities. Therefore, the interface loss is minimal.

Note that in case of both Cu and the ferromagnets we have assumed a smaller conductivity value (compared to bulk or thin films) in order to incorporate the increased resistance associated with nanowires. For simplicity we have assumed the same conductivity value for both Cu and ferromagnets. Since we are basically interested in the “order of magnitude” estimates for the spin diffusion length, all of these approximations are justified. The quantity ΔR is determined from the magnetoresistance curves (Figures 6.7(a) - (c)). Using these quantities, we obtain the following estimates of λ_N from equation

(6.1). We can also find the spin lifetime τ using the formula [8] $\lambda_N = \sqrt{\frac{v_F \tau \lambda_m}{3}}$ where

$v_F = 1.57 \times 10^6$ m/s is the Fermi velocity in Cu [126] and $\lambda_m \approx 5$ nm [8] is the mean free path (limited by surface roughness scattering) in Cu spacer. Note that this value of λ_m is somewhat smaller than the bulk value (~ 50 nm). This is because of increased surface scattering in nanowires reduces the mean free path by about an order of magnitude, which is consistent with assuming that the conductivity in nanowires is 10 times less than that in bulk samples. Based on all these assumptions, we estimate the spin diffusion lengths and spin relaxation times shown in the following table as a function of temperature.

Table 6.1 Spin relaxation lengths and spin relaxation times at various temperatures

Temperature (K)	ΔR (Ω)	λ_N (nm)	τ (fs)
1.9	0.18	18	123.82
50	0.17	16	97.83
100	0.17	16	97.83

Comparing these values to the value of spin relaxation length in thin films (reference [116]), we find that the spin relaxation length has been *reduced* by almost an order of magnitude, compared to thin films. This is a consequence of increased coulomb scattering, caused by the surface states, which decreases the mobility and therefore exacerbates the EY mechanism, while simultaneously quenching the DP mechanism. Thus, what we are measuring is the *spin relaxation rate associated with pure EY mechanism alone*. Typical mean free time in the Cu spacer (determined by surface roughness scattering) is

approximately given by $\tau_f = \lambda_m / v_F = 3.1$ fs. Thus, on an average, spin relaxation due to EY mechanism occurs over 30-40 ($= \tau / \tau_f$) momentum scattering events.

Note from the above table that spin relaxation length is relatively independent of temperature. This is consistent with the EY mechanism. The primary source of the EY relaxation is the elastic scattering caused by the high concentration of charged surface states. Since this type of elastic scattering does not involve phonons, its effect is expected to be relatively temperature independent.

The temperature independence also tells us that electron-electron scattering, no matter how frequent, is not a major contributor to spin relaxation. First, electron-electron scattering is spin-conserving. Whatever spin momentum one electron loses is picked up by the other so that the ensemble spin is not affected directly. Second, and more importantly, the momentum relaxation rate of a carrier due to electron-electron scattering is strongly temperature dependent. It has been shown that the momentum relaxation rate and the spin relaxation rate due to the EY mechanism have the same temperature dependence [31, 127]. Therefore, if electron-electron scattering were a significant contributor, we would have found a strong temperature dependence of the spin relaxation rate. Since we do not, we conclude that electron-electron scattering does not play a major role.

Figure 6.8 shows magnetoresistance plot at a higher bias current of $100 \mu\text{A}$. However, the height of the spin valve peak does not change appreciably by this tenfold increase in bias. Surface roughness scattering does not strongly depend on applied bias and hence spin valve signal is expected to be weakly dependent on it at least in $10 - 100 \mu\text{A}$ range.

We have not gone past the $100\ \mu\text{A}$ limit in order to prevent sample damage. We point out that the voltage on the sample at $100\ \mu\text{A}$ is $100\ \mu\text{A} \times 300\ \Omega = 30\ \text{mV}$. Therefore, the electric field on the Cu spacer layer is $30\ \text{mV}/100\ \text{nm} = 3\ \text{kV/cm}$ (assuming that the electric field is uniform throughout the nanowire since all metals have approximately the same conductivity).

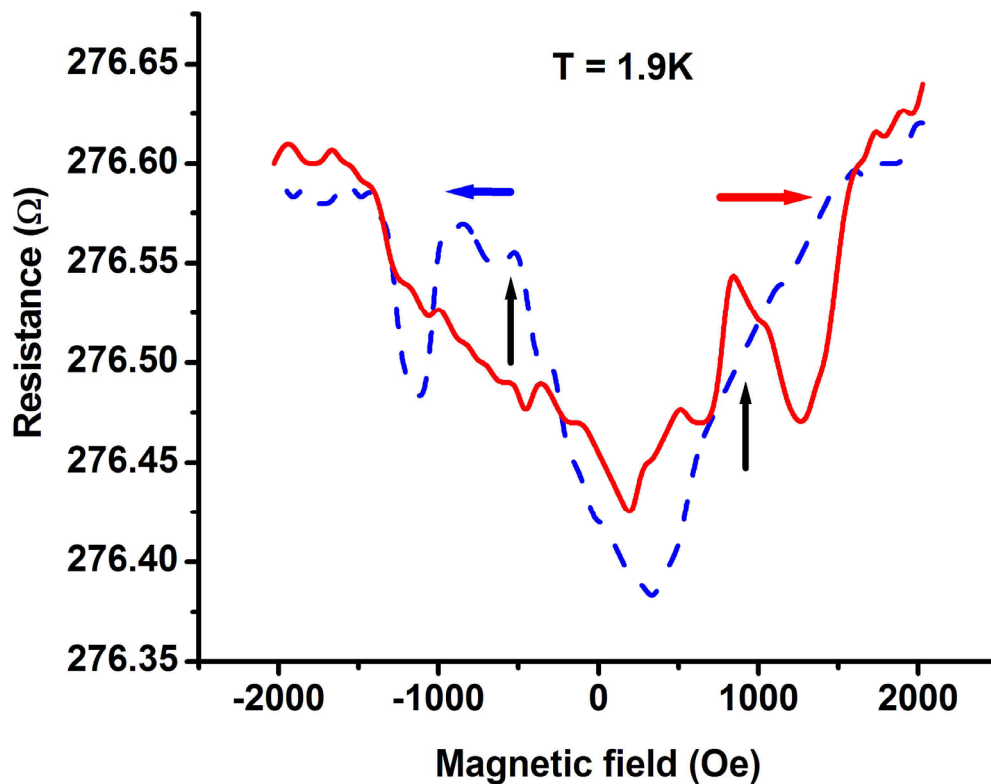


Figure 6.8 Magnetoresistance characteristics at 1.9 K and bias current of 100 microamperes. The spin valve peaks are indicated by the vertical arrows.

Reference [116] reported a significant decrease in spin relaxation length with an increase in temperature for Cu thin films. This is in sharp contrast with what we find. There are two

possible explanations for this difference. Either the primary relaxation mode in thin films is not the EY process which is relatively temperature independent if it is associated with elastic scattering events, or the primary relaxation mode is still the EY process, but it is associated with inelastic (phonon-assisted) scattering processes which are strongly temperature dependent. The first possibility is unlikely. If the primary spin relaxation mode is not the EY process, then it must be the DP process. However, the DP relaxation rate has *weak* temperature dependence [128] and therefore cannot explain a strong temperature dependence of the relaxation rate. Therefore it is likely that in thin films, which have a much smaller surface-to-volume ratio than nanowires, the primary mobility degradation mechanism is not elastic surface scattering, but inelastic phonon scattering, which has strong temperature dependence. Since the temperature dependence of the momentum relaxation rate and the spin relaxation rate is the same in the EY mode, we expect the spin relaxation rate to be strongly temperature dependent if momentum relaxation occurs primarily via phonons.

6.4 Conclusion

In conclusion, we have isolated the EY mechanism in Cu by utilizing a nanowire and studied the spin relaxation rates associated with this mechanism at various temperatures and electric fields. We find that since spin relaxation is associated with elastic scattering caused by charged surface states, the spin relaxation rate is both temperature and field insensitive.

CHAPTER 7. Spin Relaxation in a Nanowire Organic Spin Valve: Observation of Extremely Long Spin Relaxation Times*

Overview

In this chapter we report spin-valve behavior in an “organic nanowire” consisting of three layers - cobalt, tris-8-hydroxy-quinolinolato aluminum (Alq_3) and nickel – all nominally 50 nm in diameter. From the height of the spin-valve peaks we extract the spin relaxation length in Alq_3 . Using the conductivity value of the carriers in the organic layer we have estimated a typical range of spin relaxation time in this material. Surprisingly, the spin relaxation time in Alq_3 is extremely long, at least a few milliseconds, and this is relatively temperature independent up to 100 K. Analyzing the experimental data, we also conclude that the dominant spin relaxation mechanism in Alq_3 is the Elliott-Yafet mode. To our knowledge, this is the first demonstration of an organic nanoscale spin-valve, as well as the first determination of the primary spin relaxation mechanism in organics. Interestingly some samples exhibit “inverse spin valve” effect in which magnetoresistance “troughs” are

* This work has been submitted for publication as

[129] S. Pramanik, C-G. Stefanita, S. Patibandla, S. Bandyopadhyay, K. Garre, N. Harth, and M. Cahay, "Spin relaxation in a nanowire organic spin valve: observation of extremely long spin relaxation times," www.arxiv.org/cond-mat/0508744, 2006 and

[130] S. Pramanik, S. Bandyopadhyay, K. Garre, and M. Cahay, "Normal and inverse spin valve effect in organic semiconductor nanowires and the background monotonic magnetoresistance," accepted for publication (Nov. 2006), Physical Review B.

observed in between the coercivities. This is caused by resonant tunneling through localized impurity states in the organic. Peaks are always found to be accompanied by a positive, monotonic background magnetoresistance, while troughs are accompanied by a negative, monotonic background magnetoresistance. This curious correlation suggests that the background magnetoresistance, whose origin has hitherto remained unexplained, is probably caused by the recently proposed phenomenon of magnetic field induced enhancement of spin flip scattering in the presence of spin-orbit interaction [37].

7.1 Introduction

π - conjugated organic semiconductors are an important platform for “spintronics” that purports to harness the spin degree of freedom of a charge carrier to store, process, and/or communicate information [131]. Spin-orbit interaction in organic is typically very weak, which should result in long spin relaxation times [132]. Many organics are also optically active [133] and therefore could lead to multi-functional “opto-spintronic chips” where optics and spintronics are integrated to perform seamless signal processing and communication functions. Such chips will be inexpensive, versatile, and the tremendous flexibility afforded by synthetic organic chemistry offers limitless possibilities in terms of the variety and complexity of structures that can be realized. Already some efforts have been made to combine optics with spintronics in organics [134].

Recently, a thin-film organic spin valve structure consisting of an organic semiconductor placed between two ferromagnetic electrodes was demonstrated [131]. Some theoretical

effort has also been made to understand spin transport in such organics [135, 136], but any insight into the primary spin relaxation mechanism is still lacking. These structures (and/or their derivatives) [137-143] typically show a large background monotonic magnetoresistance, which can either be positive or negative. The origin of this magnetoresistance has also remained a mystery. Some attempts have been made to explain it by invoking weak localization and anti-localization [141] but it is extremely unlikely that these are the causes since the magnetoresistance is typically observed up to room temperature [141]. Localization or anti-localization requires preservation of quantum mechanical phase coherence of charge carriers over long distances. That is unlikely to happen at room temperature, particularly in organics where transport occurs mainly via phonon-assisted hopping. Thus there is a need for alternate explanation. In this chapter we will describe an exhaustive study of spin transport in nanowire organic spin valve structures and offer an alternate explanation for the background magnetoresistance, which does not require phase coherence and therefore can explain its occurrence at relatively high temperatures.

As discussed in Chapter 1, there are four major spin relaxation mechanisms in solids: the D'yakonov-Perel' (D-P) [32, 33], the Elliott-Yafet (E-Y) [30, 31], hyperfine interaction between nuclear and carrier (electron or hole) spins [35] and the Bir-Aronov-Pikus (B-A-P) mechanism [34]. They dominate in both semiconductors and metals [127].

It is important to establish which of these four mechanisms is the most dominant in organics. The two likely candidates are the D-P and the E-Y mechanisms since the B-A-P mechanism is absent in unipolar transport and the hyperfine interaction is very weak in

organics. The D-P mechanism is suppressed by quasi one-dimensional confinement [47, 71, 144]. Therefore, if the relaxation rate is found to decrease upon confining carriers to a quasi one dimensional structure, then we will have established that the primary mechanism is the D-P mode. On the other hand, the E-Y mechanism can be exacerbated by quasi one-dimensional confinement if the latter increases the momentum relaxation rate. Thus, any increase in the spin relaxation rate upon quasi one dimensional confinement is a strong indicator that the E-Y mechanism is dominant.

7.2 Experimental procedure

Based on this premise, we have fabricated a nanowire spin valve structure consisting of three layers – cobalt, Alq₃ [tris-(8-hydroxy-quinolinolato) aluminum] and nickel. The structures were synthesized by using a porous alumina membrane containing a well ordered hexagonal close packed arrangement of pores with 50 nm diameter. The fabrication of such films has been described in the previous chapter. It is produced on an aluminum foil. There is an alumina “barrier layer” at the bottom of the pores which is removed by a reverse polarity etching technique [120] so that the underlying aluminum is exposed at the bottom of the pores. Nickel is then electrodeposited selectively within the pores from a mildly acidic solution of NiSO₄ : 6 H₂O by applying a dc bias of 1.5 V at a platinum counter-electrode with respect to the aluminum substrate. Small deposition current ($\sim \mu\text{A}$) ensures well-controlled and slow-but-uniform electrodeposition of Ni inside the pores. We calibrated the deposition rate of Ni under these conditions by monitoring the deposition current during electrodeposition of Ni inside pores of known length. The

deposition current increases drastically when the pores are completely filled and a nickel percolation layer begins to form on the surface. The deposition rate is determined by calculating the ratio of the pore length to pore filling time. According to this calibration, the thickness of the nickel layer (deposited inside the pores) is approximately 500 nm. TEM characterization of these Ni nanowires showed that the wire lengths are almost uniform and indeed conform to ~ 500 nm. These samples are air-dried and then Alq_3 is resistively evaporated on the porous film through a mask with a window of area 1 mm^2 in a vacuum of 10^{-7} Torr. The rate of deposition is in the range $0.1 - 0.5$ nm/s. During evaporation, Alq_3 seeps into the pores by surface diffusion and capillary action, and reaches the nickel. The fact that Alq_3 is a short stranded organic of low molecular weight is helpful in transporting it inside the pores. The thickness of the evaporated Alq_3 layer is monitored by a crystal oscillator and subsequently confirmed by TEM analysis. Finally, cobalt is evaporated on the top without breaking vacuum (as in reference [131]). The fabrication procedure and the resulting structure are schematically depicted in Figure 7.1. The thickness of the cobalt layer (as deposited inside the pores) is also ~ 500 nm since the total pore length is $\sim 1 \mu\text{m}$. Thus we end up with an array of *nominally identical* spin valve nanowires. Since the cobalt contact pad has an area of $\sim 1 \text{ mm}^2$, approximately 2×10^8 nanowires are electrically contacted in parallel (the areal density of the nanowires is $2 \times 10^{10} \text{ cm}^{-2}$). Note that the surrounding alumina walls provide a natural encapsulation and protect the Alq_3 layer from moisture contamination. For electrical measurements, we attach two gold wires to the top cobalt and the bottom aluminum layers using silver epoxy.

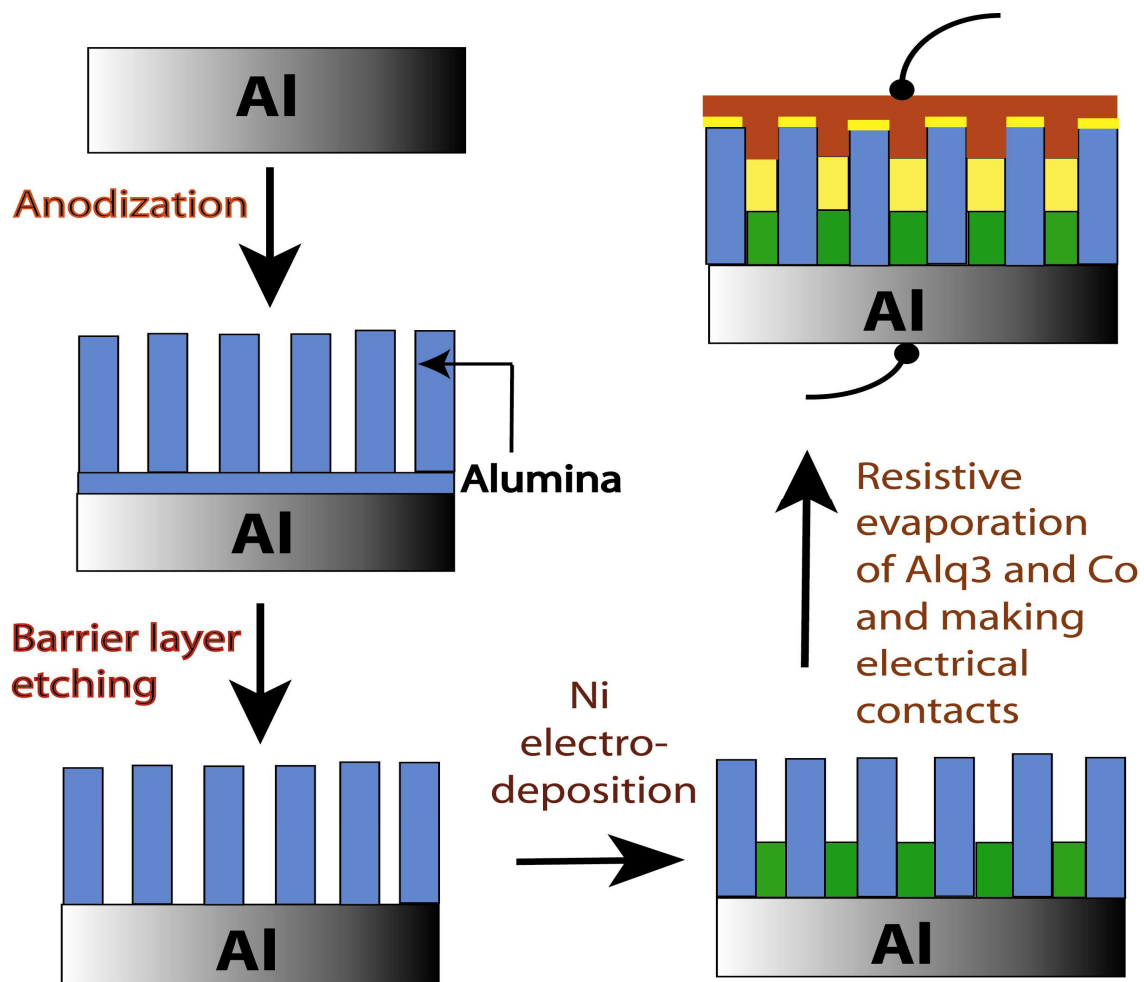


Figure 7.1 Schematic description of the sample fabrication process. The red, yellow and green layers indicate cobalt, Alq₃ and nickel respectively.

7.3 Results and discussion

From measured conductivity values, we can estimate the number of nanowires that are electrically connected from both ends. For example, resistivity of Alq₃ thin film is typically $10^5 \Omega\text{-cm}$ at room temperature [145]. When Alq₃ is confined in pores, we assume that the resistivity increases by an order of magnitude because of the increase in surface scattering.

This is a typical assumption used in similar contexts [113]. Therefore the resistivity of Alq₃ nanowires is 10⁶ Ω-cm. The resistivities of the ferromagnetic nanowire electrodes are ~ 10⁻³ Ω-cm [113]. Thus the resistance of a single trilayered nanowire is 10¹¹ Ω. Since the resistance of the sample is ~ 1 kΩ, we estimate that 50% of the nanowires (~10⁸) under the cobalt contact pad are electrically connected from both ends. Note that since the resistivity of Alq₃ is 9 orders of magnitude higher than the resistivities of the ferromagnets, during transport experiments, we will always probe the resistance of the Alq₃ layer only, and not the resistance of the ferromagnetic electrodes, which are in *series* with the Alq₃ layer. Thus, all features in the resistance accrue from the organic layer and have nothing to do with the ferromagnetic contacts. Consequently, if there are features originating from the anisotropic magnetoresistance effects in the ferromagnets, we will never see them.

To confirm that the contribution of the ferromagnetic layers to the resistance of the structure is indeed negligible, we fabricated a set of control samples without any Alq₃ layer. Note that a parallel array of 2 × 10⁸ Ni/Co bi-layered nanowires (contacted by Al at bottom and a thin film of Co at top with area 1 mm²) would produce a resistance of ~ 25 μΩ, which is below the sensitivity of our measurement apparatus. Therefore we made control samples where we probe only ~ 500 nanowires. The trick employed to achieve this was to remove the “barrier layer” incompletely from the bottom (intentionally), so that only a small fraction of the pores opened up from the bottom. We measure a resistance of ~ 10 Ω in the control samples at room temperature, which tells us about 500 bi-layered nanowires are electrically probed.

The magnetoresistance of the control samples were measured in a Quantum Design Physical Property Measurement System with a bias current of 10 μA , over a magnetic field range of 0 – 6 kOe and at a temperature of 1.9 K. A typical trace is shown in Figure 7.2. We never observed any magnetoresistance peak or trough in these samples, but observed a monotonic positive magnetoresistance $\delta R(|B|) = R(|B|) - R(0)$, where B is the magnetic flux density. This magnetoresistance effect either accrues from the anisotropic magnetoresistance effect associated with the ferromagnetic contacts or the magnetoresistance of the aluminum substrate.

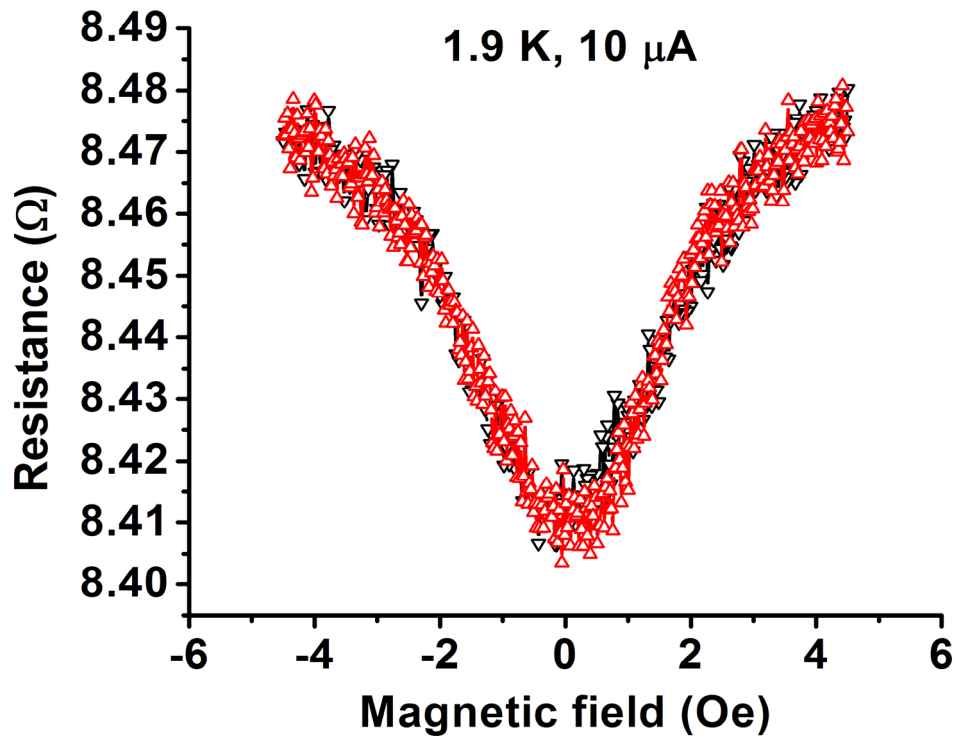


Figure 7.2 Magnetoresistance trace of the control sample, consisting of ~ 500 Ni-Co bilayered nanowires (no Alq_3)

However, the maximum value of $\delta R(|B|)$ that we observed over the entire measurement range (0 – 5 kOe) was only $\sim 0.08 \Omega$, which is more than an order of magnitude smaller than the resistance peak ΔR measured in the tri-layered structures (see later). Thus the resistance peak measured in the tri-layered structures undoubtedly originates from the spin valve effect and has nothing to do with either the anisotropic magnetoresistance associated with the ferromagnetic contacts, or the magnetoresistance of the aluminum substrate.

We fabricated ~ 90 tri-layered samples using the procedure described in section 7.2. Room temperature resistances of these samples range from 1 – 10 k Ω depending on the number of nanowires that are electrically connected from both ends. This number varies because the process of barrier layer removal is not precisely controllable. The magnetoresistance of these samples were measured in a Quantum Design Physical Property measurement system. The measured distribution of spin valve signal $\Delta R/R$ is shown in Figure 7.3. The distribution is very broad and peaks near zero, i.e. most samples do not exhibit any measurable spin valve signal. Among the remaining samples, some exhibit positive spin valve signals and others exhibit negative signals.

The insets of Figure 7.3 show the magnetoresistance traces for the highest positive and negative spin valve signals that we have measured among all samples tested. Typical magnetoresistance traces indicating normal spin valve response (with positive background magnetoresistance) at four different temperatures are shown in Figures 7.4(a) – (d) where the magnetic field is parallel to the axis of the wires. This direction also corresponds to the easy axis of magnetization for the nickel and cobalt nanomagnets within the pores.

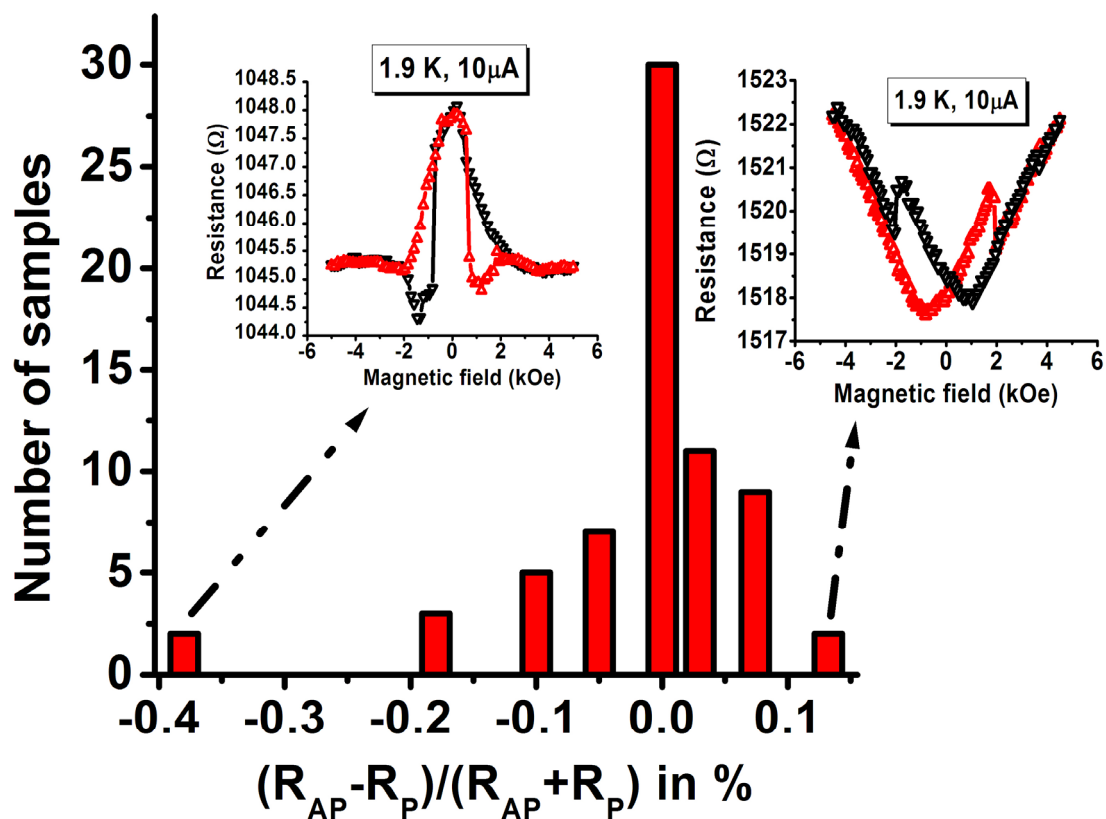


Figure 7.3 Distribution of the spin valve signal

This background *monotonic* magnetoresistance which is often observed in organic semiconductors and is dubbed “organic magnetoresistance” (OMAR) [146], but more importantly, we find magnetoresistance peaks located between fields of 800 Oe and 1800 Oe which are the coercive fields of the nickel and cobalt nanowires. This is the tell-tale signature of the spin valve effect. The height of this peak decreases with increasing temperature and is barely visible at 100 K.

In these structures, it is not possible to measure the coercivities of the cobalt and nickel contacts individually using conventional techniques. SQUID measurements do not resolve the coercivities. However, we had individually measured the coercivities of nickel and cobalt nanowires in the past [123, 124]. For nickel, [124] reported a maximum coercivity of 950 Oe at room temperature for nanowires of diameter 18 nm and it decreased to 600 Oe for wider nanowires of 21 nm diameter. Since coercivity increases with decreasing temperature [147], a value of 800 Oe is quite possible in 50-nm diameter nanowires at 1.9 K. The coercivity of cobalt nanowires has been studied extensively in reference [123]. The coercivity of 22 nm diameter wires was found to be > 1600 Oe at room temperature, so that the coercivity of 50 nm wires can quite likely be 1800 Oe at the low temperature of 1.9 K. Thus, the leading and trailing edges of the peaks in Figures 7.4(a) – (d) seem to occur at the coercive fields of the ferromagnetic contacts.

Figure 7.5 shows the magnetoresistance traces of a sample exhibiting a negative spin valve signal at four different temperatures. As before, spin valve signals manifest between 800 Oe and 1800 Oe, which represent the coercive fields of the Ni and Co nanowire electrodes respectively. The bias current is kept constant at $10 \mu\text{A}$. The spin valve signal decreases with increasing temperature indicating that the spin diffusion length in the organic decreases with increasing temperature.

Figure 7.6 shows the bias current dependence of the negative spin valve signal in a typical sample at a constant temperature of 1.9 K. As the bias current is increased, the spin valve signal decays rapidly and at $200 \mu\text{A}$, no signal is measurable with our apparatus.

Figure 7.5 also shows that there is a background monotonic magnetoresistance $\delta R(|B|)$ accompanying the spin valve signal and its sign is negative ($R(|B|) < R(0)$). We found consistently that whenever the spin valve signal is negative, the background magnetoresistance is also negative, and whenever the spin valve signal is positive, the background magnetoresistance is positive (see the insets of Figure 7.3). The background magnetoresistance has very little sensitivity to temperature (Figure 7.5), but it is extremely sensitive to bias, as can be seen in Figure 7.6. It disappears at a bias current of 200 μA .

From the relative height of the resistance peak $\Delta R / R$ shown in Figures 7.4 (a) – (d), 7.5 and 7.6 we can extract the spin diffusion length in the Alq_3 layer following the technique employed in reference [131]. We first assume that there is no loss of spin polarization at the interface between Alq_3 and the injecting ferromagnetic contact because of the so-called self adjusting capability of the organic [131, 148]. Next, we assume, as in reference [131], that there is a potential barrier at the organic/ferromagnet interface that the injected carriers tunnel through with a surviving spin polarization P_1 . This barrier could be the Schottky barrier due to the contact potential. After this, the carriers drift and diffuse through the remainder of the organic layer under the influence of the electric field, with exponentially decaying spin polarization $\exp[-(d-d_0) / \lambda_T]$ where d is the total width of the organic layer, d_0 is the spatial extent of the potential barrier, and λ_T is the spin diffusion length in Alq_3 at a temperature T . The Schottky barrier at the detecting contact is lowered by the electric field and therefore does not present a potential barrier for tunneling. This

picture is adapted from reference [131]. Finally, if the spin polarization at the Fermi level of the detecting contact is P_2 , then $\Delta R/R$ is given by the Julliere formula [149]

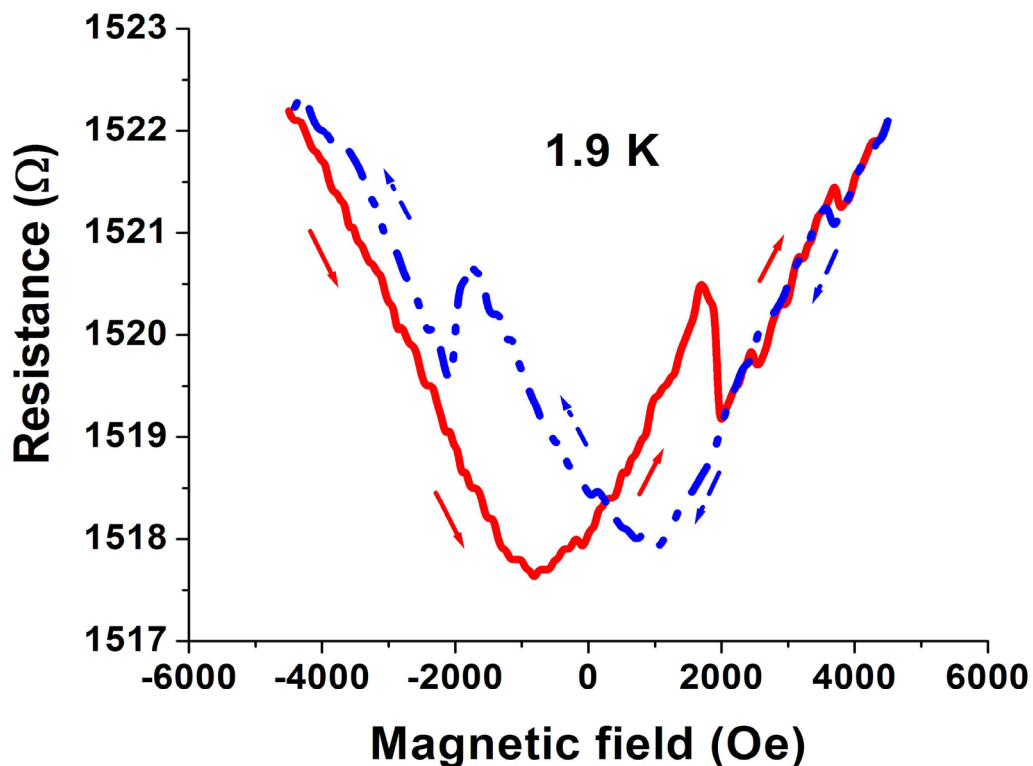


Figure 7.4 (a) Magnetoresistance trace of Alq₃ nanowire at 1.9K. The magnetic field is parallel to the wire axis. Solid and broken arrows indicate reverse and forward scans of the magnetic field. The spin valve peaks occur between +(-)800 Oe and +(-)1800 Oe.

$$\frac{\Delta R}{R} = \frac{2P_1P_2e^{-(d-d_0)/\lambda_T}}{1-P_1P_2e^{-(d-d_0)/\lambda_T}} \quad (7.1)$$

We will now assume that $d_0 \ll d$. Later we will show that this assumption is valid. In that case, the loss of spin polarization in tunneling through the potential barrier is negligible. Therefore, P_1 is approximately the spin polarization of the injecting contact. Since the spin

polarization in cobalt and nickel at their Fermi energies are 42% and 33% respectively [150], $P_1 = 0.42$ and $P_2 = 0.33$.

In order to determine the value of d , we have carried out transmission electron microscopy (TEM) of the nanowires. The wires were released from their alumina host by dissolution in very dilute chromic/phosphoric acid, washed, and captured on TEM grids for imaging. The TEM micrograph of a typical wire is shown in Figure 7.7. The Alq_3 layer thickness d is found to be 33 nm, which is quite close to the layer thickness estimated from the crystal oscillator used to monitor thickness during the evaporation of Alq_3 (that value was 30 nm). This agreement gives us confidence that d does not vary too much from one wire to another. We assume that it varies by ± 5 nm when we calculate λ_T . This will introduce some uncertainty in the spin diffusion length.

Current voltage characteristics of the nanowires are shown in Figure 7.8. They are symmetric because of equal coupling to the contacts [151], but non-linear between -3.5 and 3.5 V at all measurement temperatures, indicating that the contacts are Schottky in nature. This means there has not been significant inter-diffusion of Co or Ni into the Alq_3 layer, since that would have produced an ohmic contact. As a result, the layer thickness d is well defined in the nanowires, which allows us to apply Equation (7.1) to estimate λ_T . In estimating λ_T from Equation (7.1), we assumed that $d - d_0 \cong d$. If this approximation is valid, then the estimated λ_T will be independent of d . To confirm that fact, we fabricated another set of samples with slightly smaller d . Figure 7.9 shows the TEM micrograph of a wire from this set where the layer thickness is found to be 26 nm. The quantity λ_T

measured from this set at any temperature agrees to within ~10% with that measured from the other set at the same temperature. Therefore, λ_T is reasonably independent of d . The values of λ_T as a function of temperature are plotted in Figure 7.10. Comparing the measured values of λ_T to those reported in thin films of Alq₃ (45 nm at 4.2 K) [131], we find that quasi one dimensional confinement has actually *reduced* λ_T by almost an order of magnitude. If the D-P mechanism were the primary cause of spin relaxation, then λ_T should have increased. Since we find the opposite trend, we conclude that the primary relaxation mechanism is the E-Y mechanism.

Elliott has derived a relation between the spin relaxation time τ_s and the momentum relaxation time τ_m [30] which Yafet has shown to be temperature independent [31]:

$$\frac{\tau_m}{\tau_s} \propto \frac{\Delta}{E_g} \quad (7.2)$$

Here Δ is the spin orbit interaction strength in the band where the carrier resides (in our case the LUMO band) and E_g is the energy gap to the nearest band (in our case the HOMO-LUMO gap).

Since $\tau_s(T) = \lambda_T^2 / D(T) = m^* \lambda_T^2 / (k T \tau_m)$, where $D(T)$ is the temperature dependent diffusion coefficient related to the mobility by the Einstein relation and m^* is the effective mass, Equation (7.2) can be recast as $(\tau_m^2 k T / m^* \lambda_T^2) \propto \Delta / E_g$. Since neither Δ nor E_g is affected by quasi one-dimensional confinement, we can posit that at any temperature the following equation will hold:

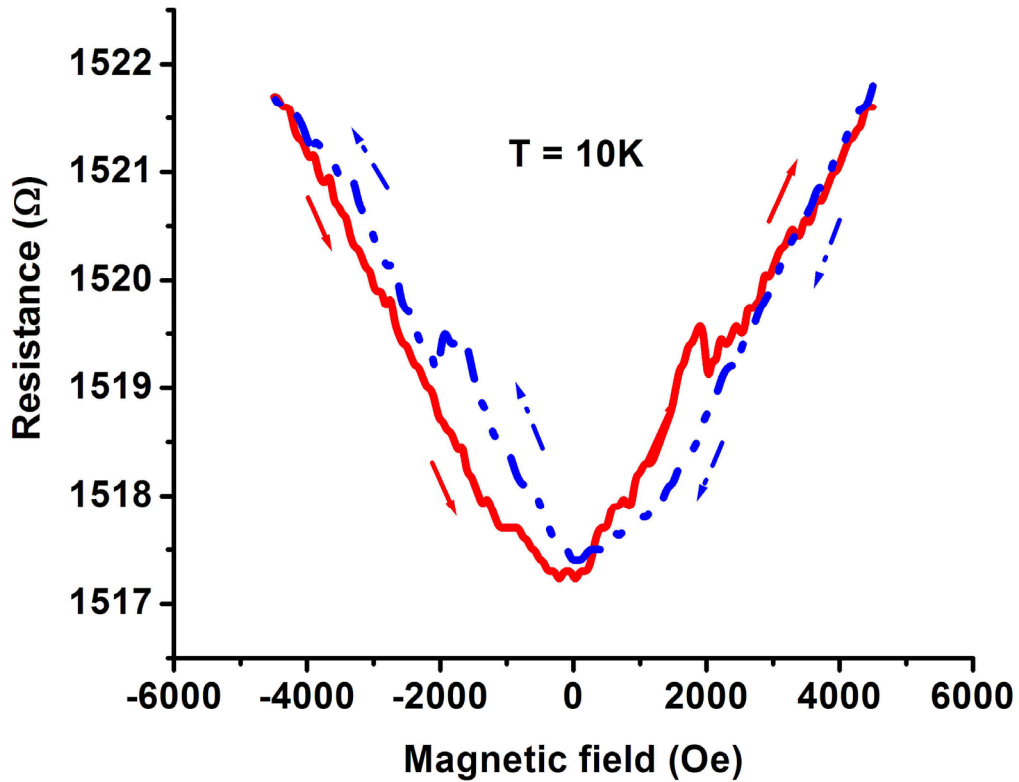


Figure 7.4 (b) Magnetoresistance trace of Alq₃ nanowire at 10K. The magnetic field is parallel to the wire axis. Solid and broken arrows indicate reverse and forward scans of the magnetic field. The spin valve peaks occur between + (-) 800 Oe and + (-) 1800 Oe.

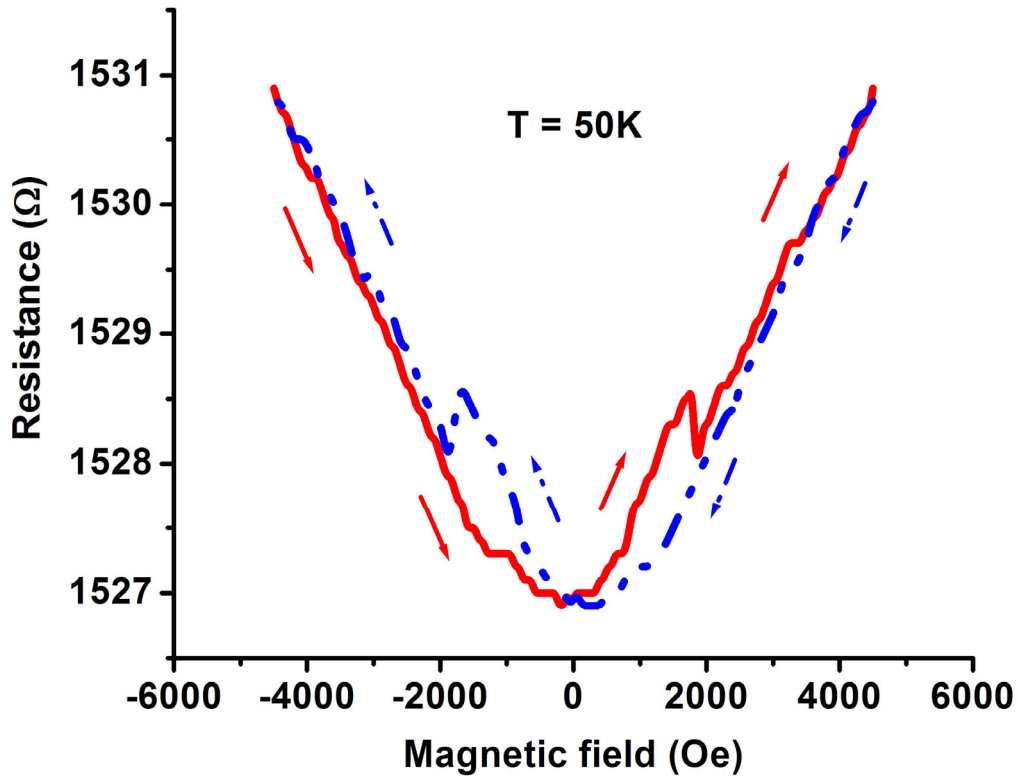


Figure 7.4 (c) Magnetoresistance trace of Alq₃ nanowire at 50K. The magnetic field is parallel to the wire axis. Solid and broken arrows indicate reverse and forward scans of the magnetic field. The spin valve peaks occur between + (-) 800 Oe and + (-) 1800 Oe.

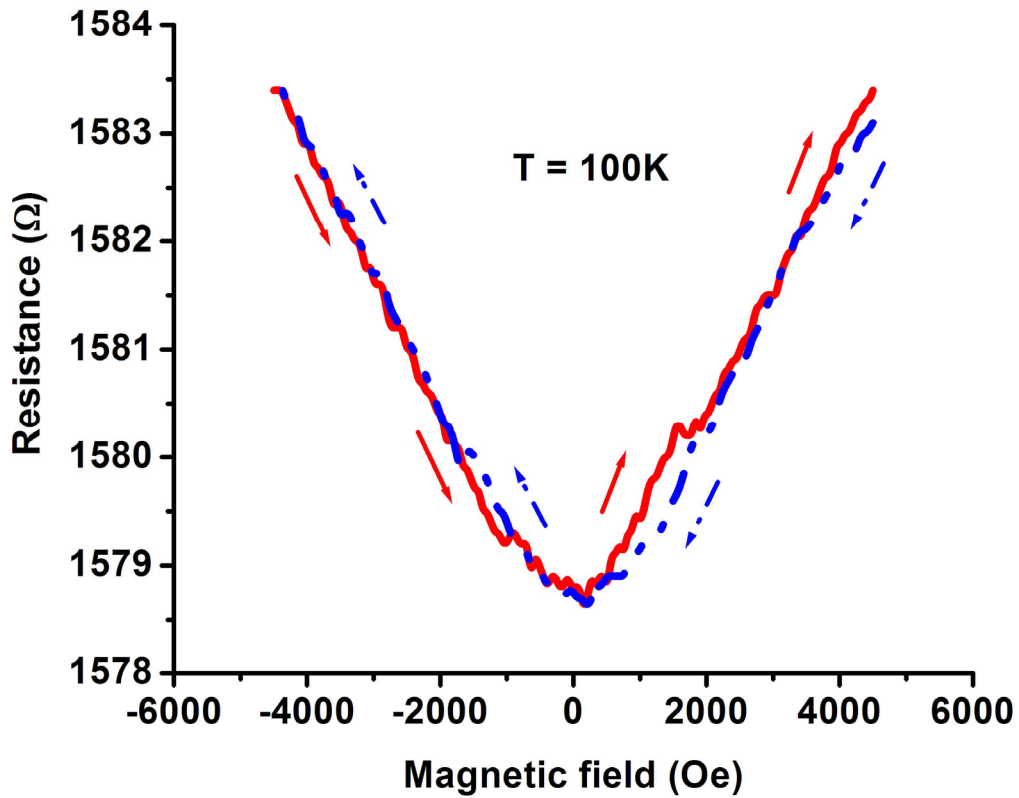


Figure 7.4 (d) Magnetoresistance trace of Alq₃ nanowire at 100K. The magnetic field is parallel to the wire axis. Solid and broken arrows indicate reverse and forward scans of the magnetic field. The spin valve peaks occur between + (-) 800 Oe and + (-) 1800 Oe.

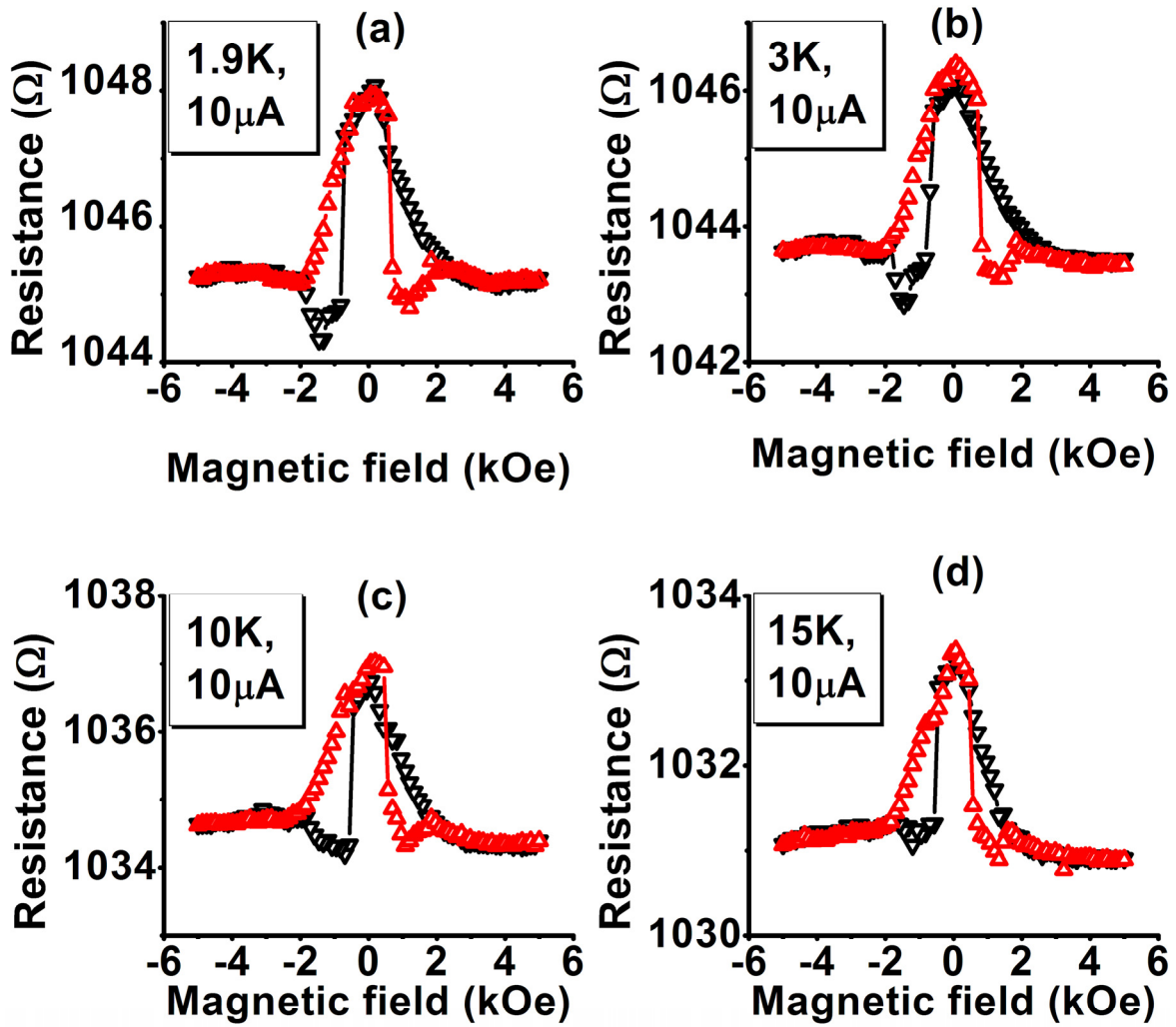


Figure 7.5 Inverse spin valve effect and background negative magnetoresistance in Ni-Alq₃-Co nanowires at four different temperatures and fixed bias of 10 μ A rms.

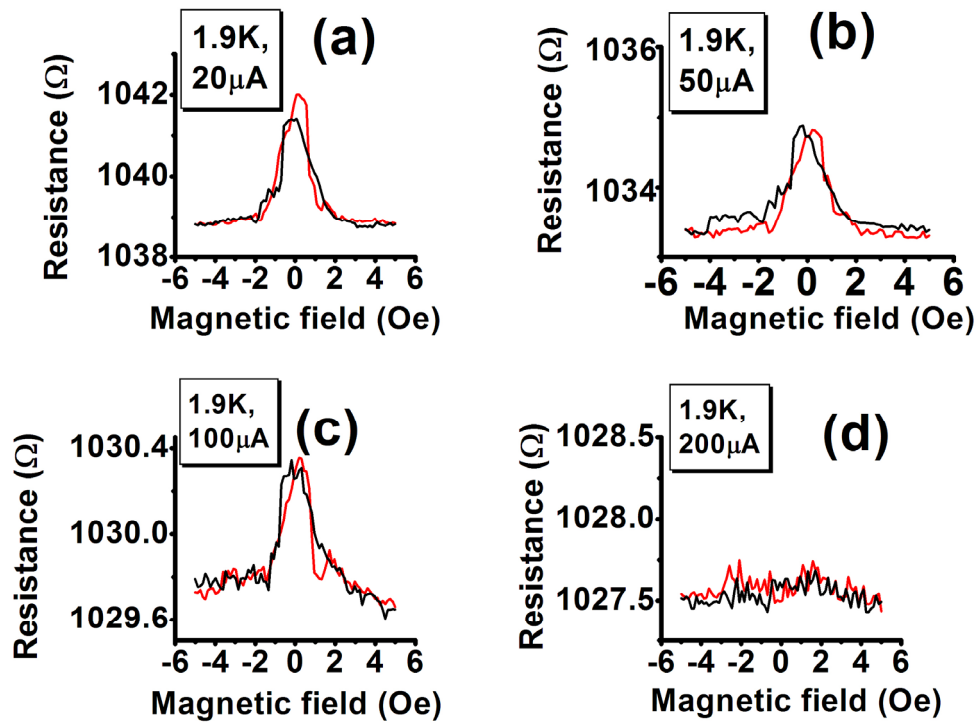


Figure 7.6 Inverse spin valve effect and background negative magnetoresistance in Ni-Alq₃-Co nanowires at four different bias values and fixed temperature of 1.9 K.

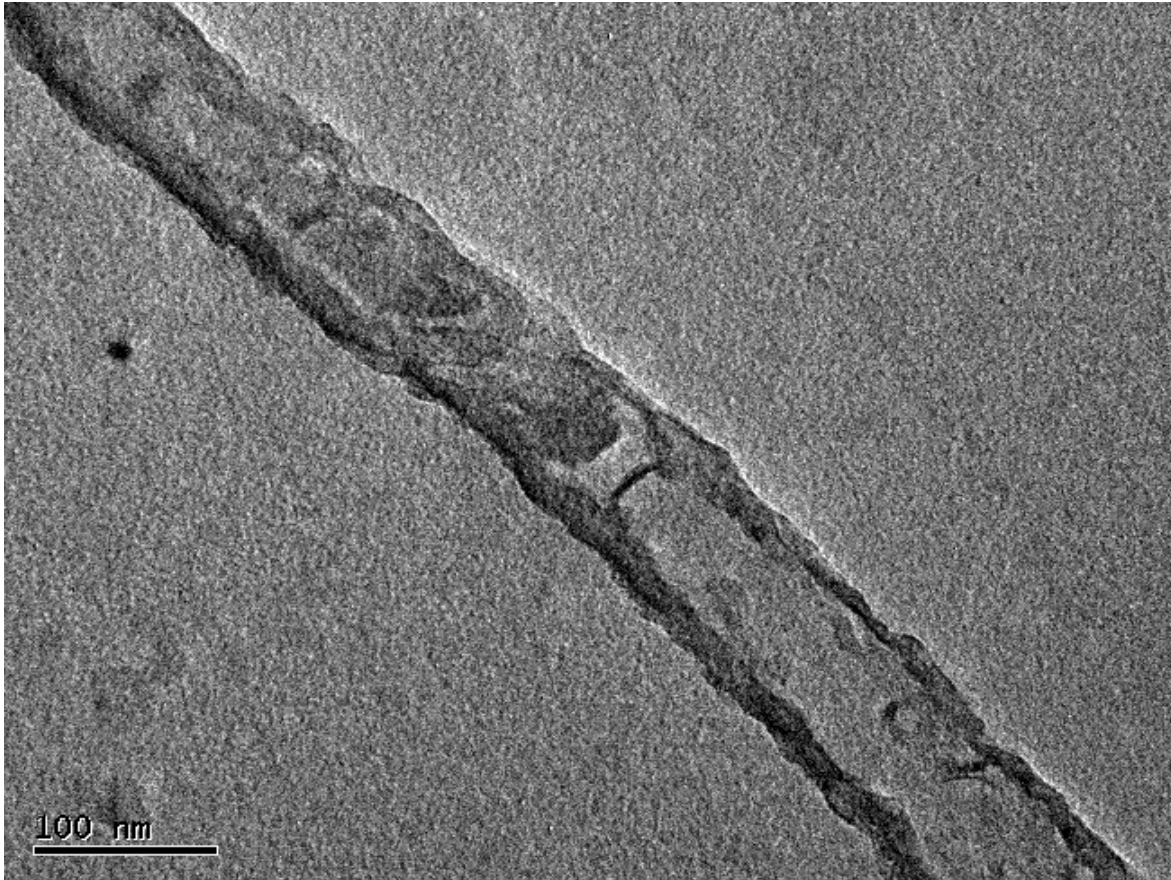


Figure 7.7 Transmission electron micrograph of a typical nanowire spin valve structure. In this set of samples, thickness of the Alq₃ layer is ~ 33 nm. For TEM characterization, the nanowires were released from the alumina host matrix by dissolution in dilute chromic-phosphoric acid. The solution (containing nanowires) was sonicated and centrifuged and the nanowires were collected on a TEM grid for imaging.

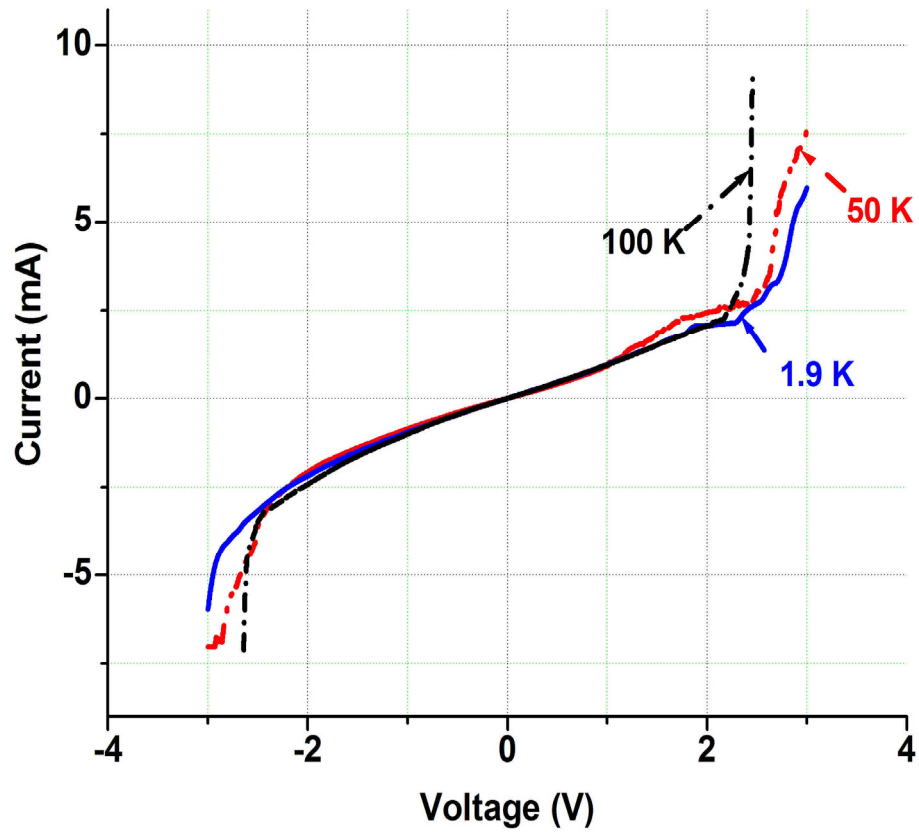


Figure 7.8 Current versus voltage characteristics of the trilayered spin-valve nanowires at three different temperatures

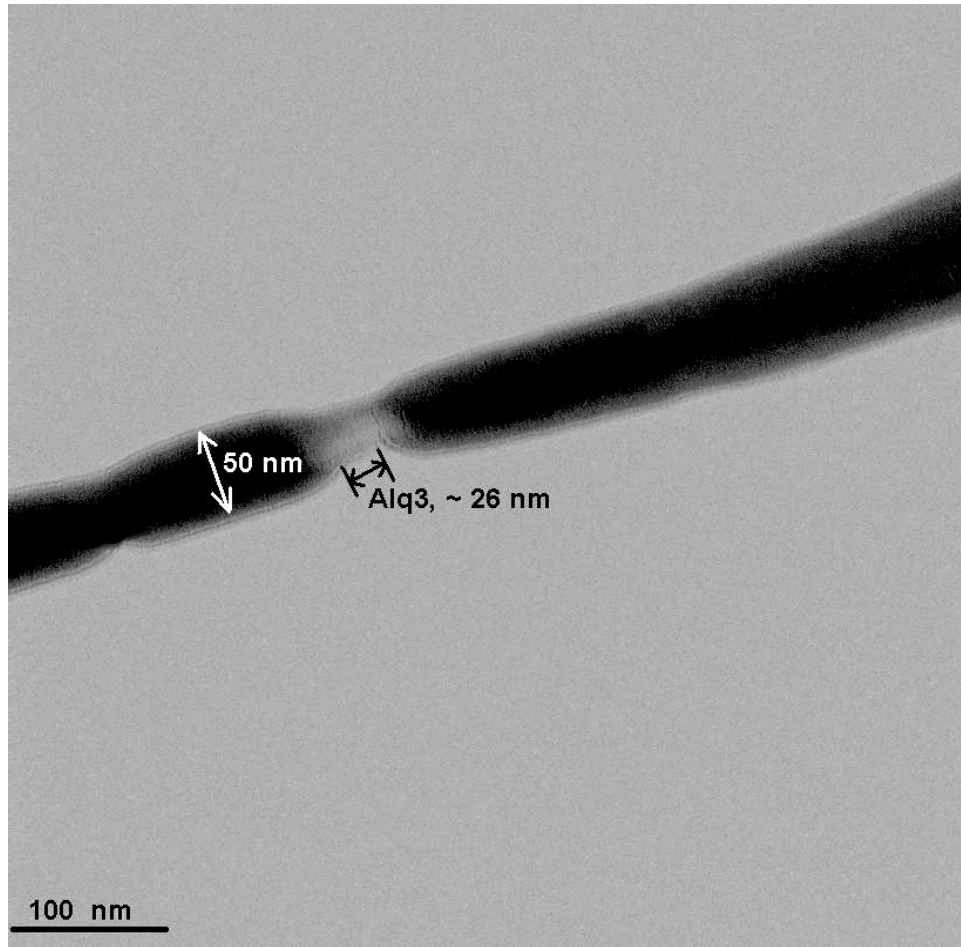


Figure 7.9 Transmission electron micrograph of a typical nanowire spin valve structure (2nd set of samples). In this set, thickness of the Alq₃ layer is ~ 26 nm.

$$\frac{\tau_m^{2D}}{\tau_m^{1D}} = \frac{\lambda_T^{2D}}{\lambda_T^{1D}} \quad (7.3)$$

where “2D” refers to thin film, and “1D” refers to nanowire. From Equation (7.3), we find

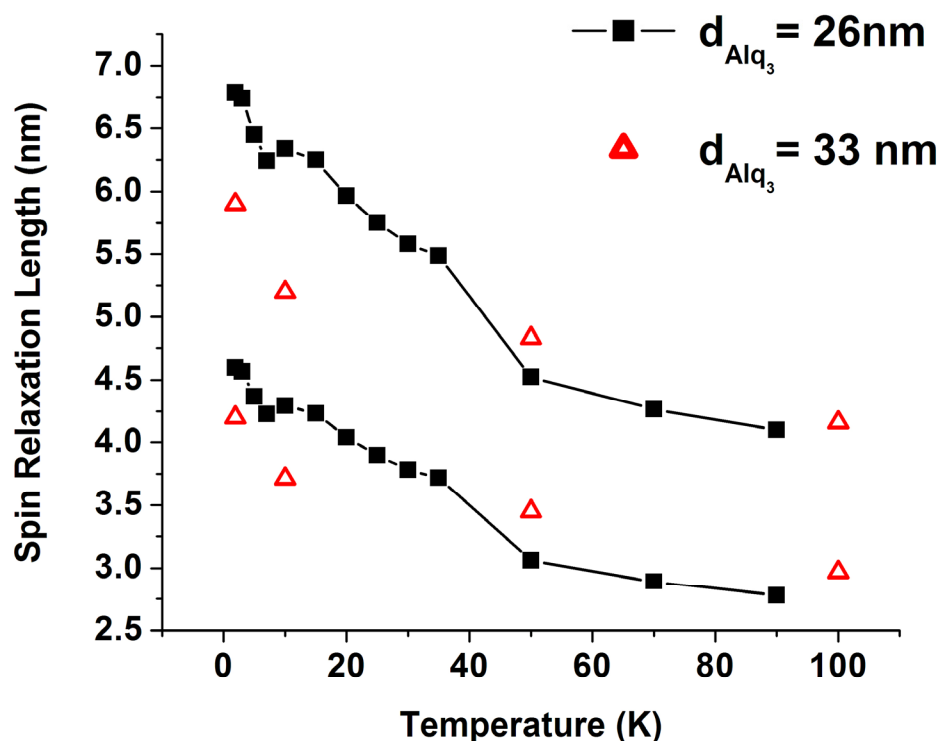


Figure 7.10 This figure plots spin relaxation length in Alq₃ nanowires as a function of temperature. The triangles are data obtained from the first set and the squares are data obtained from the second set. We show the maximum and minimum values at different temperatures. The non-zero range comes from +/- 5 nm uncertainty in the thickness of the organic layer.

that one-dimensional confinement has reduced τ_m by a factor of ~ 10 . This is possible in our structures. There is a huge density of charged surface states - of the order of $10^{13}/\text{cm}^2$ - at the interface between the nanowire and its ceramic host (alumina) [117]. These surface

states will cause frequent momentum randomizing collisions in the nanowire via Coulomb interaction, which will significantly reduce τ_m in these nanowires compared to thin films.

It is possible to estimate the temperature dependent spin relaxation *time* τ_s (T) from λ_T using the relation τ_s (T) = λ_T^2 / D (T) = $e \lambda_T^2 / k T \mu$, where μ is the drift mobility. The reported drift mobility in Alq₃ is given by the relation [152]:

$$\mu(E) = \mu_0 \exp[\alpha E^{1/2}] \quad (7.4)$$

where μ_0 and α are constants and E is the electric field. Reference [152] reports $\mu_0 = 10^{-7} - 10^{-9}$ cm²/V-sec, and $\alpha = 10^{-2}$ (cm/V)^{1/2} in the *bulk* organic.

In order to determine the electric field E in the organic, we proceed as follows. The voltage over the nanowires can be estimated from the measured resistance and the current using Ohm's law: $V = I \times R = 10 \mu\text{A} \times 1520 \Omega = 15.2$ mV. Since the Alq₃ layer (in the first set) is nominally 33 nm wide, the average electric field across it is 15.2 mV/33 nm = 4.6 kV/cm. Using this value in Equation (7.4), we estimate that the carrier mobility in the *bulk* organic is $2 \times 10^{-7} - 2 \times 10^{-9}$ cm²/V-sec. In nanowires, the mobility is 10 times lower since we found that the momentum relaxation time is 10 times smaller. Therefore, the mobility in these samples is $2 \times 10^{-8} - 2 \times 10^{-10}$ cm²/V-sec.

Assuming that the mobility is temperature independent, we have calculated the spin relaxation time τ_s (T) from the relation τ_s (T) = $e \lambda_T^2 / k T \mu$. These results are plotted as a function of temperature in Figure 7.11. The two curves give the maximum and minimum values of τ_s (T) at different temperatures. They range from few milliseconds to over 1 second at 1.9 K. These are among the longest spin relaxation times reported in any system.

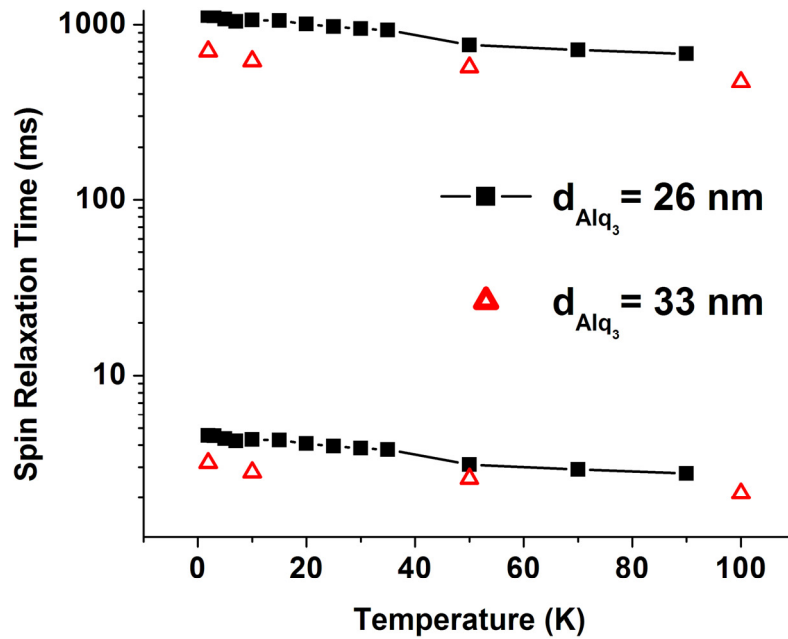


Figure 7.11 This figure plots spin relaxation time in Alq_3 nanowires as a function of temperature. The triangles are data obtained from the first set and the squares are data obtained from the second set. We show the maximum and minimum values at different temperatures. The non-zero range comes from the uncertainty in the mobility value of the organic layer.

Finally, in Figures 7.12 and 7.13, we plot the spin diffusion length and the spin relaxation time as a function of the electric field within the organic layer at a temperature of 1.9 K. Both quantities decrease with increasing field since the latter promotes momentum relaxing scattering events and therefore increases the spin relaxation rate.

One final question remains. What is the origin of negative (or inverted) spin valve peaks observed in Figures 7.5 and 7.6? If there are localized defects in the organic and carriers resonantly tunnel through them, then the spin polarization of the ferromagnetic contact

nearer to the defect can be effectively inverted (sign reversed) [150, 153]. In that case, P_1 and P_2 in equation (7.1) will have opposite signs implying $R_{AP} < R_P$. Here R_{AP} (and R_P) denotes the device resistance when the ferromagnetic contacts are magnetized anti-parallel (and parallel) to each other. This will produce a negative spin valve effect. In other words, the “peak” becomes a “trough”.

Thus the negative (inverted) spin valve peak (or the trough) is manifested when carriers resonantly tunnel through a localized defect state. This requires that the carrier energy is resonant with the impurity level. In some nanowires, this may happen and they exhibit a trough. In others, this does not happen so that they exhibit a peak, instead of a trough. Since each sample consists of a large number ($\sim 10^8$) of nanowires, there is some cancellation between the positive and negative signals which decreases the measured signal as a result of ensemble averaging. This is probably the reason why the distribution in Figure 7.3 peaks near zero.

We will now explain why a peak is accompanied by a positive background magnetoresistance and a trough is accompanied by a negative background magnetoresistance. At any magnetic field, except between the coercive fields of the two ferromagnets, the magnetizations of the injecting and detecting contacts are parallel. Assume also that both ferromagnets have the same sign of the spin polarization (as is indeed the case with cobalt and nickel). Now consider the case when the spin valve peak is positive, meaning that there is no resonant tunneling through impurity states resulting in an effective inversion of the spin polarization of the nearest contact. In this case, an injected carrier will transmit and contribute to current if its spin does not flip within the spacer

layer. In the presence of spin-orbit interaction, a magnetic field will increase the spin flip rate by inducing spin-mixing [37, 103]. Thus, the probability of spin flipping increases with increasing magnetic field. If the injected carrier's spin flips, then it will be blocked by the detecting contact and the current will decrease resulting an increase in resistance. Thus the resistance should increase with increasing magnetic field resulting in a *positive* background monotonic magnetoresistance. This is what we observe.

In the case of negative spin valve signal, resonant tunneling through an impurity state results in effective inversion of the spin polarization of the nearer ferromagnetic contact. In this case, spin flipping within the spacer layer will allow the flipped spin to transmit through the detector contact, which would have otherwise blocked it. Thus spin flip events decrease the device resistance, instead of increasing it. Since a magnetic field increases the spin flip rate, the resistance will decrease with increasing magnetic field, resulting in a negative monotonic background magnetoresistance. Again this is exactly what we observe. These mechanisms are illustrated in Figure 7.14.

Note that the above mechanism for the background monotonic magnetoresistance does not call for phase coherence of charge carriers and therefore can persist upto high temperatures. We believe that this is a more likely cause of the background monotonic magnetoresistance in organic spin valves than either localization or anti-localization. Of course, this mechanism requires correlation of the signs of the spin valve signal and the background magnetoresistance. If they turn out to be anti-correlated, then this will not be the cause. We have always observed this correlation, and never observed anti-correlation,

in all our experiments (90 samples, multiple traces). Therefore we believe the mechanism suggested here is indeed the likely cause.

In conclusion, we have demonstrated the first “quantum wire” organic spin valve, and in the process identified the dominant spin relaxation mechanism in organics to be the E-Y mode. We have also demonstrated that the spin relaxation time in organics is *exceptionally long* which is consistent with vanishingly small spin orbit interaction strength in organics. This establishes organic semiconductors as a very viable platform for spintronics. We also report an intriguing correlation between the sign of the spin valve signal and the background monotonic magnetoresistance. Based on this correlation, we have proposed a likely origin of the background magnetoresistance.

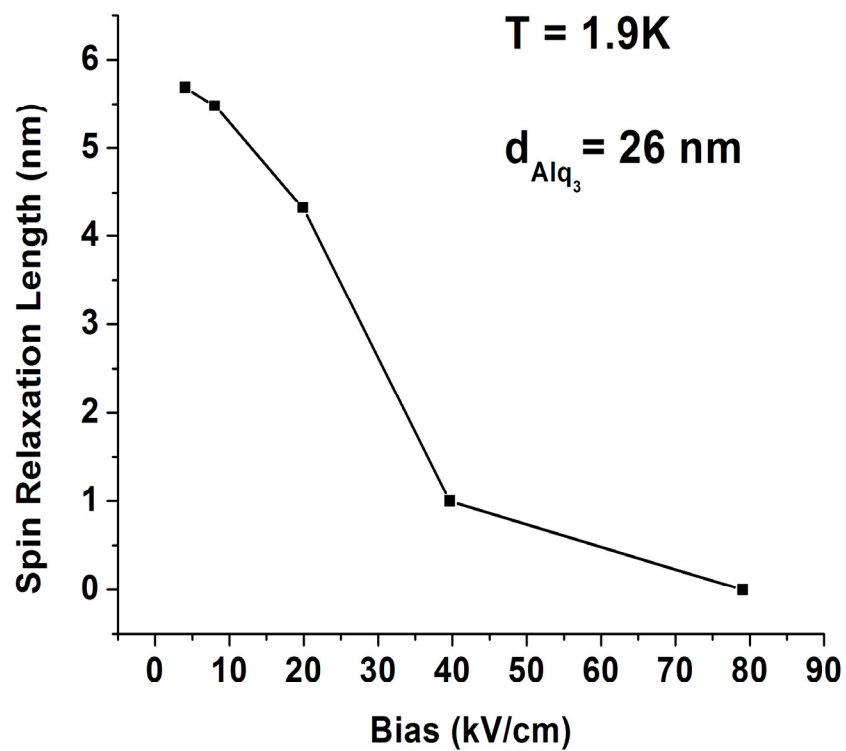


Figure 7.12 This figure plots spin relaxation length in Alq₃ nanowires as a function of applied bias at a fixed temperature of 1.9 K.

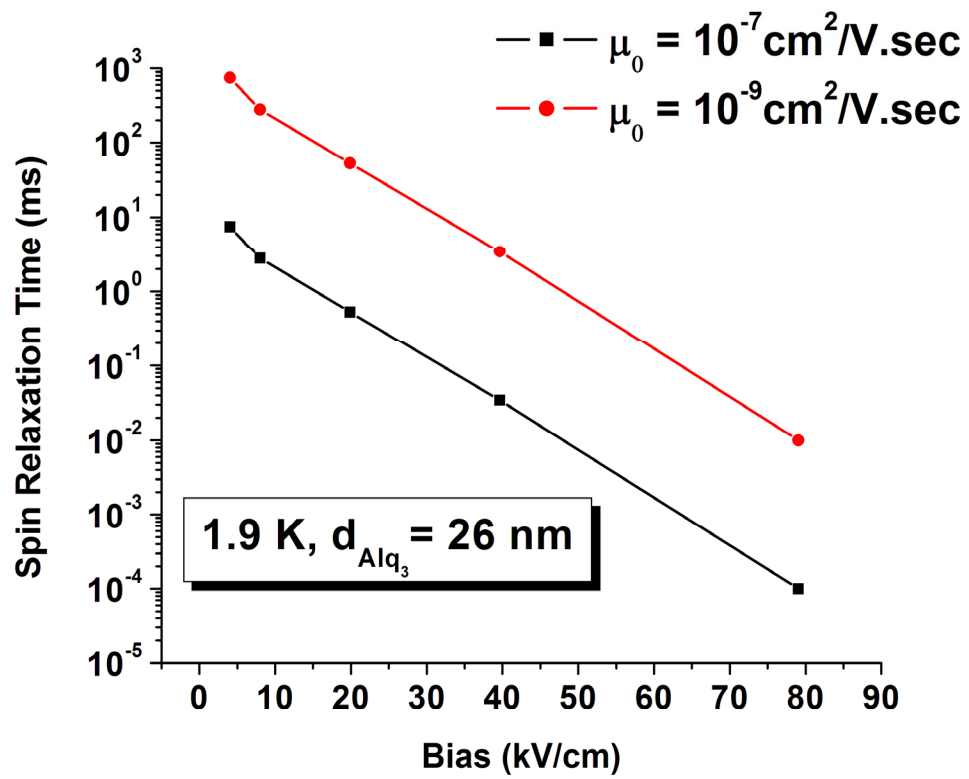
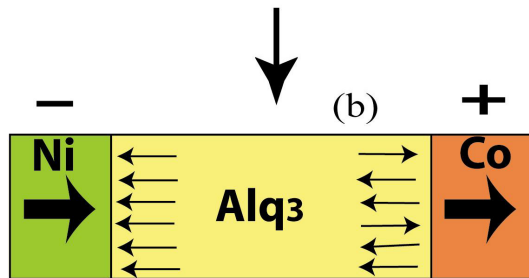


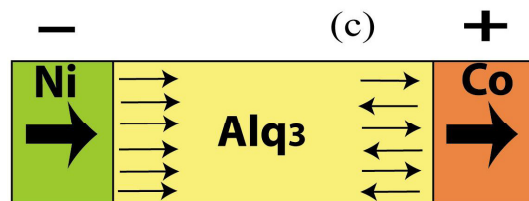
Figure 7.13 This figure plots spin relaxation time in Alq₃ nanowires as a function of applied bias at a fixed temperature of 1.9 K.



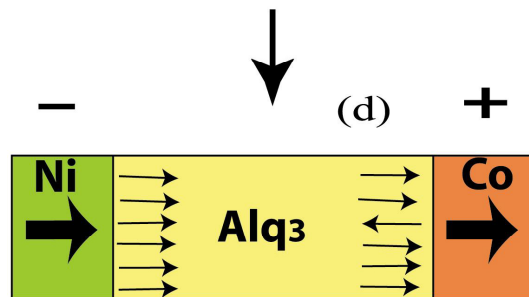
Consider the case when $H > |H_{Co}| > |H_{Ni}|$ and resonant inversion of injected spin polarization takes place at Ni/Alq₃ interface. Due to high magnetic field in the channel, injected spins are completely depolarized when they reach Co/Alq₃ interface. On an average, 50% of the injected spins are transmitted by the Co electrode and device resistance $R = R_1$ (say)



In this case, $H = 0^+$, and injection condition is as before. Partial spin depolarization takes place due to reduced magnetic field in the channel and on an average, $< 50\%$ of the injected spins are transmitted by the Co electrode. Thus device resistance $R = R_2 > R_1$. This explains the background negative magnetoresistance.



Again consider the situation when $H > |H_{Co}| > |H_{Ni}|$ but *no* resonant inversion occurs at Ni/Alq₃ interface. Due to high magnetic field in the channel, injected spins are completely depolarized when they reach Co/Alq₃ interface. On an average, 50% of the injected spins are transmitted by the Co electrode and device resistance $R = R_1'$



In this case, $H = 0^+$, and injection condition is as before. Partial spin depolarization takes place due to reduced magnetic field in the channel and on an average, $> 50\%$ of the injected spins are transmitted by the Co electrode. Thus device resistance $R = R_2' < R_1'$. This explains the background positive magnetoresistance.

Figure 7.14 Explanation of background negative (panels (a) and (b)) and positive (panels (c) and (d)) magnetoresistance. We have assumed for simplicity that Ni is a 100% spin injector. Though this assumption is not true, it does not affect the conclusions.

CHAPTER 8. Transverse Spin Relaxation Times in an Ensemble of Electrochemically Self-assembled CdS Quantum Dots*

Overview

Using electron spin resonance (ESR) experiments, we have measured the ensemble transverse relaxation time (T_2^*) of spins in arrays of cadmium sulfide (CdS) quantum dots self-assembled by selective electrodeposition of the compound in 10 nm diameter pores of an anodic alumina film. The T_2^* time is very short – a few nanoseconds at low temperatures – and it *increases* with increasing temperature in the range 3.7 K – 20 K. The major source of dephasing contributing to the relaxation rate is believed to be spatially varying hyperfine interactions with nuclear spins. The temperature dependence is consistent with the nuclear magnetic field being increasingly depolarized at higher temperatures leading to a progressively weaker hyperfine interaction. The effective Lande' g factor in the quantum dots was found to be ~ 2 .

* This chapter has been published in the Proceedings of 6th IEEE conference on Nanotechnology (IEEE-Nano), Cincinnati, 2006. (Authors: S. Pramanik, B. Kanchibotla, and S. Bandyopadhyay)

8.1 Introduction

There is significant interest in studying spin coherence lifetimes in semiconductor quantum dots [69] because of potential applications in spin based quantum computing. The spin of a single electron in a quantum dot has often been considered a suitable entity to encode a *qubit* because spin coherence times can vastly exceed charge coherence times [154]. Consequently, spin based quantum computers are expected to be more robust and fault-tolerant than charge based quantum computers.

Interest in quantum processors, particularly fault tolerant logic gates, has motivated the study of spin coherence in quantum dots. The study of spin lifetimes in semiconductors dates back to almost 40 years. There are two types of spin lifetimes that are of interest. The first is the so-called longitudinal relaxation time, or T_1 time, which essentially refers to the mean time that elapses before an excited spin flips to the ground state. This time is of great importance in classical spin-based logic gates [16] but less relevant to quantum computing where what matters is how rapidly a single spin loses its quantum mechanical phase coherence. That time is determined by the transverse relaxation time, or T_2 time. The definition of the T_2 time invariably involves a concept of quantum superposition. A qubit is a coherent superposition of “upspin” and “downspin” states, as expressed by the following equation:

$$\text{qubit} = a|\uparrow\rangle + b|\downarrow\rangle \quad (8.1)$$

where a and b are complex quantities with a definite phase relationship between them. Also, the norm of this state is unity (i.e. $|a|^2 + |b|^2 = 1$). In order to preserve the coherence between the upspin and downspin states, one needs to maintain the precise phase

relationship between the complex coefficients a and b . The time constant associated with the temporal decay of this phase relation is the T_2 time. Accordingly, T_2 provides a measure of the robustness of a qubit.

It is difficult to measure the T_2 time directly since we have to probe decoherence of a *single* electron. In most experiments, one probes a large number of spins simultaneously. Even if these spins do not interact with each other, inhomogeneities in local magnetic fields caused by nuclear spins having random polarization, or spatially varying spin-orbit interaction, will increase the decoherence rate substantially. Therefore what one measures will always be less than the actual T_2 time associated with a *single* electron. We call this measured time the T_2^* time. It has been shown that T_2^* can be several times smaller than T_2 [62].

There are many ways of measuring T_2^* in quantum dots. For example reference [66] has used femtosecond - resolved Faraday rotation technique to study T_2^* lifetime in chemically synthesized CdSe quantum dots with diameters varying in the range 2 – 8 nm. They reported spin lifetime of ~ 3 nanoseconds at zero magnetic field, which reduces to ~ 100 picoseconds at an applied magnetic field of 4 T. The g factor is in the range of 1.1 – 1.7. In these systems, T_2^* is independent of temperature in the range 6 – 282 K. References [67, 68] report T_2^* time of ~ 6 nanoseconds in GaAs quantum dots. Hanle effect measurements [65] show that T_2^* is approximately 0.2 nanoseconds in case of self-assembled InAs quantum dots. The nuclear spin of Indium is 9/2 and this is probably the reason why T_2^* is shorter for InAs quantum dots as compared to GaAs or CdSe quantum dots. In the present

work we use electron spin resonance (ESR) technique to determine T_2^* and the g factor of CdS quantum dots.

This ESR technique is quite straightforward. The quantum dots are subjected to a dc magnetic field which lifts the degeneracy of the spin states. This is the well known Zeeman splitting. Next, an ac magnetic field produced by a microwave source, is applied over the spins. It induces Rabi oscillations between the Zeeman-split levels when the microwave frequency is resonant with the spin-splitting energy. Consequently, microwave is absorbed when resonance occurs. From the linewidth of the absorption peak, we can deduce T_2^* . Also from the value of resonance frequency (equivalently, the value of dc magnetic field at which resonance occurs, when microwave frequency is kept constant) we can deduce the g factor of the electrons in the quantum dots.

Although this is a straightforward technique, it has been seldom applied to quantum dots since the absorption intensity depends on the number of participating spins and that number has to be large in order to produce a strong enough signal. With quantum dots, the number of spins involved is typically small so that normal ESR is not a reliable method. However, if the density of the quantum dots is sufficiently high, then it may be possible to obtain a strong enough ESR signal (particularly at low temperatures when level broadening is small) to yield a reliable estimate of T_2^* time. Since we can produce an extremely dense array of quantum dots (density $> 10^{11}/\text{cm}^2$) using electrochemical self-assembly, we have used ESR, successfully, to measure the T_2^* time.

8.2 Sample fabrication procedure

The electrochemical self-assembly technique for fabricating quantum-confined structures has been discussed in details in the previous chapters. Here we will reiterate the basic steps of the fabrication process. This process is schematically shown in Figure 8.1.

We first electropolish and then anodize an aluminum foil in 15% sulfuric acid using a constant voltage of 10V dc to produce a porous alumina film on the substrate. The pore diameter is 10 nm with 10% standard deviation [118]. A SEM micrograph of the anodized template is shown in Figure 8.2.

The pores are then selectively filled with CdS using ac electrodeposition in a non-aqueous solution of dimethyl sulfoxide comprising cadmium perchlorate, lithium perchlorate and sulfur powder. Electrodeposition is carried out at 100°C with an rms voltage of 20V and 250 Hz frequency. In the end, we have an ordered array of cylindrical CdS quantum dots, each with a diameter of 10 nm, and heights ranging from 10 – 100 nm, hosted in an alumina matrix.

The alumina film is released from its aluminum substrate by dissolution in HgCl_2 solution which does not affect the alumina or CdS, but dissolves away the aluminum. Several such films (~ 20) are then stacked in the sample chamber of a Bruker BioSpin ESR spectrometer in order to acquire a signal of sufficient strength. Signal is obtained from $\sim 10^{11}$ dots. Spin resonance measurements are carried out over a temperature range extending from 3.7 K to 20 K. Above 20 K, the strength of the ESR signal fades and falls below the equipment's sensitivity.

8.3 Experimental results

In Figure 8.3, we show the first derivative of the ESR linewidth as a function of (dc) magnetic field at four different temperatures. The microwave frequency is fixed at 9.35 GHz and the dc magnetic field is varied to reach resonance. The center field for the ESR resonance peak is found from Figure 8.3 to be 3310 Gauss. From this value we can find the Lande' g factor using the formula $\hbar(2\pi f) = g\mu_B B_c$ where f is the microwave frequency, $\hbar = h/2\pi$ is the reduced Planck constant, μ_B is Bohr magneton, and B_c is the flux density of the center field (i.e. 3310 Gauss). Putting $f = 9.35$ GHz and $B_c = 3310$ Gauss, we get $g = 2.0$. This measurement yields the magnitude of the g factor but not its sign. It is interesting to note that an electron in these quantum dots have, on the average, the same g factor as a free electron. From Figure 8.3, we can find the T_2^* time at different temperatures. We used very low microwave power ($\sim \mu$ W) in order to avoid sample saturation. At this power level, $T_1 \sim 100\mu$ s and the ESR linewidth is determined by

T_2^* . The lineshape resembles a Lorentzian. In that case T_2^* is given by $T_2^* = \frac{1}{\gamma_e \sqrt{3} (\Delta B_{pp})}$

where γ_e is the electronic magnetogyric ratio (1.76×10^7 G⁻¹s⁻¹), and ΔB_{pp} is the separation between the positive and negative peaks in Figure 8.3 which is basically the full-width-at-half-maximum of the ESR lineshape, scaled down by a factor of $\sqrt{3}$ (due to Lorentzian shape of the absorption curve).

In Figure 8.4, we plot T_2^* time as a function of temperature. Clearly the transverse relaxation time increases monotonically with temperature at least in the temperature range (3.7 K, 20 K). This is very counterintuitive, because in case of bulk, quantum well, or,

quantum wires, spin dephases at a faster rate as we increase temperature. But, surprisingly, for quantum dots, we observe an opposite effect. Here spin dephasing process is slowed down as we increase temperature. In order to understand this effect let us take a close look at the various spin dephasing mechanisms that are operative in quantum dots.

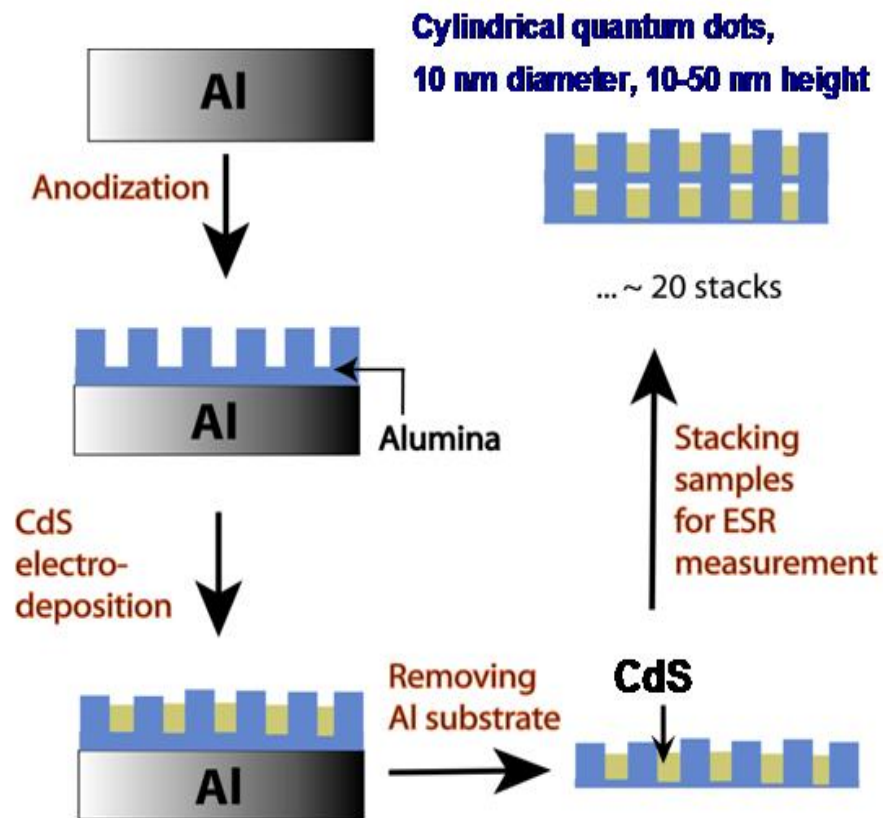


Figure 8.1 Schematic description of the sample fabrication process

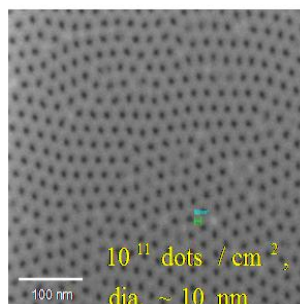


Figure 8.2 A SEM micrograph of nanoporous template with nominal pore diameter of 10 nm. The areal density of the pores is approximately $10^{11}/\text{cm}^2$

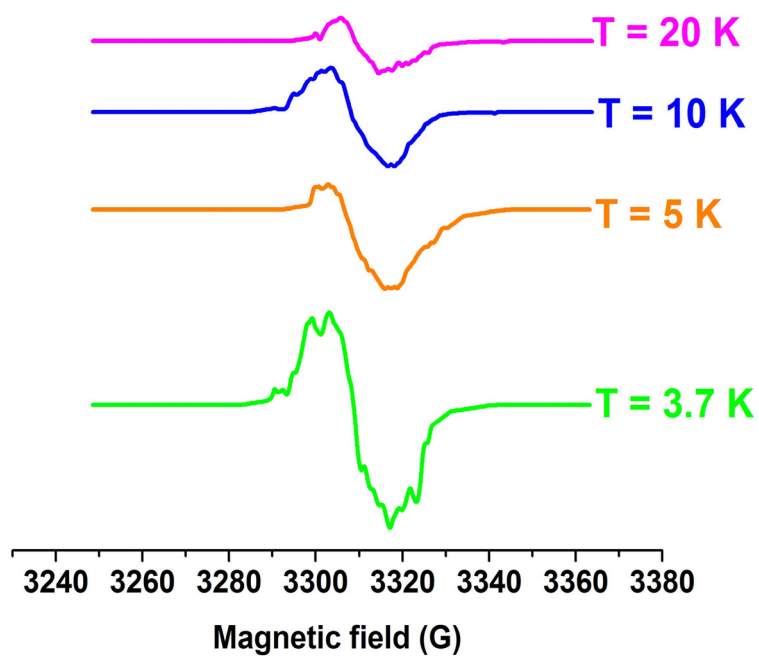


Figure 8.3 First derivative of the ESR linewidth as a function of magnetic flux density at four different temperatures. Note that the distance between the two peaks decreases slowly as we increase temperature. The vertical axis is in arbitrary units and the four spectra are shifted vertically for easy comparison.

8.4 Discussion

There are several mechanisms that can cause electron spin dephasing in quantum dots. First of all, there is ubiquitous spin-orbit interaction accruing from various sources. For a comprehensive discussion on this topic the reader is encouraged to go through reference [49]. However, in case of quantum dots, spin-orbit interaction is extremely weak since the electron is strongly localized in space i.e. its motion is restricted in all three dimensions [49, 51]. Typical time scale of spin dephasing due to spin-orbit interaction alone is \sim few milliseconds [49]. Thus spin-orbit interaction is not the dominant source of spin dephasing at least for quantum dots. It is widely believed that the primary cause of spin dephasing in an ensemble of quantum dots is the spatially varying hyperfine interaction caused by nuclear spins. The spatial variation comes about from two sources. First, the electronic wavefunction varies in space and the strength of the hyperfine interaction depends on this wavefunction. Second, the magnetic field due to nuclear spins is also inhomogeneous. This inhomogeneity is the major contributor to the dephasing rate $1/T_2^*$. In quantum wells, on the other hand, the major spin dephasing mechanism is believed to be Rashba spin-orbit interaction. That interaction, however, is extremely weak in quantum dots since the electron motion is restricted in all three dimensions [51]. Also dipole-dipole interaction between nuclear spins causes the net nuclear field to change with time. This change in net nuclear magnetic field can cause electron spin dephasing. But this process occurs on a much longer time scale. For example in case of GaAs, typical timescale associated with this process is $\sim 100 \mu\text{s}$ (obtained from the linewidth of NMR absorption spectrum). Thus this process is not very effective in dephasing electron spins.

Reference [57] provides an equation for the transverse relaxation rate in the special case of electrons hopping between dots

$$\frac{1}{T_2} = \frac{1}{2T_1} + \frac{(g\mu_B)^2}{2\hbar^2} \int_{-\infty}^{\infty} \langle H_{NZ}(0)H_{NZ}(\tau) \rangle d\tau$$

where the bracket $\langle \dots \rangle$ denotes ensemble average and H_{NZ} is the effective magnetic field due to nuclear spins. Obviously, the dephasing rate increases with increasing autocorrelation given by the integral in the above equation. With increasing temperature, the nuclear spin polarizations are randomized leading to a decrease in the autocorrelation function. This explains why the dephasing rate decreases with increasing temperature as shown in Figure 8.4.

The thermal depolarization of nuclear spins also plays a direct role in electron spin dephasing. As we discussed in Chapter 1, for an unpolarized configuration of nuclear spins, the net magnetic field is reduced by a factor \sqrt{N} , where N is the total number of nuclear spins interacting with the electron. Since hyperfine interaction gets weaker at higher temperature, electron spin dephasing rate decreases. Using the theory of reference [59], we indeed obtain $T_2^* \sim 2$ ns, which is in excellent agreement with our experimental finding.

8.5 Conclusion

In conclusion, we have measured the ensemble transverse spin relaxation time T_2^* in an array of 10^{11} quantum dots using ESR. The relaxation time increases with temperature which is consistent with hyperfine interaction due to nuclear spins being the primary cause

of spin dephasing. The measured time is very short, of the order of few nanoseconds, which agrees with previously published experimental data and theoretical model.

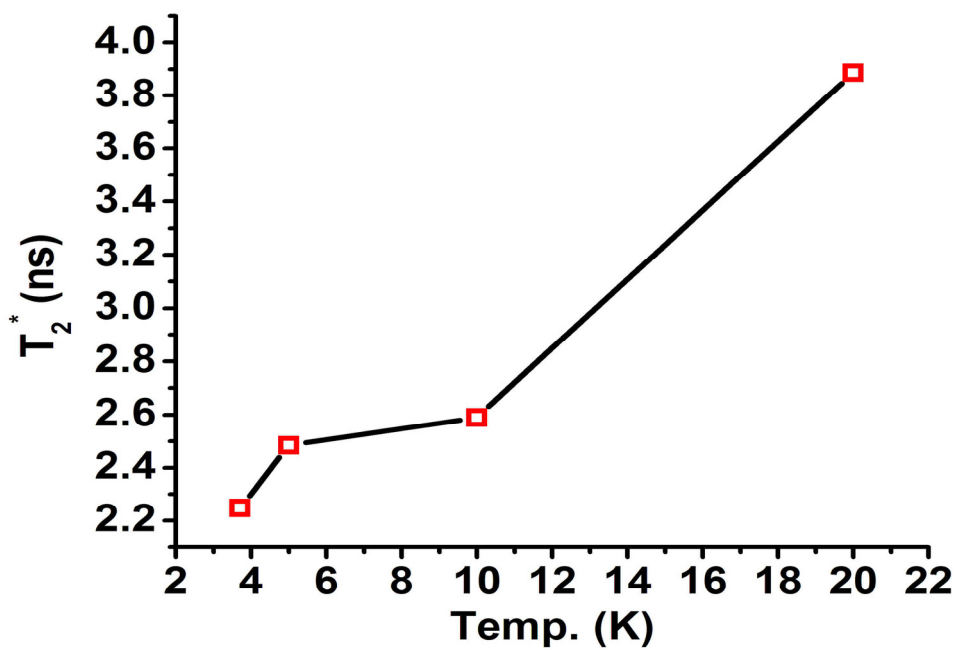


Figure 8.4 The measured T_2^* time as a function of temperature

BIBLIOGRAPHY

- [1] M. Cahay and S. Bandyopadhyay, "Spintronics," *IEE Proceedings - Circuits, Devices and Systems*, vol. 152, pp. 293-296, 2005.
- [2] D. D. Awschalom, M. E. Flatte, and N. Samarth, "Spintronics," *Scientific American*, vol. 286, pp. 66-73, 2002.
- [3] S. A. Wolf and D. M. Treger, "Special issue on spintronics," *Proceedings of the IEEE*, vol. 91, pp. 647-651, 2003.
- [4] C. H. Tsang, R. E. Fontana, T. Lin, D. E. Heim, B. A. Gurney, and M. L. Williams, "Design, fabrication, and performance of spin-valve read heads for magnetic recording applications," *IBM Journal of Research and Development*, vol. 42, pp. 103-116, 1998.
- [5] E. Grochowski, "Emerging trends in data storage on magnetic hard disk drives," *Datatech*, pp. 11-16, 1998.
- [6] M. N. Baibich, J. M. Broto, A. Fert, F. N. Vandau, F. Petroff, P. Eitenne, G. Creuzet, A. Friederich, and J. Chazelas, "Giant magnetoresistance of (001)Fe/(001)Cr magnetic superlattices," *Physical Review Letters*, vol. 61, pp. 2472-2475, 1988.
- [7] G. Binasch, P. Grunberg, F. Saurenbach, and W. Zinn, "Enhanced magnetoresistance in layered magnetic-structures with antiferromagnetic interlayer exchange," *Physical Review B*, vol. 39, pp. 4828-4830, 1989.
- [8] J. F. Gregg, I. Petej, E. Jouguelet, and C. Dennis, "Spin electronics - a review," *Journal of Physics D - Applied Physics*, vol. 35, pp. R121-R155, 2002.
- [9] S. Datta and B. Das, "Electronic analog of the electro-optic modulator," *Applied Physics Letters*, vol. 56, pp. 665-667, 1990.
- [10] S. Bandyopadhyay and M. Cahay, "Alternate spintronic analog of the electro-optic modulator," *Applied Physics Letters*, vol. 85, pp. 1814-1816, 2004.

- [11] J. Fabian, I. Zutic, and S. Das Sarma, "Magnetic bipolar transistor," *Applied Physics Letters*, vol. 84, pp. 85-87, 2004.
- [12] M. E. Flatte, Z. G. Yu, E. Johnston-Halperin, and D. D. Awschalom, "Theory of semiconductor magnetic bipolar transistors," *Applied Physics Letters*, vol. 82, pp. 4740-4742, 2003.
- [13] M. E. Flatte and G. Vignale, "Unipolar spin diodes and transistors," *Applied Physics Letters*, vol. 78, pp. 1273-1275, 2001.
- [14] M. E. Flatte and G. Vignale, "Heterostructure unipolar spin transistors," *Journal of Applied Physics*, vol. 97, pp. 104508, 2005.
- [15] S. Bandyopadhyay and M. Cahay, "Re-examination of some spintronic field-effect device concepts," *Applied Physics Letters*, vol. 85, pp. 1433-1435, 2004.
- [16] S. Bandyopadhyay, B. Das, and A. E. Miller, "Supercomputing with spin-polarized single electrons in a quantum coupled architecture," *Nanotechnology*, vol. 5, pp. 113-133, 1994.
- [17] N. J. Wu, N. Shibata, and Y. Amemiya, "Boltzmann machine neuron device using quantum-coupled single electrons," *Applied Physics Letters*, vol. 72, pp. 3214-3216, 1998.
- [18] S. Bandyopadhyay and V. P. Roychowdhury, "Switching in a reversible spin logic gate," *Superlattices and Microstructures*, vol. 22, pp. 411-416, 1997.
- [19] D. Loss and D. P. DiVincenzo, "Quantum computation with quantum dots," *Physical Review A*, vol. 57, pp. 120-126, 1998.
- [20] D. Bohm, *The Special Theory of Relativity*. New York: W. A. Benjamin, Inc., 1965.
- [21] H. Kroemer, "The Thomas precession factor in spin-orbit interaction," *American Journal of Physics*, vol. 72, pp. 51-52, 2004.

- [22] M. Jammer, *The Conceptual Development of Quantum Mechanics*. New York: McGraw Hill, 1966.
- [23] L. H. Thomas, "The motion of the spinning electron," *Nature*, vol. 117, pp. 514, 1926.
- [24] C. Kittel, *Quantum Theory of Solids*. New York: John Wiley & Sons, Inc., 1963.
- [25] R. Shankar, *Principles of Quantum Mechanics*, 2nd ed: Springer, 1994.
- [26] G. Dresselhaus, "Spin-orbit coupling effects in zinc blende structures," *Physical Review*, vol. 100, pp. 580-586, 1955.
- [27] A. M. Bychkov, L. A. Openov, and I. A. Semenihih, "Single-electron computing without dissipation," *JETP Letters*, vol. 66, pp. 298-303, 1997.
- [28] Y. A. Bychkov and E. I. Rashba, "Oscillatory effects and the magnetic-susceptibility of carriers in inversion-layers," *Journal of Physics C - Solid State Physics*, vol. 17, pp. 6039-6045, 1984.
- [29] I. Zutic, J. Fabian, and S. Das Sarma, "Spintronics: Fundamentals and applications," *Reviews of Modern Physics*, vol. 76, pp. 323-410, 2004.
- [30] R. J. Elliott, "Theory of the effect of spin-orbit coupling on magnetic resonance in some semiconductors," *Physical Review*, vol. 96, pp. 266-279, 1954.
- [31] Y. Yafet, *Solid State Physics*, vol. 14: Academic Press, 1963.
- [32] M. I. D'yakonov and V. I. Perel', "Spin orientation of electrons associated with the interband absorption of light in semiconductors," *Soviet Physics - JETP*, vol. 33, pp. 1053-1059, 1971.
- [33] M. I. D'yakonov and V. I. Perel', "Spin relaxation of conduction electrons in non-centrosymmetric semiconductors," *Soviet Physics - Solid State*, vol. 13, pp. 3023-3026, 1972.

- [34] G. L. Bir, A. G. Aronov, and G. E. Pikus, *Soviet Physics - JETP*, vol. 42, pp. 705, 1976.
- [35] A. Abragam, *The Principles of Nuclear Magnetism*. London: Oxford University Press, 1973.
- [36] H. Sakaki, "Scattering suppression and high-mobility effect of size-quantized electrons in ultrafine semiconductor wire Structures," *Japanese Journal of Applied Physics*, vol. 19, pp. L735-L738, 1980.
- [37] M. Cahay and S. Bandyopadhyay, "Phase-coherent quantum mechanical spin transport in a weakly disordered quasi-one-dimensional channel," *Physical Review B*, vol. 69, pp. 045303, 2004.
- [38] S. Saikin, "A drift-diffusion model for spin-polarized transport in a two-dimensional non-degenerate electron gas controlled by spin-orbit interaction," *Journal of Physics - Condensed Matter*, vol. 16, pp. 5071-5081, 2004.
- [39] Z. G. Yu and M. E. Flatte, "Spin diffusion and injection in semiconductor structures: Electric field effects," *Physical Review B*, vol. 66, pp. 235302-1--235302-14, 2002.
- [40] Z. G. Yu and M. E. Flatte, "Electric-field dependent spin diffusion and spin injection into semiconductors," *Physical Review B*, vol. 66, pp. 201202-1--201202-4, 2002.
- [41] M. Q. Weng and M. W. Wu, "Kinetic theory of spin transport in n-type semiconductor quantum wells," *Journal of Applied Physics*, vol. 93, pp. 410-420, 2003.
- [42] A. Bournel, V. Delmouly, P. Dollfus, G. Tremblay, and P. Hesto, "Theoretical and experimental considerations on the spin field effect transistor," *Physica E*, vol. 10, pp. 86-90, 2001.
- [43] A. Bournel, P. Dollfus, P. Bruno, and P. Hesto, "Gate-induced spin precession in an In_{0.53}Ga_{0.47}As two dimensional electron gas," *European Physical Journal - Applied Physics*, vol. 4, pp. 1-4, 1998.

- [44] A. Bournel, P. Dollfus, E. Cassan, and P. Hesto, "Monte Carlo study of spin relaxation in AlGaAs/GaAs quantum wells," *Applied Physics Letters*, vol. 77, pp. 2346-2348, 2000.
- [45] A. Bournel, P. Dollfus, S. Galdin, F. X. Musalem, and P. Hesto, "Modeling of gate-induced spin precession in a striped channel high electron mobility transistor," *Solid State Communications*, vol. 104, pp. 85-89, 1997.
- [46] S. Pramanik, S. Bandyopadhyay, and M. Cahay, "Spin dephasing in quantum wires," *Physical Review B*, vol. 68, pp. 075313-1--075313-10, 2003.
- [47] S. Pramanik, S. Bandyopadhyay, and M. Cahay, "Decay of spin-polarized hot carrier current in a quasi-one-dimensional spin-valve structure," *Applied Physics Letters*, vol. 84, pp. 266-268, 2004.
- [48] S. Saikin, M. Shen, M. C. Cheng, and V. Privman, "Semiclassical Monte Carlo model for in-plane transport of spin-polarized electrons in III-V heterostructures," *Journal of Applied Physics*, vol. 94, pp. 1769-1775, 2003.
- [49] A. V. Khaetskii and Y. V. Nazarov, "Spin relaxation in semiconductor quantum dots," *Physical Review B*, vol. 61, pp. 12639-12642, 2000.
- [50] A. V. Khaetskii and Y. V. Nazarov, "Spin-flip transitions between Zeeman sublevels in semiconductor quantum dots," *Physical Review B*, vol. 64, pp. 125316, 2001.
- [51] S. Bandyopadhyay and M. Cahay, "Rashba effect in an asymmetric quantum dot in a magnetic field," *Superlattices and Microstructures*, vol. 32, pp. 171-177, 2002.
- [52] V. Privman, I. D. Vagner, and G. Kventsel, "Quantum computation in quantum-Hall systems," *Physics Letters A*, vol. 239, pp. 141-146, 1998.
- [53] B. E. Kane, "A silicon-based nuclear spin quantum computer," *Nature*, vol. 393, pp. 133-137, 1998.
- [54] S. Bandyopadhyay, "Self-assembled nanoelectronic quantum computer based on the Rashba effect in quantum dots," *Physical Review B*, vol. 61, pp. 13813-13820, 2000.

- [55] T. Calarco, A. Datta, P. Fedichev, E. Pazy, and P. Zoller, "Spin-based all-optical quantum computation with quantum dots: Understanding and suppressing decoherence," *Physical Review A*, vol. 68, pp. 012310, 2003.
- [56] D. P. DiVincenzo and D. Loss, "Quantum information is physical," *Superlattices and Microstructures*, vol. 23, pp. 419-432, 1998.
- [57] A. Khaetskii, D. Loss, and L. Glazman, "Electron spin evolution induced by interaction with nuclei in a quantum dot," *Physical Review B*, vol. 67, pp. 195329, 2003.
- [58] Y. G. Semenov and K. W. Kim, "Effect of an external magnetic field on electron-spin dephasing induced by hyperfine interaction in quantum dots," *Physical Review B*, vol. 67, pp. 073301, 2003.
- [59] I. A. Merkulov, A. L. Efros, and M. Rosen, "Electron spin relaxation by nuclei in semiconductor quantum dots," *Physical Review B*, vol. 65, pp. 205309, 2002.
- [60] W. A. Coish and D. Loss, "Hyperfine interaction in a quantum dot: Non-Markovian electron spin dynamics," *Physical Review B*, vol. 70, pp. 195340, 2004.
- [61] A. V. Khaetskii, D. Loss, and L. Glazman, "Electron spin decoherence in quantum dots due to interaction with nuclei," *Physical Review Letters*, vol. 88, pp. 186802, 2002.
- [62] R. de Sousa and S. Das Sarma, "Electron spin coherence in semiconductors: Considerations for a spin-based solid-state quantum computer architecture," *Physical Review B*, vol. 67, pp. 033301, 2003.
- [63] Y. V. Pershin and V. Privman, "Spin relaxation of conduction electrons in semiconductors due to interaction with nuclear spins," *Nano Letters*, vol. 3, pp. 695-700, 2003.
- [64] A. Greilich, D. R. Yakovlev, A. Shabaev, A. L. Efros, I. A. Yugova, R. Oulton, V. Stavarache, D. Reuter, A. Wieck, and M. Bayer, "Mode locking of electron spin coherences in singly charged quantum dots," *Science*, vol. 313, pp. 341-345, 2006.

- [65] R. J. Epstein, D. T. Fuchs, W. V. Schoenfeld, P. M. Petroff, and D. D. Awschalom, "Hanle effect measurements of spin lifetimes in InAs self-assembled quantum dots," *Applied Physics Letters*, vol. 78, pp. 733-735, 2001.
- [66] J. A. Gupta, D. D. Awschalom, X. Peng, and A. P. Alivisatos, "Spin coherence in semiconductor quantum dots," *Physical Review B*, vol. 59, pp. R10421-R10424, 1999.
- [67] A. S. Bracker, E. A. Stinaff, D. Gammon, M. E. Ware, J. G. Tischler, A. Shabaev, A. L. Efros, D. Park, D. Gershoni, V. L. Korenev, and I. A. Merkulov, "Optical pumping of the electronic and nuclear spin of single charge-tunable quantum dots," *Physical Review Letters*, vol. 94, 2005.
- [68] M. V. G. Dutt, J. Cheng, B. Li, X. D. Xu, X. Q. Li, P. R. Berman, D. G. Steel, A. S. Bracker, D. Gammon, S. E. Economou, R. B. Liu, and L. J. Sham, "Stimulated and spontaneous optical generation of electron spin coherence in charged GaAs quantum dots," *Physical Review Letters*, vol. 94, 2005.
- [69] J. Schliemann, A. Khaetskii, and D. Loss, "Electron spin dynamics in quantum dots and related nanostructures due to hyperfine interaction with nuclei," *Journal of Physics - Condensed Matter*, vol. 15, pp. R1809-R1833, 2003.
- [70] V. G. Fleisher and I. A. Merkulov, *Optical Orientation*. North Holland-Amsterdam, 1984.
- [71] S. Pramanik, S. Bandyopadhyay, and M. Cahay, "Spin relaxation in the channel of a spin field-effect transistor," *IEEE Transactions on Nanotechnology*, vol. 4, pp. 2-7, 2005.
- [72] S. Pramanik, S. Bandyopadhyay, and M. Cahay, "The inequality of charge and spin diffusion coefficients," *submitted (2006)*.
- [73] J. Sinova, D. Culcer, Q. Niu, N. A. Sinitsyn, T. Jungwirth, and A. H. MacDonald, "Universal intrinsic spin Hall effect," *Physical Review Letters*, vol. 92, 2004.
- [74] B. A. Bernevig and S. Zhang, "Toward dissipationless spin transport in semiconductors," *IBM Journal of Research and Development*, vol. 50, pp. 141-148, 2006.

- [75] E. G. Mishchenko, A. V. Shytov, and B. I. Halperin, "Spin current and polarization in impure two-dimensional electron systems with spin-orbit coupling," *Physical Review Letters*, vol. 93, pp. 226602, 2004.
- [76] A. A. Burkov, A. S. Nunez, and A. H. MacDonald, "Theory of spin-charge-coupled transport in a two-dimensional electron gas with Rashba spin-orbit interactions," *Physical Review B*, vol. 70, pp. 155308, 2004.
- [77] S. Saikin, "A drift-diffusion model for spin-polarized transport in a two-dimensional non-degenerate electron gas controlled by spin-orbit interaction," *Journal of Physics-Condensed Matter*, vol. 16, pp. 5071-5081, 2004.
- [78] S. Bandyopadhyay, M. E. Klausmeier-Brown, C. M. Maziar, S. Datta, and M. S. Lundstrom, "A Rigorous Technique to Couple Monte-Carlo and Drift-Diffusion Models for Computationally Efficient Device Simulation," *IEEE Transactions on Electron Devices*, vol. 34, pp. 392-399, 1987.
- [79] Y. V. Pershin, "Drift-diffusion approach to spin-polarized transport," *Physica E - Low-Dimensional Systems & Nanostructures*, vol. 23, pp. 226-231, 2004.
- [80] A. G. Malshukov, K. A. Chao, and M. Willander, "Quantum localization effects on spin transport in semiconductor quantum wells with zinc-blende crystal structure," *Physical Review Letters*, vol. 76, pp. 3794-3797, 1996.
- [81] M. E. Flatte and J. M. Byers, "Spin diffusion in semiconductors," *Physical Review Letters*, vol. 84, pp. 4220-4223, 2000.
- [82] S. Pramanik, "Spin dephasing in quantum wires," M.S. thesis, Department of Electrical and Computer Engineering, Virginia Commonwealth University, 2003.
- [83] A. A. Kiselev and K. W. Kim, "Progressive suppression of spin relaxation in two-dimensional channels of finite width," *Physical Review B*, vol. 61, pp. 13115-13120, 2000.
- [84] A. Svizhenko, S. Bandyopadhyay, and M. A. Strosio, "Velocity fluctuations and Johnson noise in quantum wires: the effect of phonon confinement," *Journal of Physics - Condensed Matter*, vol. 11, pp. 3697-3709, 1999.

- [85] N. Telang and S. Bandyopadhyay, "Hot electron magnetotransport in quantum wires," *Physical Review B*, vol. 51, pp. 9728-9734, 1995.
- [86] N. Telang and S. Bandyopadhyay, "Effects of a magnetic field on hot-electron transport in quantum wires," *Applied Physics Letters*, vol. 66, pp. 1623-1625, 1995.
- [87] J. C. Egues, G. Burkard, and D. Loss, "Datta-Das transistor with enhanced spin control," *Applied Physics Letters*, vol. 82, pp. 2658-2660, 2003.
- [88] A. Bournel, "Magneto-electronics in semiconductor devices," *Annales De Physique*, vol. 25, pp. 1, 2000.
- [89] A. Bournel, P. Dollfus, P. Bruno, and P. Hesto, "Spin-dependent transport phenomena in a HEMT," *Physica B*, vol. 272, pp. 331-334, 1999.
- [90] A. Bournel, P. Dollfus, P. Bruno, and P. Hesto, "Spin polarized transport in 1D and 2D semiconductor heterostructures," in *Ultrafast Phenomena in Semiconductors*, vol. 297-2, *Materials Science Forum*. Zurich-Uetikon: Transtec Publications Ltd, 1999, pp. 205-212.
- [91] A. Bournel, P. Dollfus, and P. Hesto, "Spin-dependent collection in ferromagnet/semiconductor contacts," *Journal of Magnetism and Magnetic Materials*, vol. 240, pp. 217-219, 2002.
- [92] S. Saikin, Y. V. Pershin, and V. Privman, "Modelling for semiconductor spintronics," *IEE Proceedings - Circuits, Devices, and Systems*, vol. 152, pp. 366-376, 2005.
- [93] S. Saikin, M. Shen, and M. C. Cheng, "Study of spin-polarized transport properties for spin-FET design optimization," *IEEE Transactions on Nanotechnology*, vol. 3, pp. 173-179, 2004.
- [94] S. Saikin, M. Shen, and M. C. Cheng, "Spin dynamics in a compound semiconductor spintronic structure with a Schottky barrier," *Journal of Physics - Condensed Matter*, vol. 18, pp. 1535-1544, 2006.

- [95] M. Shen, S. Saikin, and M. C. Cheng, "Monte Carlo modeling of spin injection through a Schottky barrier and spin transport in a semiconductor quantum well," *Journal of Applied Physics*, vol. 96, pp. 4319-4325, 2004.
- [96] M. Shen, S. Saikin, and M. C. Cheng, "Spin injection in spin FETs using a step-doping profile," *IEEE Transactions on Nanotechnology*, vol. 4, pp. 40-44, 2005.
- [97] M. Shen, S. Saikin, M. C. Cheng, and V. Privman, "Monte Carlo simulation of spin-polarized transport," in *Computational Science and its Applications - ICCSA 2003, Pt 2, Proceedings*, vol. 2668, *Lecture Notes in Computer Science*. Berlin: Springer-Verlag Berlin, 2003, pp. 881-891.
- [98] M. Shen, S. Saikin, M. C. Cheng, and V. Privman, "Monte Carlo modeling of spin FETs controlled by spin-orbit interaction," *Mathematics and Computers in Simulation*, vol. 65, pp. 351-363, 2004.
- [99] L. W. Molenkamp, G. Schmidt, and G. E. W. Bauer, "Rashba Hamiltonian and electron transport," *Physical Review B*, vol. 64, pp. 121202(R), 2001.
- [100] M. Governale and U. Zulicke, "Spin accumulation in quantum wires with strong Rashba spin-orbit coupling," *Physical Review B*, vol. 66, pp. 073311, 2002.
- [101] N. Telang and S. Bandyopadhyay, "Effects of a magnetic field on electron-phonon scattering in quantum wires," *Physical Review B*, vol. 48, pp. 18002-18009, 1993.
- [102] S. Bandyopadhyay, S. Pramanik, and M. Cahay, "Magnetoelectric subbands and eigenstates in the presence of Rashba and Dresselhaus spin-orbit interactions in a quantum wire," *Superlattices and Microstructures*, vol. 35, pp. 67-75, 2004.
- [103] M. Cahay and S. Bandyopadhyay, "Conductance modulation of spin interferometers," *Physical Review B*, vol. 68, pp. 115316, 2003.
- [104] D. D. Awschalom and J. M. Kikkawa, "Electron spin and optical coherence in semiconductors," *Physics Today*, vol. 52, pp. 33-38, 1999.
- [105] J. M. Kikkawa and D. D. Awschalom, "Lateral drag of spin coherence in gallium arsenide," *Nature*, vol. 397, pp. 139-141, 1999.

- [106] J. M. Kikkawa and D. D. Awschalom, "Resonant spin amplification in n-type GaAs," *Physical Review Letters*, vol. 80, pp. 4313-4316, 1998.
- [107] S. Pramanik, S. Bandyopadhyay, and M. Cahay, "Spin relaxation of "upstream" electrons in quantum wires: Failure of the drift diffusion model," *Physical Review B*, vol. 73, pp. 125309-1--125309-7, 2006.
- [108] G. Schmidt, D. Ferrand, L. W. Molenkamp, A. T. Filip, and B. J. van Wees, "Fundamental obstacle for electrical spin injection from a ferromagnetic metal into a diffusive semiconductor," *Physical Review B*, vol. 62, pp. R4790-R4793, 2000.
- [109] E. I. Rashba, "Theory of electrical spin injection: tunnel contacts as a solution of the conductivity mismatch problem," *Physical Review B*, vol. 62, pp. R16267-R16270, 2000.
- [110] A. T. Hanbicki, O. M. J. van 't Erve, R. Magno, G. Kioseoglou, C. H. Li, B. T. Jonker, G. Itskos, R. Mallory, M. Yasar, and A. Petrou, "Analysis of the transport process providing spin injection through an Fe/AlGaAs Schottky barrier," *Applied Physics Letters*, vol. 82, pp. 4092-4094, 2003.
- [111] A. T. Hanbicki, B. T. Jonker, G. Itskos, G. Kioseoglou, and A. Petrou, "Efficient electrical spin injection from a magnetic metal/tunnel barrier contact into a semiconductor," *Applied Physics Letters*, vol. 80, pp. 1240-1242, 2002.
- [112] K. Blum, *Density Matrix Theory and Applications*, 2nd ed. New York: Plenum Press, 1996.
- [113] S. Pramanik, C. G. Stefanita, and S. Bandyopadhyay, "Spin transport in self assembled all-metal nanowire spin valves: A study of the pure Elliott-Yafet mechanism," *Journal of Nanoscience and Nanotechnology*, vol. 6, pp. 1973-1978, 2006.
- [114] T. Ohgai, X. Hoffer, L. Gravier, J. E. Wegrowe, and J. P. Ansermet, "Bridging the gap between template synthesis and microelectronics: spin-valves and multilayers in self-organized anodized aluminium nanopores," *Nanotechnology*, vol. 14, pp. 978-982, 2003.

- [115] F. J. Jedema, H. B. Heersche, A. T. Filip, J. J. A. Baselmans, and B. J. van Wees, "Electrical detection of spin precession in a metallic mesoscopic spin valve," *Nature*, vol. 416, pp. 713-716, 2002.
- [116] F. J. Jedema, A. T. Filip, and B. J. van Wees, "Electrical spin injection and accumulation at room temperature in an all-metal mesoscopic spin valve," *Nature*, vol. 410, pp. 345-348, 2001.
- [117] V. Pokalyakin, S. Tereshin, A. Varfolomeev, D. Zaretsky, A. Baranov, A. Banerjee, Y. Wang, S. Ramanathan, and S. Bandyopadhyay, "Proposed model for bistability in nanowire nonvolatile memory," *Journal of Applied Physics*, vol. 97, pp. 124306, 2005.
- [118] S. Bandyopadhyay, A. E. Miller, H. C. Chang, G. Banerjee, V. Yuzhakov, D. F. Yue, R. E. Ricker, S. Jones, J. A. Eastman, E. Baugher, and M. Chandrasekhar, "Electrochemically assembled quasi-periodic quantum dot arrays," *Nanotechnology*, vol. 7, pp. 360-371, 1996.
- [119] H. Masuda and M. Satoh, "Fabrication of gold nanodot array using anodic porous alumina as an evaporation mask," *Japanese Journal of Applied Physics Part 2-Letters*, vol. 35, pp. L126-L129, 1996.
- [120] O. Rabin, P. R. Herz, S. B. Cronin, Y.-M. Lin, A. I. Akinwande, and M. S. Dresselhaus, *Materials Research Society Symposium*, vol. D.4.7.1, pp. 636, 2001.
- [121] N. Kouklin, L. Menon, and S. Bandyopadhyay, "Room-temperature single-electron charging in electrochemically synthesized semiconductor quantum dot and wire array," *Applied Physics Letters*, vol. 80, pp. 1649-1651, 2002.
- [122] T. Ohgai, L. Gravier, X. Hoffer, M. Lindeberg, K. Hjort, R. Spohr, and J. P. Ansermet, "Template synthesis and magnetoresistance property of Ni and Co single nanowires electrodeposited into nanopores with a wide range of aspect ratios," *Journal of Physics D - Applied Physics*, vol. 36, pp. 3109-3114, 2003.
- [123] H. Zeng, M. Zheng, R. Skomski, D. J. Sellmyer, Y. Liu, L. Menon, and S. Bandyopadhyay, "Magnetic properties of self-assembled Co nanowires of varying length and diameter," *Journal of Applied Physics*, vol. 87, pp. 4718-4720, 2000.

- [124] M. Zheng, L. Menon, H. Zeng, Y. Liu, S. Bandyopadhyay, R. D. Kirby, and D. J. Sellmyer, "Magnetic properties of Ni nanowires in self-assembled arrays," *Physical Review B*, vol. 62, pp. 12282-12286, 2000.
- [125] J. P. Ansermet, "Perpendicular transport of spin-polarized electrons through magnetic nanostructures," *Journal of Physics - Condensed Matter*, vol. 10, pp. 6027-6050, 1998.
- [126] N. W. Ashcroft and N. D. Mermin, *Solid State Physics*: Thomson Learning, 1975.
- [127] F. J. Jedema, M. S. Nijboer, A. T. Filip, and B. J. van Wees, "Spin injection and spin accumulation in all-metal mesoscopic spin valves," *Physical Review B*, vol. 67, pp. 085319, 2003.
- [128] J. Kainz, U. Rossler, and R. Winkler, "Temperature dependence of Dyakonov-Perel spin relaxation in zinc-blende semiconductor quantum structures," *Physical Review B*, vol. 70, pp. 195322, 2004.
- [129] S. Pramanik, C.-G. Stefanita, S. Patibandla, S. Bandyopadhyay, K. Garre, N. Harth, and M. Cahay, "Spin relaxation in a nanowire organic spin valve: observation of extremely long spin relaxation times," www.arxiv.org/cond-mat/0508744, 2006.
- [130] S. Pramanik, S. Bandyopadhyay, K. Garre, and M. Cahay, "Normal and inverse spin valve effect in organic semiconductor nanowires and the background monotonic magnetoresistance," accepted for publication (Nov. 2006), *Physical Review B*.
- [131] Z. H. Xiong, D. Wu, Z. V. Vardeny, and J. Shi, "Giant magnetoresistance in organic spin-valves," *Nature*, vol. 427, pp. 821-824, 2004.
- [132] V. Dediu, M. Murgia, F. C. Matocotta, C. Taliani, and S. Barbanera, "Room temperature spin polarized injection in organic semiconductor," *Solid State Communications*, vol. 122, pp. 181-184, 2002.
- [133] S. Forrest, P. Burrows, and M. Thompson, "The dawn of organic electronics," *IEEE Spectrum*, vol. 37, pp. 29-34, 2000.

- [134] G. Salis, S. F. Alvarado, M. Tschudy, T. Brunswiler, and R. Allenspach, "Hysteretic electroluminescence in organic light-emitting diodes for spin injection," *Physical Review B*, vol. 70, pp. 085203, 2004.
- [135] P. P. Ruden and D. L. Smith, "Theory of spin injection into conjugated organic semiconductors," *Journal of Applied Physics*, vol. 95, pp. 4898-4904, 2004.
- [136] Z. G. Yu, M. A. Berding, and S. Krishnamurthy, "Spin drift, spin precession, and magnetoresistance of noncollinear magnet-polymer-magnet structures," *Physical Review B*, vol. 71, pp. 060408 (R), 2005.
- [137] E. Arisi, I. Bergenti, V. Dediu, M. A. Loi, M. Muccini, M. Murgia, G. Ruani, C. Taliani, and R. Zamboni, "Organic light emitting diodes with spin polarized electrodes," *Journal of Applied Physics*, vol. 93, pp. 7682-7683, 2003.
- [138] A. H. Davis and K. Bussmann, "Organic luminescent devices and magnetoelectronics," *Journal of Applied Physics*, vol. 93, pp. 7358-7360, 2003.
- [139] T. L. Francis, O. Mermer, G. Veeraraghavan, and M. Wohlgenannt, "Large magnetoresistance at room temperature in semiconducting polymer sandwich devices," *New Journal of Physics*, vol. 6, pp. 185, 2004.
- [140] O. Mermer, G. Veeraraghavan, T. L. Francis, and M. Wohlgenannt, "Large magnetoresistance at room-temperature in small molecular weight organic semiconductor sandwich devices," www.arxiv.org/cond-mat/0501124, 2005.
- [141] O. Mermer, M. Wohlgenannt, G. Veeraraghavan, and T. L. Francis, "Weak localization and antilocalization in semiconducting polymer sandwich devices," www.arxiv.org/cond-mat/0312204, 2003.
- [142] E. Shikoh, Y. Ando, and T. Miyazaki, "Time resolved luminescence properties of Alq3 for spin-injection into organic semiconductor," *Journal of Magnetism and Magnetic Materials*, vol. 272-76, pp. 1921-1923, 2004.
- [143] Z. G. Yu, M. A. Berding, and S. Krishnamurthy, "Spin transport in organics and organic spin devices," *IEE Proceedings - Circuits, Devices, and Systems*, vol. 152, pp. 334-339, 2005.

- [144] W. Holleitner, V. Sih, R. C. Myers, A. C. Gossard, and D. D. Awschalom, "Suppression of spin relaxation in submicron InGaAs wires," in <http://www.arxiv.org/abs/cond-mat/0602155>, 2006.
- [145] A. K. Mahapatro, R. Agrawal, and S. Ghosh, "Electric-field-induced conductance transition in 8-hydroxyquinoline aluminum (Alq3)," *Journal of Applied Physics*, vol. 96, pp. 3583-3585, 2004.
- [146] M. Wohlgenannt, Z. V. Vardeny, J. Shi, T. L. Francis, X. M. Jiang, O. Mermer, G. Veeraraghavan, D. Wu, and Z. H. Xiong, "Spin and magnetic field effects in organic semiconductor devices," *IEE Proceedings - Circuits, Devices, and Systems*, vol. 152, pp. 385-392, 2005.
- [147] L. Menon, M. Zheng, H. Zeng, S. Bandyopadhyay, and D. J. Sellmyer, "Size dependence of the magnetic properties of electrochemically self-assembled Fe quantum dots," *Journal of Electronic Materials*, vol. 29, pp. 510-514, 2000.
- [148] S. J. Xie, K. H. Ahn, D. L. Smith, A. R. Bishop, and A. Saxena, "Ground-state properties of ferromagnetic metal/conjugated polymer interfaces," *Physical Review B*, vol. 67, pp. 125202, 2003.
- [149] M. Julliere, "Tunneling between ferromagnetic films," *Physics Letters A*, vol. 54A, pp. 225-226, 1975.
- [150] E. Y. Tsymbal, O. N. Mryasov, and P. R. LeClair, "Spin-dependent tunnelling in magnetic tunnel junctions," *Journal of Physics - Condensed Matter*, vol. 15, pp. R109-R142, 2003.
- [151] F. Zahid, A. W. Ghosh, M. Paulsson, E. Polizzi, and S. Datta, "Charging-induced asymmetry in molecular conductors," *Physical Review B*, vol. 70, pp. 245317, 2004.
- [152] B. J. Chen, W. Y. Lai, Z. Q. Gao, C. S. Lee, S. T. Lee, and W. A. Gambling, "Electron drift mobility and electroluminescent efficiency of tris(8-hydroxyquinolinolato) aluminum," *Applied Physics Letters*, vol. 75, pp. 4010-4012, 1999.
- [153] E. Y. Tsymbal, A. Sokolov, I. F. Sabirianov, and B. Doudin, "Resonant inversion of tunneling magnetoresistance," *Physical Review Letters*, vol. 90, 2003.

- [154] P. Mohanty, E. M. Q. Jariwala, and R. A. Webb, "Intrinsic decoherence in mesoscopic systems," *Physical Review Letters*, vol. 78, pp. 3366-3369, 1997.
- [155] S. Pramanik, S. Bandyopadhyay, and M. Cahay, "Spin relaxation in time versus space: the difference between charge and spin diffusion constants," *submitted*, 2006.
-

SHORT VITA OF SANDIPAN PRAMANIK

EDUCATION

Degree (Year)	Institution	Subject Area
Ph.D. (2006)	Virginia Commonwealth University	Electrical Engineering (<i>Specialization: Nanoelectronics and Spintronics</i>)
Master of Science (2003)	Virginia Commonwealth University	Electrical Engineering (<i>Specialization: Nanoelectronics and Spintronics</i>)
Bachelor of Engineering (2001)	Bengal Engineering and Science University, West Bengal, India	Electrical Engineering

APPOINTMENTS

2002-'03, 2004-'06, Research Assistant in Nanoelectronics and Spintronics, Quantum Device Laboratory, *Virginia Commonwealth University.*

2003-'04, Teaching Assistant, Department of Electrical and Computer Engineering, *Virginia Commonwealth University.*

HONORS AND PROFESSIONAL ACTIVITIES

- Referee, IEEE Transactions on Nanotechnology
- Student member of IEEE and APS (since 2003)
- Profiled in the Chancellor's list (2006), Who's who among students in American Universities and Colleges (2006)
- Awarded Phi Kappa Phi Graduate Student Scholarship (2006)
- Member of Tau Beta Pi (2005) and Phi Kappa Phi (2006, invited)

MAJOR PUBLICATIONS (including preprints)

Please refer to the following entries in the bibliography of this dissertation: [46, 47, 71, 72, 82, 102, 107, 113, 129, 130, 155].

COLOPHON

This document was created in Microsoft Word 2002 and converted to Portable Document Format (PDF) with Adobe Acrobat PDF Maker on a Windows XP computer. Images were created in JPEG format. Formatting is in compliance with VCU electronic thesis and dissertation (ETD) guideline, available at <http://etd.vcu.edu/>
